AN ABSTRACT OF THE DISSERTATION OF

Christopher L. Wolfe for the degree of Doctor of Philosophy in Oceanography presented on September 8, 2006.
Title: Quantifying Linear Disturbance Growth in Periodic and Aperiodic Systems

Abstract approved: ______________________________

Roger M. Samelson

The mathematical and physical connections between three different ways of quantifying linear predictability in geophysical fluid systems are studied in a series of analytical and numerical models. Normal modes, as they are traditionally formulated in the instabilities theories of geophysical fluid dynamics, characterize the asymptotic development of disturbances to stationary flows. Singular vectors, currently used to generate initial conditions for ensemble forecasting systems at some operational centers, characterize the transient evolution of disturbances to flows with arbitrary time dependence. Lyapunov vectors are an attempt to associate a physical structure with the Lyapunov exponents, which give the rate at which the trajectories of dynamical systems diverge. It is shown that these seemingly divergent ways of quantifying linear disturbance growth are closely related. It is argued that Lyapunov vectors are a natural generalization of normal modes to flows with arbitrary time dependence. Singular vectors are shown to asymptotically converge to orthogonalizations of the Lyapunov vectors. A direct, efficient, and norm-independent method for constructing the n most rapidly growing Lyapunov vectors from the n most rapidly growing forward and the n most rapidly decaying backward asymptotic singular vectors is proposed and demonstrated using several models of geophysical flows.

These connections are further studied using a (time-periodic) wave-mean oscillation in an intermediate complexity baroclinic channel model. For time-periodic systems, normal modes may be defined in terms of Floquet vectors. It is argued that Floquet vectors are equivalent to Lyapunov vectors for time-periodic flows. The Floquet vectors of the wave-mean oscillation are found to split into two dynamically distinct classes that have analogs in the classical theories of the baroclinic instability and parallel shear flow. The singular vectors of the oscillation are found to preserve this dynamical splitting. The representations of the singular vectors in terms of the forward and adjoint Floquet vectors display much simpler temporal behavior than the singular vectors or the Floquet vectors individually. It is further demonstrated that while the Floquet vectors point 'onto' the local system attractor, the singular vectors point 'off' the attractor.

Quantifying Linear Disturbance Growth in Periodic and Aperiodic Systems

by
Christopher L. Wolfe

A DISSERTATION

submitted to

Oregon State University

in partial fulfillment of
the requirements for the
degree of

Doctor of Philosophy

Presented September 8, 2006
Commencement June 2007

Doctor of Philosophy dissertation of Christopher L. Wolfe presented on

September 8, 2006

APPROVED:

Major Professor, representing Oceanography

Dean of the College of Oceanic and Atmospheric Sciences

Dean of the Graduate School

I understand that my dissertation will become part of the permanent collection of Oregon State University libraries. My signature below authorizes release of my dissertation to any reader upon request.

Christopher L. Wolfe, Author

ACKNOWLEDGMENTS

I would first like to thank my advisor, Roger Samelson, for supporting me and guiding me through the past five years. I am especially grateful that he encouraged to attend the WHOI GFD Summer School and allowed me to spend a significant amount of time pursuing research questions that arose there once I returned. I would also like to thank my committee members, Andrew Bennett, Robert Miller, Roland deSzoeke, and Solomon Yim, for taking the time to attend multiple events and providing helpful suggestions. Special thanks go to Andrew for teaching two classes for which I was the only registered student.

The primary responsibility for who I am today, of course, lies with my parents, Donald and Penelope. They inspired an early desire to become a scientist and encouraged me to do 'something useful' for society. With this dissertation, I am fulfilling the first goal ... I'm still working on the second. Thanks Mom and Dad!

The past five years wouldn't have been the same with out the constant companionship of my greatest friend and partner Melanie. The contribution she has made to my life is impossible to put into words. I would also like to thank her parents, Randy and Jane, for hosting me in Indiana every Christmas and reminding me that Oregon never really gets all that cold.

Thanks go to all of my close friends who made life in Oregon much more interesting and entertaining than it would have been otherwise. Special thanks go to Rachel, Kerry, Cornelius, Keeta, Rhiannon, Claire, and all the residents and frequent visitors to the 24th Street Home for Wayward Boys.

TABLE OF CONTENTS

TABLE OF CONTENTS (Continued)

TABLE OF CONTENTS (Continued)

LIST OF FIGURES

LIST OF TABLES

DEDICATION

For Cornelius and Keeta, but most of all, for my mother, Penelope.

Quantifying Linear Disturbance Growth in Periodic and Aperiodic Systems

1 INTRODUCTION

A series of numerical and analytical studies of linear disturbance growth are performed using several low- to intermediate-complexity models. Of primary interest are the physical and mathematical relationships between three different approaches to quantifying linear disturbance growth: normal modes, singular vectors, and Lyapunov vectors.

Normal mode analyses form the backbone of geophysical stability theory and are classically defined as those linear disturbances which may be factored into a part with exponential time-dependence and a structure function with fixed (or possible recurring) spatial structure (see, e.g., Drazin and Reid, 2004). The utility of normal mode analysis is two-fold: First, normal modes characterize asymptotic linear stability since a flow is asymptotically unstable if any one of its normal modes are unstable. Second, normal mode structure functions often have compelling physical interpretations which can be used to understand the nature of a flow's stability or instability.

Singular vectors, also known as optimal disturbances, are structures which optimize linear disturbance growth in a specified norm over a specified time interval (Lorenz, 1965; Farrell, 1989). In contrast to normal modes, singular vectors characterize transient, not asymptotic stability. While singular vectors generalize easily to unsteady flows, the considerable arbitrariness in the choice of norm and optimization interval can make their physical interpretation difficult. Singular vectors currently find their greatest utility in operational ensemble forecasting systems (Buizza et al., 1993; Ehrendorfer and Tribbia, 1997).

Lyapunov exponents measure the average rate at which the phase-space trajectories of dynamical systems diverge and, as such, they characterize the asymptotic evolution of linear disturbances (Oseledec, 1968; Eckmann and Ruelle, 1985). Steady or time-periodic trajectories with positive Lyapunov exponents are asymptotically unstable while, for bounded aperiodic trajectories, having a positive Lyapunov exponent is often considered to be an operational definition of chaos. As geophysical flows can be represented as high- or infinite-dimensional dynamical systems, it is natural that Lyapunov exponents are closely related to the stability exponents of normal modes and to singular values (the singular vector growth factors). For steady or time-periodic flows, the Lyapunov exponents are equal to the real parts of the stability exponents (see, e.g., Wiggins, 2003). Further, for arbitrary flows, the singular values asymptotically grow a rates given by the Lyapunov exponents as the optimization interval extends infinitely far into the future or the past (Legras and Vautard, 1996).

'Lyapunov vectors' are an attempt to associate physical structures with the Lyapunov exponents. There are several reason why such an association is useful. First, since Lyapunov exponents naturally generalize stability exponents to aperiodic systems, it is hoped that a suitable definition of the Lyapunov vectors will naturally generalize normal modes and their physical structures may shed light on the mechanisms sustaining chaotic behavior. Also, since the unstable (i.e. growing) Lyapunov vectors exhibit the largest disturbance growth in the long-term, it might be hoped that initializing ensemble forecasting systems with Lyapunov vectors also leads to largest ensemble spread in the long-term, maximizing the utility of the forecast system. The different requirements of these two applications have lead to different definitions of 'the' Lyapunov vectors.

For ensemble forecasting applications, all that is needed is a set of vectors which spans the subspace of growing disturbances. This has lead some authors to define Lyapunov vectors to be singular vectors optimized infinitely far in the past (Legras and Vautard, 1996; Szuntogh et al., 1997), since these vectors grow at rates given by the Lyapunov exponents. Since singular vectors are norm-dependent, these Lyapunov vectors are also norm-dependent, but this is not a problem since these vectors span the correct subspace. This definition is unsuitable for the first application, however, since the norm-dependence leads same difficulties in physical interpretation found with singular vectors. 'Proper' Lyapunov vectors should be defined so that they are norm-independent. Further, it is desirable that they agree with normal modes for the cases of stationary and time-periodic flows. Lyapunov vectors with these properties can be defined in terms of intersecting sets of singular vectors optimized asymptotically far in the past and the future by application of a corollary to the Oseledec (1968) theorem (Legras and Vautard, 1996; Trevisan and Pancotti, 1998). (Note that Legras and Vautard (1996) use the term 'characteristic vector' to describe these vectors, since they apply the term 'Lyapunov vector' to the norm-dependent vectors generated by the previous definition.)

It should be noted that operational forecasting centers use bred vectors instead of Lyapunov vectors (Toth and Kalnay, 1993, 1997). Bred vectors are considered to be a finite-amplitude generalization of Lyapunov vectors and have the advantange over Lyapunov vectors of being generated automatically by the integration of the (nonlinear) ensemble members. Additionally, their finite amplitude evolution is intended to filter out fast-growing, but low-amplitude, instabilities of low significance to the large-scale forecast (e.g., convective instabilities). The present series of studies focuses on linear disturbances growth, however, and so is primarly concerned Lyapunov vectors rather than bred vectors.

A detailed discussion of the relationship between singular vectors, normal modes, and the two definitions of Lyapunov vectors is given in chapter 2. Additionally, a direct, efficient, and norm-independent method for constructing the n most rapidly growing Lyapunov vectors from the n most rapidly growing forward and the n most rapidly decaying backward asymptotic singular vectors is proposed. An analogous method allows the construction of the n most rapidly decaying Lyapunov vectors from n decaying forward and n growing backward singular vectors. This method is demonstrated using two low-dimensional models.

Chapters 3 and 4 focus on a normal-mode and singular vector, respectively, analysis of a wave-mean oscillation in an intermediate complexity, two-layer, quasi-geostrophic spectral model. These studies build on and extend a previous analysis of a weakly nonlinear model of the baroclinic instability (Samelson, 2001b,a). Samelson (2001b) analyzed a stable limit cycle of the weakly nonlinear model in terms of time-periodic normal modes (Floquet vectors) and singular vectors. It was found that the normal modes split into two dynamical classes distinguished by spatio-temporal structure and stability exponent (Floquet exponent). The first class was characterized of large-scale wave-like disturbances which grew or decayed inviscidly at rates well separated from the damping rate; hence, this class was refered to as the 'wave-dynamical' class. The second class, the 'viscous-advective' class, was characterized by small-scale disturbances which were advected by the mean flow and decayed at roughly the damping rate. The singular vectors displayed a similar dynamical splitting, with the wave-dynamical (resp. viscous-advective) singular vectors projecting mainly onto the wave-dynamical (resp. viscous-advective) Floquet vectors. Furthermore, the projections were relatively simple functions of initialization and optimization time, varying little even though both the Floquet and singular vectors underwent large changes in spatial structure. This implies a stronger connection between singular vectors and normal modes than is commonly appreciated.

This analysis was extended into a weakly chaotic regime using ideas from periodic cycle expansion theory, which posits that the behavior of trajectories on a chaotic attractor can be understood in terms of a self-similar ‘skeleton’ of unstable periodic orbits (see, e.g., Cvitanović et al., 2005). In the weakly chaotic regime, the system displayed behavior which is essentially similar to that the logistic map. In particular, the Poincaré first-return map took the approximate form of an asymmetric quadratic function, allowing the formulation of a complete symbolic dynamics. The symbolic dynamics and inverse iteration of the first-return map generated first-guess initial conditions for unstable periodic orbits, which were then refined using Newton’s method. In this manner, the orbits corresponding all possble symbol sequences with twelve characters or less were generated and subjected to Floquet and singular vector analyses. The dynamical splitting first noted in disturbances to the stable limit cycle was essentially unchanged in disturbances to the unstable periodic orbits. Since the unstable periodic orbits visit a large fraction of the attractor, it was concluded that the dynamical splitting of linear disturbances is likely to occur for most trajectories in the attractor. This conclusion is strengthened by the observation that the leading Floquet vector of the lowest order orbit is a good approximation to the leading Lyapunov vector of the attractor at most locations on the Poincaré section (Samelson, 2001a).

It was of interest to determine if similar results could be obtained in a model with vastly greater dimension and less constrained dynamics. The model considered was a spectral representation of the nonlinear Phillips (1954) model with several thousand degrees of freedom. Attention was focused on a strongly nonlinear regime where the model possessed a moderately high-dimensional (Kaplan-Yorke dimension ≈ 7) chaotic attractor. It was not possible to find simple representation for the Poicaré first-return map and so a 'brute-force' search for unstable periodic orbits was undertaken by looking for near-recurrences in long time-series. Given the high dimensionality of the attractor, near recurrences are rare and only a handful of unstable periodic orbits were found. The analyses of chapters 3 and 4 focus on a low-order periodic orbit with multiple normal-mode instabilities which resembles the limit cycle and lowest order unstable periodic orbit studied by Samelson (2001b,a). This orbit is also described in Samelson and Wolfe (2003), which gives a preliminary analysis of the leading Floquet vectors.

As discussed in chapter 3, the Floquet vectors of this orbit fall into two classes which have direct physical interpretations: wave dynamical modes and damped-advective modes (analogous to the viscous-advective modes in the weakly nonlinear model). The wave-dynamical modes (which include two neutral modes related to continuous symmetries of the underlying system) have large scales and can efficiently exchange energy and vorticity with the basic flow; thus, the dynamics of the wave-dynamical modes reflects the dynamics of the wave-mean oscillation. These modes are analogous to the normal modes of steady parallel flow. On the other hand, the damped-advective modes have fine scales and dynamics which reduces, to first order, to damped advection of the potential vorticity by the basic flow. While individual wave-dynamical modes have immediate physical interpretations as discrete normal modes, the damped-advective modes are best viewed, in sum, as a generalized solution to the damped advection problem. The asymptotic stability of the time-periodic basic flow is determined by a small number of discrete wave-dynamical modes and, thus, the number of independent initial disturbances which may destabilize the basic flow is likewise small. Comparison of the Floquet exponent spectrum of the wave-mean oscillation to the Lyapunov exponent spectrum of a nearby aperiodic trajectory suggests that this result will still obtain when the restriction to time-periodicity is relaxed.

In chapter 4, the relationship between singular vectors and Floquet vectors (the analog of Lyapunov vectors for time-periodic systems) is analyzed in the context of the nonlinear baroclinic wave-mean oscillation. It is found that the singular vectors divide into two dynamical classes which are related to those of the Floquet vectors. Singular vectors in the wave-dynamical class are found to asymptotically approach constant linear combinations of Floquet vectors. The most rapidly decaying singular vectors project strongly onto the most rapid decaying Floquet vectors. In contrast, the leading singular vectors project strongly onto the leading adjoint Floquet vectors. Examination of trajectories which are 'near' the basic cycle show that the leading Floquet vectors point 'into' the local unstable tangent space of the attractor while the leading initial singular vectors point 'off' the local attractor. The method for recovering the leading Lypaunov (here Floquet) vectors from a small number of leading singular vectors developed in chapter 2 is additionally demonstrated.

2 RECOVERING LYAPUNOV VECTORS FROM SINGULAR VECTORS

Christopher L. Wolfe and Roger M. Samelson

Submitted to *Tellus*

Blackwell Munksgaard

1 Rosenørns Allé

DK-1970 Frederiksberg C

Denmark

Submitted

2.1 Introduction

Geophysical fluid flows often exhibit complex and apparently random behavior. One compelling explanation for this apparent randomness is that small errors in the initial, boundary, and forcing conditions are amplified by instabilities of the fluid motions. This is an example the so-called sensitive dependence on initial conditions of nonlinear dynamical systems. Several techniques have been developed to quantify linear disturbance growth in systems subject to sensitive dependence on initial conditions, including the traditional normal-mode instability theories of fluid dynamics (e.g., Drazin and Reid, 2004), Lyapunov vectors from dynamical systems theory (Oseledec, 1968; Eckmann and Ruelle, 1985), and singular vectors from ensemble forecasting (Lorenz, 1965; Farrell, 1989; Buizza and Palmer, 1995; Buizza et al., 2005).

Normal modes, in the simplest conceptions, are linear disturbances with a fixed spatial structure which grow at a fixed exponential rate. Singular vectors, by contrast, optimize disturbance growth in a specified norm over a specified time-interval, and their spatial structure is generally time-dependent. Lyapunov vectors, which have generally received less attention in the literature than Lyapunov exponents, are the time-dependent spatial structures associated with the corresponding Lyapunov exponents, which are in turn the asymptotic exponential growth rates of linear disturbances in general time-dependent flows. The definition of the Lyapunov vectors given in the literature varies depending on the application. We focus on a norm-independent definition of the Lyapunov vectors which emphasizes their connection to normal modes.

We present an efficient, norm-independent method for constructing Lyapunov vectors from asymptotic singular vectors. This method generalizes and streamlines similar methods given by Legras and Vautard (1996) and Trevisan and Pancotti (1998). The method is demonstrated using two low-order geophysical models. The format of the paper is as follows: We review the definitions of singular vectors, Lyapunov vectors, and normal modes is section 2.2. The connections between singular vectors and Lyapunov vectors are discussed in section 2.3. In section 2.4, we present the method for constructing Lyapunov vectors from singular vectors. Two numerical examples which demonstrate the method are presented in section 2.5. Finally, section 2.6 contains a discussion of some of the practical implications of the method developed in section 2.4.

2.2 Definitions

2.2.1 Dynamical system and propagator

Consider a flow which, when discretized, satisfies the autonomous N-dimensional dynamical system

$$\dot{\boldsymbol{x}} = \mathbf{F}(\boldsymbol{x}). \tag{2.1}$$

In general, N is very large. The evolution of infinitesimal disturbances $\boldsymbol{y}$ to the flow $\boldsymbol{x}$ is governed by the tangent linearization of eq. (2.1)

$$\dot{\boldsymbol{y}} = \mathbf{A}(\boldsymbol{x}(t))\,\boldsymbol{y} \tag{2.2}$$

where

$$\mathbf{A}(\boldsymbol{x}(t)) = \frac{\partial \mathbf{F}(\boldsymbol{x}(t))}{\partial \boldsymbol{x}}. \tag{2.3}$$

The propagator $\mathcal{L}(t_2, t_1)$ is a matrix which takes solutions of (2.2) at time t_1 to solutions of (2.2) at time t_2. It can be represented as

$$\mathcal{L}(t_2, t_1) = \mathbf{Z}(t_2)\mathbf{Z}(t_1)^{-1}, \tag{2.4}$$

where $\mathbf{Z}$ is matrix whose columns form a complete set of solutions to eq. (2.2).

2.2.2 Normal modes

The traditional definition of normal modes depends on the time dependence the flow and thus on the time dependence of the matrix $\mathbf{A}$ in eq. (2.2). If the flow is stationary, the normal modes and their exponential growth rates are simply the eigenvectors and eigenvalues of $\mathbf{A}$, respectively. The normal modes are norm-independent, time-stationary disturbances whose asymptotic stability is determined by the corresponding growth rate. A very useful property of normal modes is that they are often physically meaningful and facilitate the interpretation of flow instability. The normal modes will be orthogonal in a given norm if $\mathbf{A}$ is normal (i.e., it commutes with its adjoint) in that norm.

If the flow is time-periodic with period T, the normal modes are Floquet vectors: the eigenvectors of the one-period propagator $\mathcal{L}(t+T, t)$ (see, e.g., Coddington and Levinson, 1955). The asymptotic stability of the Floquet vectors is determined by the corresponding Floquet exponents, which are the logarithms of the eigenvalues of $\mathcal{L}(t+T, t)$. The Floquet vectors consist of a time-periodic structure function multiplying a part which grows or decays exponentially at the rate given by the Floquet exponent. Like time-stationary normal modes, Floquet vectors have compelling physical interpretations which shed light on the instability mechanisms of the background flow (Wolfe and Samelson, 2006).

Currently, there does not appear to be a consensus in the literature on a definition of normal modes which generalizes to aperiodic flows. To be a proper generalization, the candidate definition should reduce to stationary normal modes or Floquet vectors for stationary or time-periodic flows, respectively, and thus should be norm-independent and characterize the asymptotic stability of linear disturbances to the flow. Singular vectors do not provide the required generalized due to their (strong) dependence on norm and optimization interval. Additionally, singular vectors characterize transient stability only and it is easy to construct asymptotically stable systems which nevertheless have growing singular vectors for certain optimization intervals (Farrell and Ioannou, 1996). Finite-time normal modes (FTNM), the eigenvectors of the arbitrary-time propagator $\mathcal{L}(t_2, t_1)$ (Frederiksen, 1997), are free from norm-dependence, but do not necessarily characterize asymptotic stability. While FTNMs are equivalent to time-stationary normal modes for time-stationary flows, if the flow is T-periodic, FTNMs reduce to Floquet vectors only if $t_2 - t_1 = nT$, for some integer $n \neq 0$. If $t_2 - t_1 \neq nT$, the eigenvectors and eigenvalues of $\mathcal{L}(t_2, t_1)$ loose their significance (Trevisan and Pancotti, 1998). For aperiodic flows, there is no way to choose a 'correct' value of $t_2 - t_1$. We argue in section 2.2.4 that Lyapunov vectors, properly defined, are a good (though, not necessarily the only) generalization of normal modes to aperiodic flows.

2.2.3 Singular vectors

Singular vectors optimize the growth of perturbations in a specified norm over a specified optimization interval $\tau = t_2 - t_1$. It is straightforward to show that the initial singular vectors $\boldsymbol{\xi}_{0,j}(t_1, t_2)$, initialized and optimized at times t_1 and t_2, respectively, are the eigenvectors of $\mathcal{L}(t_2, t_1)^* \mathcal{L}(t_2, t_1)$. $\mathcal{L}(t_2, t_1)^*$ is the adjoint of

$\mathcal{L}(t_2, t_1)$ and is defined by the identity $\langle \boldsymbol{v}, \mathcal{L}\boldsymbol{w} \rangle = \langle \mathcal{L}^* \boldsymbol{v}, \boldsymbol{w} \rangle$. The singular vectors can be evolved to any time t by application of the propagator. We will use the notation

$$\boldsymbol{\xi}_j(t; t_1, t_2) \equiv \mathcal{L}(t, t_1)\boldsymbol{\xi}_{0,j}(t_1, t_2) \tag{2.5}$$

to denote the singular vector with initialization and optimization times t_1 and t_2 which has been evolved to time t. The final, or 'evolved,' singular vectors are simply $\boldsymbol{\xi}_j(t_2; t_1, t_2)$. They may also be obtained as the eigenvectors of $\mathcal{L}(t_2, t_1)\mathcal{L}(t_2, t_1)^*$.

If the inner product $\langle \cdot, \cdot \rangle$ is characterized by the matrix $\mathbf{N}$ such that

$$\langle \boldsymbol{v}, \boldsymbol{w} \rangle = \boldsymbol{v}^{\mathrm{T}} \mathbf{N} \boldsymbol{w}, \tag{2.6}$$

then

$$\mathbf{N}\mathcal{L}(t_2, t_1)^* = \mathcal{L}(t_2, t_1)^{\mathrm{T}} \mathbf{N}. \tag{2.7}$$

If the initial and final time norms are the same, the singular vectors and their amplification factors (the singular values) σ_j satisfy the generalized eigenvalue problem

$$\mathcal{L}(t_2, t_1)^{\mathrm{T}} \mathbf{N} \mathcal{L}(t_2, t_1)\boldsymbol{\xi}_j(t_1; t_1, t_2) = \sigma_j^2 \mathbf{N} \boldsymbol{\xi}_j(t_1; t_1, t_2), \tag{2.8}$$

For systems where the range of singular value magnitudes is not too great, the eigenvalue problem (2.8) may be solved directly. Otherwise, a more robust method is singular value decomposition, which allows square matrix $\mathbf{B}$ to be written as

$$\mathbf{B} = \mathbf{U}\mathbf{S}\mathbf{V}^{\mathrm{T}}, \tag{2.9}$$

where $\mathbf{U}$ and $\mathbf{V}$ are orthogonal matrices and $\mathbf{S}$ is diagonal (see, e.g., Golub and Van Loan, 1996). If eq. (2.9) is left-multiplied by $\mathbf{B}^{\mathrm{T}}$, singular value decomposition of $\mathbf{B}$ is seen to be equivalent to eigen-decomposition of $\mathbf{B}^{\mathrm{T}}\mathbf{B}$, since

$$\mathbf{B}^{\mathrm{T}}\mathbf{B} = \mathbf{V}\mathbf{S}\mathbf{U}^{\mathrm{T}}\mathbf{U}\mathbf{S}\mathbf{V}^{\mathrm{T}} = \mathbf{V}\mathbf{S}^2\mathbf{V}^{\mathrm{T}}. \tag{2.10}$$

Thus, eq. (2.10) will be equivalent to eq. (2.8) if

$$\mathbf{B} = \mathbf{N}^{1/2}\mathcal{L}(t_2, t_1)\mathbf{N}^{-1/2}, \tag{2.11}$$

$$\boldsymbol{v}_j = N^{1/2}\boldsymbol{\xi}_j(t_1; t_1, t_2), \tag{2.12}$$

and

$$\mathbf{S}_{jj} = \sigma_j, \tag{2.13}$$

where $\boldsymbol{v}_j$ is the j^{th} column of $\mathbf{V}$. Similarly, right multiplication of eq. (2.9) by $\mathbf{B}^{\mathrm{T}}$ shows that

$$\boldsymbol{u}_j = \sigma_j^{-1}\mathbf{N}^{1/2}\boldsymbol{\xi}_j(t_2; t_1, t_2), \tag{2.14}$$

where $\boldsymbol{u}_j$ is the j^{th} column of $\mathbf{U}$.

The singular vectors for the examples of section 2.5 where calculated using the singular value decomposition method.

2.2.4 Lyapunov vectors

Unlike singular values, which characterize disturbance growth over a specified time interval, Lyapunov exponents characterize the asymptotic evolution of linear disturbances. The Lyapunov exponents $\lambda^{\pm}$ can be shown to be the logarithms of the eigenvalues of the matrix

$$\mathbf{S}_{\pm}(t_1) = \lim_{t_2 \to \pm\infty} \left[\mathcal{L}(t_2, t_1)^{*}\mathcal{L}(t_2, t_1)\right]^{1/2(t_2 - t_1)}. \tag{2.15}$$

This matrix exists under fairly general conditions (primarily, that the nonlinear trajectory exists and is bounded as $t \to \pm\infty$) and its eigenvalues are independent of norm and the initial time t_1 for almost every choice of t_1 (Oseledec, 1968). Further, the forward and backward Lyapunov spectra are identical except for a change in sign, hence $\lambda_i^- = -\lambda_i^+$. We can thus unambiguously refer to $\lambda_i \equiv \lambda_i^+$ as *the* i^{th} Lyapunov exponent. Note that the Lyapunov spectrum may be degenerate, so that the total number of distinct Lyapunov exponents M may be less than the dimension of the system N.

Comparison of eq. (2.15) to eq. (2.8) shows that the singular values must become asymptotically independent of norm and initialization time as the optimization interval τ tends to infinity. The singular vectors must become asymptotically independent of τ as $\tau \to \pm\infty$ for the limit eq. (2.15) to exist, but they may retain their dependence on norm and initialization time.

Lyapunov vectors are an attempt to associate a physical structure with Lyapunov exponents. The precise definition of the Lyapunov vectors varies with the applications intended for them. Some authors define Lyapunov vectors to be the eigenvectors $\boldsymbol{\xi}^+$ of $\mathbf{S}_+$, equivalent to initial singular vectors optimized in the distant future (Goldhirsch et al., 1987; Yoden and Nomura, 1993). Others define Lyapunov vectors to be the eigenvectors $\boldsymbol{\xi}^-$ of $\mathbf{S}_+$, equivalent to final singular vectors optimized in the distant past (Lorenz, 1965, 1984; Shimada and Nagashima, 1979). Legras and Vautard (1996) consider both and call the former 'forward' Lyapunov vectors and the latter 'backward' Lyapunov vectors. These definitions produce norm-dependent Lyapunov vectors since. while the eigenvalues of $\mathbf{S}_\pm$ are independent of norm, the eigenvectors are not (except for the first or the last eigenvector). Lyapunov vectors defined in this manner are typically intended for use in predictability studies. For these applications, all that is needed is a set of vectors which spans the same subspace as the growing disturbances so norm-dependence is not a problem.

However, these norm-dependent definitions are unsatisfactory for candidate aperiodic normal modes for a number of reasons. First, neither of these definitions reduce, in general, to stationary normal modes or Floquet vectors for stationary or time-periodic flows. Further, the Lyapunov vectors defined as the eigenvectors of $\mathbf{S}_+$ or $\mathbf{S}_-$ do not characterize asymptotic stability forward and backward in time since, while the eigenvector $\boldsymbol{\xi}_i^+$ grows asymptotically with the rate λ_i as $t \to \infty$, it does not, in general, decay with the rate $-\lambda_i$ as $t \to -\infty$.

A norm-independent set of Lyapunov vectors $\boldsymbol{\phi}_i$, such that $\boldsymbol{\phi}_i$ grows at the rate $\pm\lambda_i$ as $t \to \pm\infty$, may defined using the following consequence of the Oseledec (1968) theorem: For almost every time t, every vector $\boldsymbol{y}$ in the tangent space $\mathcal{S}_1^+(t) = \mathbb{R}^N$ of the dynamical system eq. (2.1) grows asymptotically at a rate given by the first Lyapunov exponent λ_1 as the system evolves forward in time, except those $\boldsymbol{y}$ belonging to a set $\mathcal{S}_2^+(t)$ of measure zero. Similarly, every vector $\boldsymbol{y} \in \mathcal{S}_2^+(t)$ asymptotically grows at the rate λ_2 except those $\boldsymbol{y}$ belonging to a set $\mathcal{S}_3^+(t)$ of measure zero relative to $\mathcal{S}_2^+(t)$. This argument may be applied recursively to obtain a set of nested subspaces

$$\mathcal{S}_M^+(t) \subset \mathcal{S}_{M-1}^+(t) \subset \cdots \subset \mathcal{S}_1^+(t) = \mathbb{R}^N \tag{2.16}$$

such than any vector $\boldsymbol{y} \in \mathcal{S}_i^+(t) \setminus \mathcal{S}_{i+1}^+(t)$ grows asymptotically at the rate $\hat{\lambda}_i$, where $\hat{\lambda}_i$ is the i^{th} *distinct* Lyapunov exponent and $M \leq N$ is the number of distinct Lyapunov exponents (Eckmann and Ruelle, 1985). The dimension of the difference space $\mathcal{S}_i^+(t) \setminus \mathcal{S}_{i+1}^+(t)$ is equal to the multiplicity m_i of $\hat{\lambda}_i$.

A similar argument may be made as the system evolved backward in time to obtain a similar set of nested subspaces

$$\mathcal{S}_M^-(t) \subset \mathcal{S}_{M-1}^-(t) \subset \cdots \subset \mathcal{S}_1^-(t) = \mathbb{R}^N \tag{2.17}$$

such than any vector $\mathbf{y} \in \mathcal{S}_i^-(t) \setminus \mathcal{S}_{i+1}^-(t)$ grows at the exponential rate $-\hat{\lambda}_i$. The intersection space

$$\mathcal{T}_i(t) = \mathcal{S}_i^+(t) \cap \mathcal{S}_{M-i+1}^-(t) \tag{2.18}$$

is, in general, m_i-dimensional, where m_i is the multiplicity of the i^{th} Lyapunov exponent. If $d = 1$, then $\mathcal{T}_i$ may be identified as *the* Lyapunov vector $\boldsymbol{\phi}_i$ since it grows asymptotically at the rates $\hat{\lambda}_i$ and $-\hat{\lambda}_i$ as the system evolved forward and backward, respectively, in time. If $d > 1$, then any m_i linearly independent vectors from $\mathcal{T}_i$ may be identified as Lyapunov vectors.

The $\boldsymbol{\phi}_i$ defined in this manner are norm-independent and characterize the asymptotic stability of linear disturbances as the system evolves both forward and backward in time. Further, the $\boldsymbol{\phi}_i$ reduce to the Floquet vectors if the flow is time-periodic (Trevisan and Pancotti, 1998) and to the stationary normal modes if the flow is stationary. The Lyapunov vectors $\boldsymbol{\phi}_i$ are thus good candidates for aperiodic normal modes.

This norm-independent definition of the Lyapunov vectors $\boldsymbol{\phi}_i$ has been given previously by several authors (e.g., Vastano and Moser, 1991; Legras and Vautard, 1996; Trevisan and Pancotti, 1998). Note that Legras and Vautard (1996) call the $\boldsymbol{\phi}_i$ "characteristic vectors." Trevisan and Pancotti (1998) show how these Lyapunov vectors may be obtained from singular vectors in the three-dimensional Lorenz (1963) system. Their method may, *in principle*, be extended to arbitrary N-dimensional systems, but would require the knowledge of $N + 1$ singular vectors. In modern forecast and process models, N is very large and this method would be prohibitively expensive. In section 2.4, we give an efficient method for constructing the leading n Lyapunov vectors using just $2n$ singular vectors.

2.3 Connections between Lyapunov vectors and singular vectors

It is apparent from the discussion in the previous section that Lyapunov vectors are closely related to singular vectors with long optimization intervals. Singular vectors are, in fact, orthogonalizations of the Lyapunov vectors (Trevisan and Pancotti, 1998). To see how this is so, fixed a time t and consider evolved singular vectors initialized in the distant past ($t_1 \ll t$) and optimized at t, i.e. consider

$$\hat{\boldsymbol{\eta}}_j(t) \equiv \lim_{t_1 \to -\infty} \boldsymbol{\xi}_j(t; t_1, t). \tag{2.19}$$

These singular vectors will be referred to as the 'backward' singular vectors since they are equivalent to Legras and Vautard's 'backward' Lyapunov vectors. Since almost all linear disturbances rotate toward the leading Lyapunov vector, we must have $\hat{\boldsymbol{\eta}}_1(t) = \hat{p}_{11}\boldsymbol{\phi}_1(t)$, for some projection coefficient $\hat{p}_{11}$. The second singular vector $\hat{\boldsymbol{\eta}}_2(t)$ is constrained to be orthogonal (in the selected inner product) to $\hat{\boldsymbol{\eta}}_1(t)$ and thus cannot rotate toward the leading Lyapunov vector. The growth of $\hat{\boldsymbol{\eta}}_2(t)$ will be instead optimized if it lies in $\mathcal{S}_2^+(t)$, the space spanned by the first two Lyapunov vectors. Thus, we must have $\hat{\boldsymbol{\eta}}_2(t) = \hat{p}_{21}\boldsymbol{\phi}_1(t) + \hat{p}_{22}\boldsymbol{\phi}_2(t)$. Recursive application of this argument gives a representation of the asymptotic evolved singular vectors $\hat{\boldsymbol{\eta}}_j(t)$ in terms of the Lyapunov vectors

$$\hat{\boldsymbol{\eta}}_j(t) = \sum_{i=1}^{j} \hat{p}_{ji}\boldsymbol{\phi}_i. \tag{2.20}$$

A similar argument can be made to show that the initial conditions of singular vectors optimized in the distant future $\hat{\boldsymbol{\xi}}_j(t)$ (called 'forward' singular vectors because they are equivalent to Legras and Vautard's 'forward' Lyapunov vectors), where

$$\hat{\boldsymbol{\xi}}_j(t) \equiv \lim_{t_2\to\infty} \boldsymbol{\xi}_j(t;t,t_2), \tag{2.21}$$

are also an orthogonalization of the Lyapunov vectors. In this case, the orthogonalization proceeds upward from the most rapidly decaying Lyapunov vector to obtain

$$\hat{\boldsymbol{\xi}}_j(t) = \sum_{i=j}^{N} \hat{q}_{ji}\boldsymbol{\phi}_i, \tag{2.22}$$

for some coefficients $\hat{q}_{ji}$.

The convergence of the singular vectors to their asymptotic forms is, in fact, exponential. That this is a consequence of asymptotic exponential time-dependence of the Lyapunov vectors made more clear by writing the propagator in terms of the Lyapunov vectors. Let

$$\mathcal{L}(t_2,t_1) = \mathbf{F}(t_2)\mathbf{F}(t_1)^{-1} \tag{2.23}$$

for any t_1, t_2, where $\mathbf{F}$ is a matrix whose columns are the Lyapunov vectors, ordered by decreasing Lyapunov exponent. Since the Lyapunov vectors span the space of linear disturbances, the singular vectors may be written as a fixed sum of Lyapunov vectors,

$$\boldsymbol{\xi}_j(t;t_1,t_2) = \sum_{i=1}^{N} \boldsymbol{\phi}_i(t)p_{ij}(t_1,t_2) = \mathbf{F}(t)\boldsymbol{p}(t_1,t_2). \tag{2.24}$$

The projection coefficients are a function of initialization and optimization time only. With eqs. (2.23) and (2.24), eq. (2.8) becomes

$$\mathbf{F}(t_2)^{\mathrm{T}}\mathbf{N}\mathbf{F}(t_2)\boldsymbol{p}_j = \sigma_j^2\mathbf{F}(t_1)^{\mathrm{T}}\mathbf{N}\mathbf{F}(t_1)\boldsymbol{p}_j. \tag{2.25}$$

For $\tau = t_2 - t_1 \gg 1$, the components of the LHS of eq. (2.25) grow like

$$\left[\mathbf{F}(t_2)^{\mathrm{T}}\mathbf{N}\mathbf{F}(t_2)\right]_{ij} \sim e^{(\lambda_i+\lambda_j)\tau}. \tag{2.26}$$

Thus, as $\tau \to \infty$, the LHS of eq. (2.25) is given with exponential accuracy by a matrix whose only non-zero entry is the upper right corner. The resulting eigensystem has only one nontrivial solution, $\boldsymbol{p}_1$, whose components are $p_{1i} = 0$ except for $i = 1$. The rate of convergence to the asymptotic form is $\mu_1 = |\lambda_2 - \lambda_1|$. The remaining eigenvectors can be recovered by working in the subspace orthogonal to the first, in which the LHS of eq. (2.25) is again given with exponential accuracy by a matrix whose only non-zero entry is the upper right corner. The rate of convergence in this subspace is $|\lambda_3 - \lambda_2|$, but since the rate of convergence *into* this subspace is $|\lambda_2 - \lambda_1|$, the rate of convergence of $\boldsymbol{\xi}_2(t; t_1, t)$ to its asymptotic form $\hat{\boldsymbol{\eta}}_2(t)$ is

$$\mu_2 = \min\left\{|\lambda_3 - \lambda_2|, |\lambda_2 - \lambda_1|\right\}. \tag{2.27}$$

In general, the rate of convergence of $\boldsymbol{\xi}_j(t; t_1, t)$ to its asymptotic form $\hat{\boldsymbol{\eta}}_j(t)$ is

$$\mu_j = \min_{1 \le i \le j} |\lambda_{i+1} - \lambda_i|. \tag{2.28}$$

In a similar manner, it can be shown that the the rate of convergence of $\boldsymbol{\xi}_j(t; t, t_2)$ to its asymptotic form $\hat{\boldsymbol{\xi}}_j(t)$ is

$$\sigma_j = \min_{j \le i \le N} |\lambda_i - \lambda_{i-1}|. \tag{2.29}$$

It should be noted at μ_j and σ_j only give lower bounds on the convergence rate. For example, if two Lyapunov vectors are orthogonal in a given norm, the convergence rate of the corresponding singular vectors in that norm may be faster than the estimates given by μ_j and σ_j. In practice, we find that a good approximation to the true convergence rate is

$$\mu_j = \begin{cases} |\lambda_2 - \lambda_1| & j = 1, \\ \min\left\{|\lambda_{j+1} - \lambda_j|, |\lambda_j - \lambda_{j-1}|\right\} & 1 < j < N, \\ |\lambda_N - \lambda_{N-1}| & j = N, \end{cases} \tag{2.30}$$

Note that, if the Lyapunov spectrum is degenerate, there is no lower bound on the convergence rate and some of the singular vectors may not converge.

2.4 The recovery of Lyapunov vectors from singular vectors

The 'forward' and 'backward' asymptotic singular vectors $\hat{\boldsymbol{\eta}}_j$ and $\hat{\boldsymbol{\xi}}_j$, respectively, furnish two different orthogonalizations of the same Lyapunov vectors. It is possible to use these two orthogonalizations to recover the Lyapunov vectors in a norm-independent manner.

Under fairly general conditions, for each time t, the asymptotic forward and backward singular vectors ($\hat{\boldsymbol{\xi}}_j(t)$ and $\hat{\boldsymbol{\eta}}_j(t)$, respectively) are orthonormal in the specified norm and span the space of the dynamical system. Thus, each $\boldsymbol{\phi}_i(t)$ may be alternately written as a linear combination of the $\hat{\boldsymbol{\xi}}$'s or the $\hat{\boldsymbol{\eta}}$'s. This may be expressed compactly as

$$\mathbf{F} = \mathbf{A}\mathbf{X}, \tag{2.31}$$

$$\mathbf{F} = \mathbf{B}\mathbf{Y}, \tag{2.32}$$

where $\mathbf{F}$, $\mathbf{X}$, and $\mathbf{Y}$ are matrices whose columns are the $\boldsymbol{\phi}$'s, $\hat{\boldsymbol{\xi}}$'s, and $\hat{\boldsymbol{\eta}}$'s, respectively, and the components of the matrices $\mathbf{A}$ and $\mathbf{B}$ are

$$a_{ij} = \langle \boldsymbol{\phi}_i, \hat{\boldsymbol{\xi}}_j \rangle,$$

$$b_{ij} = \langle \boldsymbol{\phi}_i, \hat{\boldsymbol{\eta}}_j \rangle.$$

If we could determine either $\mathbf{A}$ or $\mathbf{B}$, we could determine $\mathbf{F}$ and, thus, the Lyapunov vectors.

The relationships (2.31) and (2.32) may be inverted to find

$$\mathbf{X} = \mathbf{A}^{-1}\mathbf{F}, \tag{2.33}$$

$$\mathbf{Y} = \mathbf{B}^{-1}\mathbf{F}. \tag{2.34}$$

Comparison of eqs. (2.33) and (2.34) with eqs. (2.20) and (2.22) shows that $\mathbf{A}^{-1}$ is an upper triangular matrix with components $\hat{q}_{ji}$ and $\mathbf{B}^{-1}$ is a lower triangular matrix with components $\hat{p}_{ji}$. It follows that $\mathbf{A}$ is upper triangular and $\mathbf{B}$ is lower triangular: $\langle \boldsymbol{\phi}_i, \hat{\boldsymbol{\xi}}_j \rangle = 0$ for $i < j$ and $\langle \boldsymbol{\phi}_i, \hat{\boldsymbol{\eta}}_j \rangle = 0$ for $i > j$. Thus, (2.31) and (2.32) may be written as

$$\boldsymbol{\phi}_n = \sum_{i=n}^{N} \langle \hat{\boldsymbol{\xi}}_i, \boldsymbol{\phi}_n \rangle \hat{\boldsymbol{\xi}}_i, \tag{2.35}$$

$$\boldsymbol{\phi}_n = \sum_{j=1}^{n} \langle \hat{\boldsymbol{\eta}}_j, \boldsymbol{\phi}_n \rangle \hat{\boldsymbol{\eta}}_j, \tag{2.36}$$

where now the dependence of all the vectors on t has been suppressed.

Setting (2.35) and (2.36) equal gives

$$\sum_{j=1}^{n} \langle \hat{\boldsymbol{\eta}}_j, \boldsymbol{\phi}_n \rangle \hat{\boldsymbol{\eta}}_j = \sum_{i=n}^{N} \langle \hat{\boldsymbol{\xi}}_i, \boldsymbol{\phi}_n \rangle \hat{\boldsymbol{\xi}}_i$$

which, upon taking inner products alternately with $\hat{\boldsymbol{\xi}}_k$ and $\hat{\boldsymbol{\eta}}_k$, yields

$$\langle \hat{\boldsymbol{\xi}}_k, \boldsymbol{\phi}_n \rangle = \sum_{j=1}^{n} \langle \hat{\boldsymbol{\eta}}_j, \boldsymbol{\phi}_n \rangle \langle \hat{\boldsymbol{\xi}}_k, \hat{\boldsymbol{\eta}}_j \rangle \quad \text{for } k \geq n, \tag{2.37}$$

$$\langle \hat{\boldsymbol{\eta}}_k, \boldsymbol{\phi}_n \rangle = \sum_{i=n}^{N} \langle \hat{\boldsymbol{\xi}}_i, \boldsymbol{\phi}_n \rangle \langle \hat{\boldsymbol{\eta}}_k, \hat{\boldsymbol{\xi}}_i \rangle \quad \text{for } k \leq n. \tag{2.38}$$

Substitution of (2.37) into (2.38) to eliminate $\langle \hat{\boldsymbol{\xi}}_k, \boldsymbol{\phi}_n \rangle$ yields the following linear system in $\langle \hat{\boldsymbol{\eta}}_k, \boldsymbol{\phi}_n \rangle$:

$$\langle \hat{\boldsymbol{\eta}}_k, \boldsymbol{\phi}_n \rangle = \sum_{j=1}^{n} \left[\sum_{i=n}^{N} \langle \hat{\boldsymbol{\eta}}_k, \hat{\boldsymbol{\xi}}_i \rangle \langle \hat{\boldsymbol{\xi}}_i, \hat{\boldsymbol{\eta}}_j \rangle \right] \langle \hat{\boldsymbol{\eta}}_j, \boldsymbol{\phi}_n \rangle \quad k \leq n. \tag{2.39}$$

The solution to this system gives the expansion coefficients of the Lyapunov vectors in terms of the backward singular vectors which, in turn, determines the Lyapunov vectors themselves. However, the solution of eq. (2.39) for any n requires the knowledge of $N+1$ asymptotic singular vectors and the accuracy of the solution is limited by the accuracy of the singular vector with the slowest slowest convergence rate. If the Lyapunov spectrum is degenerate, convergence of eq. (2.39) is not assured for any finite optimization interval τ.

The bracketed term in eq. (2.39) can be simplified and the convergence problem circumvented by noting that for any two complete orthonormal sets of vectors $\boldsymbol{e}_i$ and $\boldsymbol{f}_i$,

$$\sum_{k=1}^{N} \langle \boldsymbol{f}_i, \boldsymbol{e}_k \rangle \langle \boldsymbol{e}_k, \boldsymbol{f}_j \rangle = \delta_{ij}.$$

Thus,

$$\sum_{i=n}^{N} \langle \hat{\boldsymbol{\eta}}_k, \hat{\boldsymbol{\xi}}_i \rangle \langle \hat{\boldsymbol{\xi}}_i, \hat{\boldsymbol{\eta}}_j \rangle = \delta_{kj} - \sum_{i=1}^{n-1} \langle \hat{\boldsymbol{\eta}}_k, \hat{\boldsymbol{\xi}}_i \rangle \langle \hat{\boldsymbol{\xi}}_i, \hat{\boldsymbol{\eta}}_j \rangle$$

and therefore,

$$\sum_{j=1}^{n} \sum_{i=1}^{n-1} \langle \hat{\boldsymbol{\eta}}_k, \hat{\boldsymbol{\xi}}_i \rangle \langle \hat{\boldsymbol{\xi}}_i, \hat{\boldsymbol{\eta}}_j \rangle \langle \hat{\boldsymbol{\eta}}_j, \boldsymbol{\phi}_n \rangle = 0 \qquad k \leq n. \tag{2.40}$$

That this is indeed a simplification becomes apparent when it is noted that eq. (2.40) involves only the first n (forward and backward) asymptotic singular vectors.

Eq. (2.39) and (2.40) can be cast into a more familiar form by defining

$$y_k^{(n)} = \langle \hat{\boldsymbol{\eta}}_k, \boldsymbol{\phi}_n \rangle \qquad k = 1, 2, \ldots, n, \tag{2.41}$$

$$D_{kj}^{(n)} = \sum_{i=1}^{n-1} \langle \hat{\boldsymbol{\eta}}_k, \hat{\boldsymbol{\xi}}_i \rangle \langle \hat{\boldsymbol{\xi}}_i, \hat{\boldsymbol{\eta}}_j \rangle \qquad k, j \leq n. \tag{2.42}$$

Then eq. (2.40) takes the form

$$\mathbf{D}^{(n)} \boldsymbol{y}^{(n)} = 0, \tag{2.43}$$

and the desired expansion coefficients $\boldsymbol{y}^{(n)}$ are seen to be the null vector of $\mathbf{D}^{(n)}$. The problem (2.43) can thus be solved to obtain the n leading Lyapunov vectors from just the first n forward and n backward singular vectors. In contrast, the expansion (2.39) requires the knowledge of $N+1$ singular vectors. In many ensemble forecasting examples, $2n \ll N+1$.

A similar method for recovering the last n Lyapunov vectors from the last n forward and n backward singular vectors may be obtained by substituting (2.38) into (2.37) to eliminate $\langle \hat{\boldsymbol{\eta}}_k, \boldsymbol{\phi}_n \rangle$ and proceeding as above. The trailing Lyapunov vectors are then the null vectors of

$$\mathbf{C}^{(n)} \boldsymbol{x}^{(n)} = 0, \tag{2.44}$$

where

$$x_k^{(n)} = \langle \hat{\boldsymbol{\xi}}_{k+n-1}, \boldsymbol{\phi}_n \rangle \qquad k = 1, 2, \ldots, N-n+1, \tag{2.45}$$

and

$$C_{ki}^{(n)} = \sum_{j=n+1}^{N} \langle \hat{\boldsymbol{\xi}}_{k+n-1}, \hat{\boldsymbol{\eta}}_j \rangle \langle \hat{\boldsymbol{\eta}}_j, \hat{\boldsymbol{\xi}}_{i+n-1} \rangle \qquad k, i \leq N-n+1. \tag{2.46}$$

The uniqueness of the recovered Lyapunov vectors (the solution to eqs. (2.43) and (2.44)) follows from the uniqueness of the representations (2.35) and (2.36) which, in turn, follows from the completeness of the asymptotic singular vectors and assumed uniqueness of the Lyapunov vectors in question. As discussed in sections 2.2.4 and 2.3, the Lyapunov vectors associated with Lyapunov exponents with multiplicity $m_i > 1$ are not uniquely defined and the above method may produce unpredictable results when applied to these Lyapunov vectors. The extension of these results to the case of degenerate Lyapunov vectors is a subject of future work.

Note that the $\hat{\boldsymbol{\eta}}_j$ could be replaced with *any* orthogonal set of linear disturbances initialized sufficiently far in the past, although the singular vectors are, by definition, optimal. The same is not true for the $\hat{\boldsymbol{\xi}}_j$ since the efficiency of this algorithm depends crucially on the fact that the $\hat{\boldsymbol{\xi}}_j$ are initial conditions which optimize disturbance growth in the future. This is necessary to ensure that the $\hat{\boldsymbol{\xi}}_j$ are a proper orthogonalization of the Lyapunov vectors (i.e., one which proceeds upward from the most rapidly decaying Lyapunov vector). Replacement of the $\hat{\boldsymbol{\xi}}_j$ with a different, non-optimal, set of linear disturbances would require using a complete set of linear disturbances initialized in the distant future and integrated backward to t in order to obtain the correct orthogonalization. Evolving a complete set of linear disturbances would negate the efficiency of this method.

2.5 Numerical examples

2.5.1 Lorenz model

The Lorenz model is perhaps the simplest nontrivial system with which to demonstrate the principles discussed in section 2.3 and the algorithm presented in section 2.4. The development and characteristics of this model are well studied, and the reader is referred to the extensive literature (e.g., Sparrow, 1982) regarding this model for further details. Further, since the linear disturbance dynamics of this model have been discussed in detail by other authors (e.g., Legras and Vautard, 1996; Trevisan and Legnani, 1995; Trevisan and Pancotti, 1998), the present treatment of the Lorenz model will be brief.

We use the standard parameter values $\sigma = 10$, $\rho = 28$, and $\beta = 8/3$, for which the model possesses a strange attractor with Lyapunov exponents

$$\lambda_1 = 0.91 \pm 0.01,$$

$$\lambda_2 = 0,$$

$$\lambda_3 = -14.58 \pm 0.01.$$

That λ_2 is exactly zero is a consequence of the fact that the model equations do not explicitly depend on time. Further, it can be shown that, if the Lyapunov vectors are defined in terms of intersecting forward and backward subspaces (as is section 2.2.4), the second Lyapunov vector $\boldsymbol{\phi}_2$ is proportional to the time derivative (i.e., the tangent vector) of the nonlinear trajectory. Since $\boldsymbol{\phi}_2$ is the only Lyapunov vector that requires a non-trivial application of the method described in section 2.4 for three-dimensional systems, this result will prove to be a useful check of the calculation.

The propagator $\mathcal{L}$ is obtained on a fine temporal grid ($\Delta t = 0.02$) by direct integration of the tangent linearization of the Lorenz equations about a nonlinear, aperiodic trajectory encompassing 8 time units. The singular vectors in the identity norm are then calculated by singular value decomposition of $\mathcal{L}$. The asymptotic forms of the singular vectors are obtained by, at each point in the temporal grid, systematically increasing the optimization interval τ until the singular vectors are constant to within a specified tolerance (here, 10^{-6}). As discussed in section 2.3, the convergence of the singular vectors to their asymptotic forms is expected to be asymptotically exponential. According to the estimate (2.30), the average convergence rate of the first and second singular vectors is expected to be $\lambda_1 - \lambda_2 = \lambda_1$ while the expected average convergence rate of the third singular vector is $\lambda_2 - \lambda_3 = -\lambda_3$. The observed numerical convergence rates (Fig. 2.1) match these expectations quite well.

The Lyapunov vectors $\boldsymbol{\phi}_j$ were calculated from the singular vectors using the method described in section 2.4. The second Lyapunov vector $\boldsymbol{\phi}_2$ was found to subtend an angle of only $0.02° \pm 0.01°$ with the tangent vector of the trajectory. The numerically determined second Lyapunov vector was thus nearly collinear with the tangent vector of the trajectory, which indicated that the algorithm was operating correctly.

The local Lyapunov exponents (LLEs),

$$\mathrm{LLE}_j(t) = \frac{1}{\|\phi_j(t)\|}\frac{d}{dt}\|\phi_j(t)\|, \tag{2.47}$$

of the first two Lyapunov vectors are of comparable magnitude and show marked oscillations in phase with the growth and decay of the underlying trajectory (Fig. 2.2b). The LLE of the last, rapidly decaying, Lyapunov vector shows similar oscillations roughly 180° out of phase with the leading two Lyapunov vectors, indicating that the growth phase of the underlying trajectory is favorable for enhanced transient decay as well as growth. Note that the first two Lyapunov vectors exhibit many periods of so-called 'super-Lyapunov' growth, that is, their local growth rates are larger than the leading Lyapunov exponent. While super-Lyapunov growth is sometimes taken as evidence of non-modal dynamics, the dynamics here are modal by definition. Thus, the normal modes themselves are capable of transient growth exceeding that of the first Lyapunov exponent; only their long-time average growth rate is bounded by the Lyapunov exponents. The relationship between super-Lyapunov growth and modal dynamics is discussed in detail by Trevisan and Pancotti (1998).

The projections of the Lyapunov vectors onto each other also oscillate with the nonlinear trajectory (Fig. 2.2c). The first two Lyapunov vectors are nearly

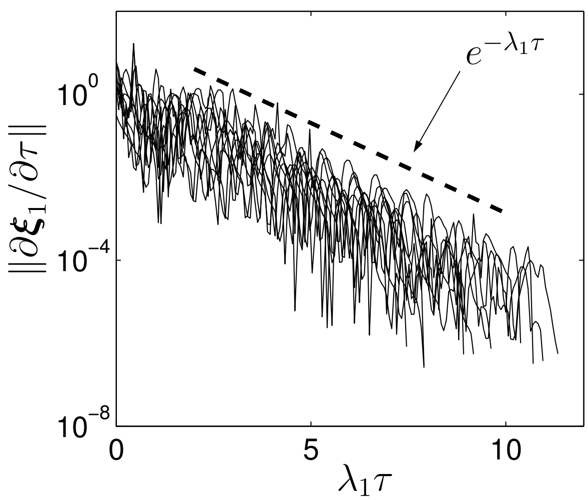

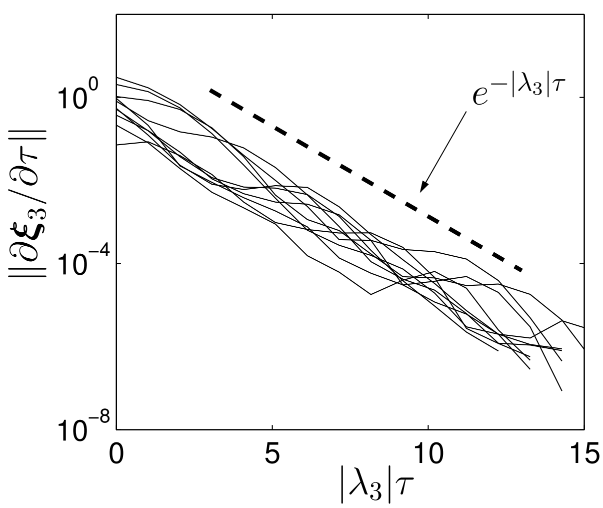

FIGURE 2.1: Norm of the derivative of the first (upper panel) and last (lower panel) forward singular vectors with respect to optimization interval τ as a function of τ for ten different initialization times scattered throughout the attractor. The dotted lines give the expected convergence rates predicted by the Lyapunov exponents of the Lorenz model.

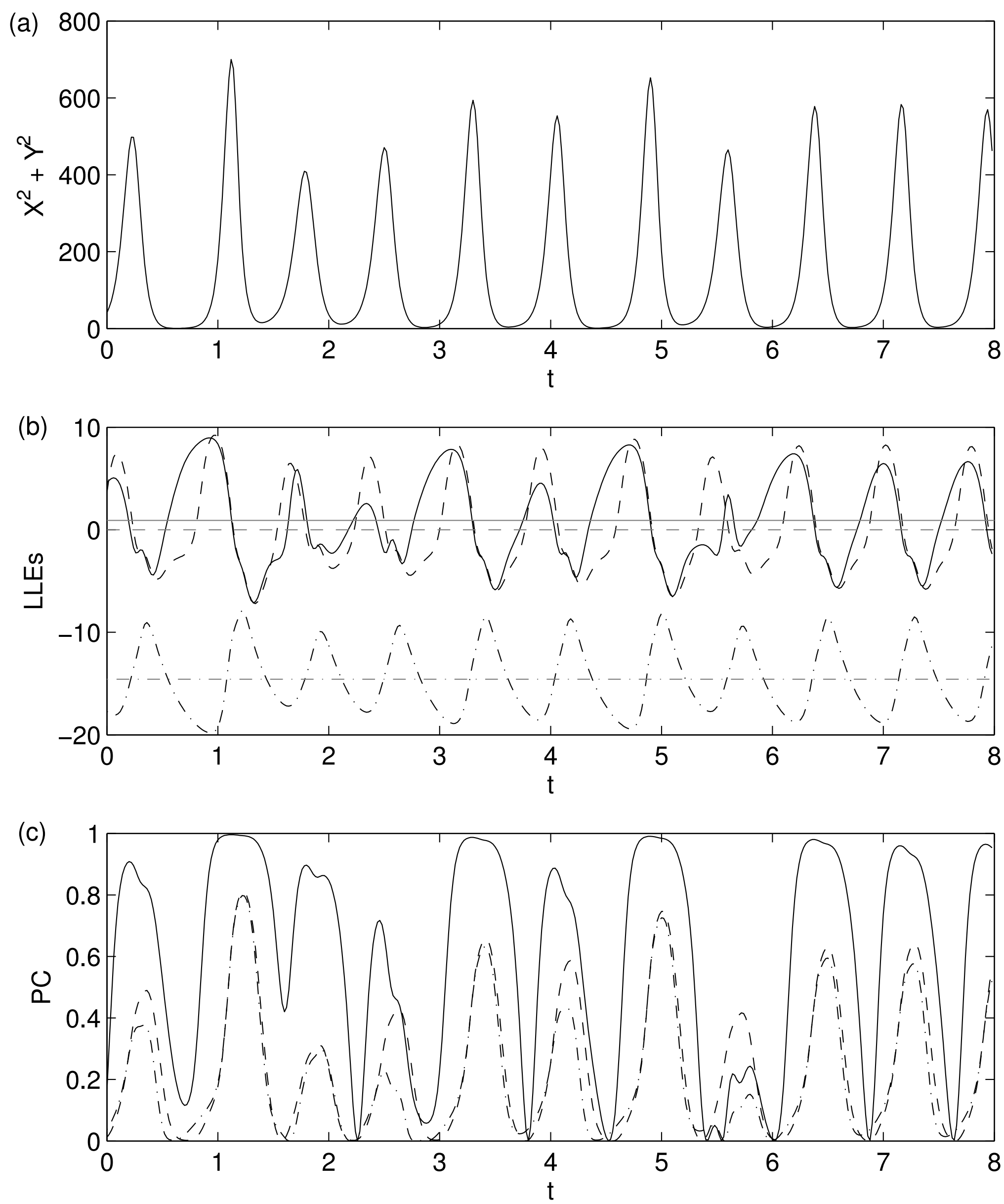

FIGURE 2.2: (a) Background flow amplitude as measured by $X^2 + Y^2$, (b) local Lyapunov exponents (LLEs) of $\boldsymbol{\phi}_1$ (solid), $\boldsymbol{\phi}_2$ (dashed), $\boldsymbol{\phi}_3$ (dash-dot), and (c) pattern correlation between $\boldsymbol{\phi}_1$ and $\boldsymbol{\phi}_2$ (solid), $\boldsymbol{\phi}_2$ and $\boldsymbol{\phi}_3$ (dashed), and $\boldsymbol{\phi}_3$ and $\boldsymbol{\phi}_1$ (dash-dot) as a function of time for the Lorenz model. The horizontal grey lines in (b) give the Lyapunov exponent associated with each Lyapunov vector. Compare (c) to Trevisan and Pancotti (1998), figure 4.

collinear during the trajectory maxima and nearly orthogonal during the trajectory minima. The projections of $\boldsymbol{\phi}_1$ and $\boldsymbol{\phi}_2$ onto the third, decaying, Lyapunov vector $\boldsymbol{\phi}_3$ are of similar magnitude and are generally smaller than their projections onto each other. The time evolution of the projections are very similar to that found by Trevisan and Pancotti (1998), although the detailed behavior is different because those authors focused on a time-periodic trajectory of the Lorenz model while the current trajectory is aperiodic.

2.5.2 Weakly nonlinear Phillips model

The weakly nonlinear Phillips model of the baroclinic instability (Pedlosky, 1971) can be formally considered to be an extension of the Lorenz model (Pedlosky and Frenzen, 1980). It has the advantage of being a consistent asymptotic limit of a geophysical process, whereas the Lorenz equations result from an ad hoc truncation of the equations of motion. This enables us to interpret the convergence time-scale of the singular vectors in terms of a physically relevant time-scale.

The weakly nonlinear model is described in detail in Pedlosky (1987, section 7.16). It takes the form of a system of nonlinear ordinary differential equations for the amplitude A (proportional to the barotropic streamfunction) and inter-layer phase shift B (proportional to the baroclinic streamfunction) of a baroclinic wave. The presence of the wave induces a change in the zonal mean flow which is described by the mean flow corrections V_j. While there are, in principle, an infinite number of mean flow correction terms, in practice, only a finite number J are retained. We use $J = 6$, the same value used by Samelson (2001a,b); the system considered here is thus 8-dimensional. The behavior of the model is controlled by three parameters: the zonal and meridional wavenumbers (k, m) of the fundamental wave and the dissipation parameter γ. For $(k, m) = (\pi, 1)$ and $\gamma = 0.1315$, the model undergoes a baroclinic wave-mean oscillation of chaotically vacillating amplitude with mean period $T_p \approx 24.4$ (for details, see Samelson, 2001a,b).

Direct calculation of the Lyapunov exponents λ_i, using standard methods (e.g., Bennetin et al., 1980), yields

$$\begin{aligned}
\lambda_1 &= 0.0178 \pm 0.0002, \\
\lambda_2 &= 0, \\
\lambda_3 &= -0.0797 \pm 0.0001, \\
\lambda_8 &= -0.2877 \pm 0.0002,
\end{aligned}$$

while $\lambda_i \approx -\gamma$ for $i = 4, 5, 6, 7$. The differences between the exponents λ_4 through λ_7 are thus small and, by the convergence rate estimate (2.30), the corresponding singular vectors can be expected to converge very slowly. The other singular vectors show a range of expected convergence times, from about a quarter period for $\hat{\boldsymbol{\xi}}_8$ to more than $2.5T_p$ for $\hat{\boldsymbol{\xi}}_1$ and $\hat{\boldsymbol{\xi}}_2$. The expected convergence time for singular vectors $\hat{\boldsymbol{\xi}}_4$ through $\hat{\boldsymbol{\xi}}_7$ is greater than $10T_p$ (Fig. 2.3), and we therefore omit calculating $\hat{\boldsymbol{\xi}}_4$ through $\hat{\boldsymbol{\xi}}_7$.

The asymptotic singular vectors $\hat{\boldsymbol{\xi}}_1$, $\hat{\boldsymbol{\xi}}_2$, $\hat{\boldsymbol{\xi}}_3$, and $\hat{\boldsymbol{\xi}}_8$ in the identity norm were calculated on a coarse temporal grid ($\Delta t = 5$) using the same method as in section 2.5.1, with a convergence tolerance of 10^{-4}. The singular vectors converged to their asymptotic forms slightly faster than predicted (Fig. 2.3).

The first three Lyapunov vectors were recovered from the asymptotic singular vector on the coarse grid using the method of section 2.4. Integration of the tangent linear equations using the recovered Lyapunov vectors as initial conditions was used to determine the Lyapunov vectors on a refined temporal grid ($\Delta t = 0.1$). The

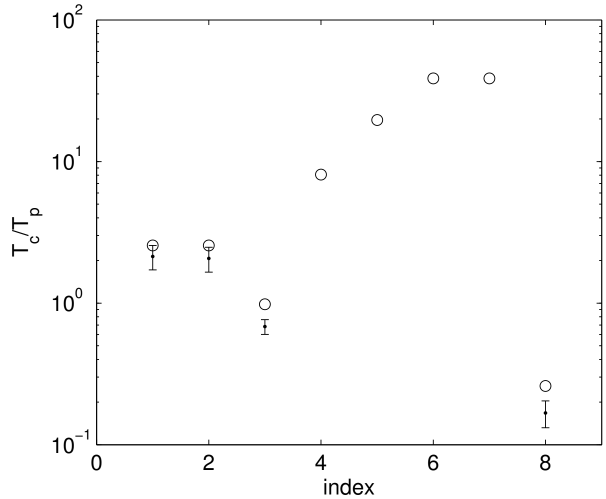

FIGURE 2.3: Singular vector convergence e-folding time T_c relative to the mean period of the baroclinic wave-mean oscillation T_p for the weakly nonlinear Phillips model. Circles give the expected convergence time based on the Lyapunov exponents, dots give the average measured convergence time (based on a fit to an exponential) for ten initial randomly chosen initial conditions, and the error bars give the standard deviation. The asymptotic forms were not calculated for singular vectors 4–7.

advantage of this method was two-fold: First, it allowed the transient growth and decay of the Lyapunov vectors to be determined (the method of section 2.4 cannot determine the amplitude of the Lyapunov vectors). Second, integration of the tangent linear equations was much more efficient than calculating asymptotic singular vectors on a fine temporal grid. Since the Lyapunov vectors were not determined to perfect accuracy, the tangent linear integration could be performed for only a finite time before all of the vectors began to rotate toward the leading Lyapunov vector. It was found, through trail-and-error, that restarting the tangent linear integration every $\Delta t = 5$ gave a good trade-off between accuracy and computational effort. The resulting Lyapunov vectors grew or decayed at the correct rate, as given by the Lyapunov exponents (Fig. 2.4). Further, the second Lyapunov vector $\boldsymbol{\phi}_2$ tracked the transient growth and decay of the tangent to the background trajectory

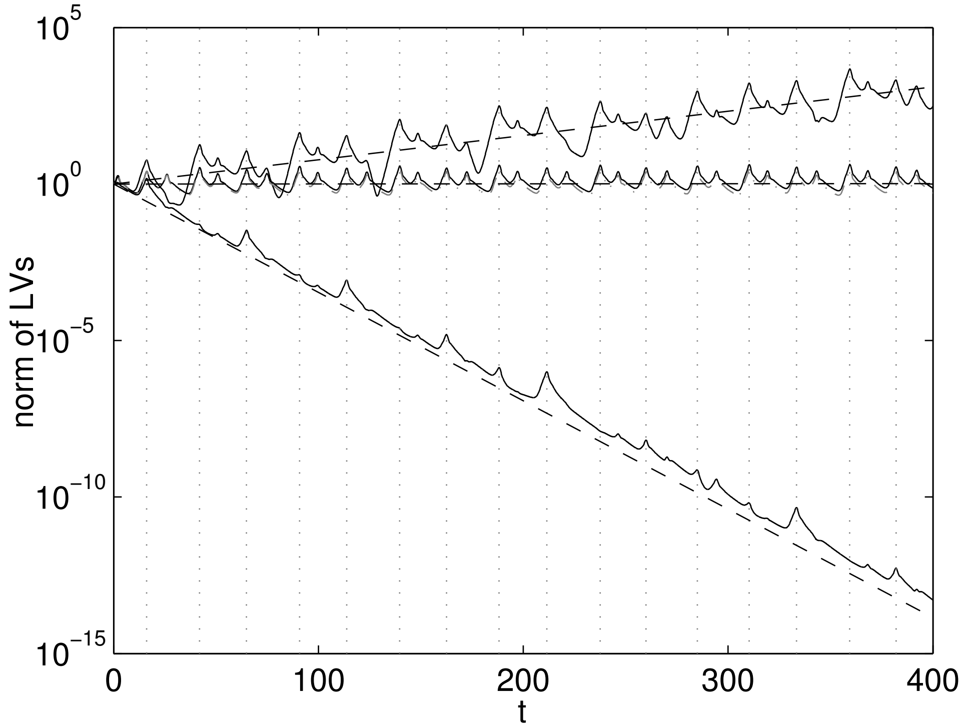

FIGURE 2.4: Norm of the first three Lyapunov vectors (solid) and the tangent to the background trajectory (dash-dot, gray) as a function of time. The expected exponential growth calculated from the Lyapunov exponents is shown for reference (dashed). Vertical dotted lines give the location of the Poincaré section $B = \gamma A$, $A > 0$.

quite well (gray dash-dotted line in fig. 2.4). It should be noted that the decaying Lyapunov vector $\boldsymbol{\phi}_3$ could not have been obtained by long forward or backward integration (which gives only the first or last Lyapunov vectors, respectively), nor could it have been obtained using the straightforward extension of the method presented in Trevisan and Pancotti (1998) due to the unavailability of the asymptotic singular vectors $\hat{\boldsymbol{\xi}}_4$ through $\hat{\boldsymbol{\xi}}_7$.

The leading three Lyapunov vectors give an interesting picture of the dynamics of linear disturbances to the aperiodic trajectory. $\boldsymbol{\phi}_2$, since it is proportional to the time-derivative of the background trajectory, grows and decays in phase with the growth and decay phases of the background trajectory (Fig. 2.5b) and directly reflects the dynamics of the aperiodic trajectory itself. $\boldsymbol{\phi}_1$ and $\boldsymbol{\phi}_3$ have similar local growth rates and grow and decay roughly in phase with $\boldsymbol{\phi}_2$; there are, however, important differences. $\boldsymbol{\phi}_1$ goes through periods of high and low activity which are associated with times when the background trajectory achieves relatively high or low amplitude, respectively, on the Poincaré section $B = \gamma A$, $A > 0$ (compare fig. 2.5a with fig. 2.5b). In contrast, $\boldsymbol{\phi}_3$ is most active when $\boldsymbol{\phi}_1$ is least active.

The projections of the Lyapunov vectors onto each other are of interest because systems with highly non-orthogonal Lyapunov vectors are capable of rapid transient growth due to the interference of the Lyapunov vectors (Farrell and Ioannou, 1996). Following a high-activity period, $\boldsymbol{\phi}_1$ spends an extended period of time nearly collinear with $\boldsymbol{\phi}_2$ (Fig. 2.5c). Thus, while disturbances with strong projections onto $\boldsymbol{\phi}_1$ will grow during a high-activity period simply because $\boldsymbol{\phi}_1$ is growing, disturbances made after a high-activity period may still grow through interference of $\boldsymbol{\phi}_1$ and $\boldsymbol{\phi}_2$, even when all of the LLEs are negative. The temporal evolution of the projection of $\boldsymbol{\phi}_1$ onto $\boldsymbol{\phi}_2$ is more structured following a low-activity period and contains several periods of orthogonality (Fig. 2.5c). The projections of both $\boldsymbol{\phi}_1$ and $\boldsymbol{\phi}_2$ onto $\boldsymbol{\phi}_3$ are of similar magnitude and generally smaller than their projections onto each other. However, all three Lyapunov vectors are nearly orthogonal approximately 5 time units ahead of a low-activity Poincaré section but rotate to become nearly collinear on the low-activity Poincaré sections ($t \approx 0, 50, 100$).

The above observations were derived from a short segment of an aperiodic trajectory. In order to test if they held more generally, Lyapunov vectors where calculated from a long trajectory ($T = 20\,000$) at equal intervals of $\Delta t = 5$. 4000 points was sufficient to give good coverage of the attractor, which may be conve-

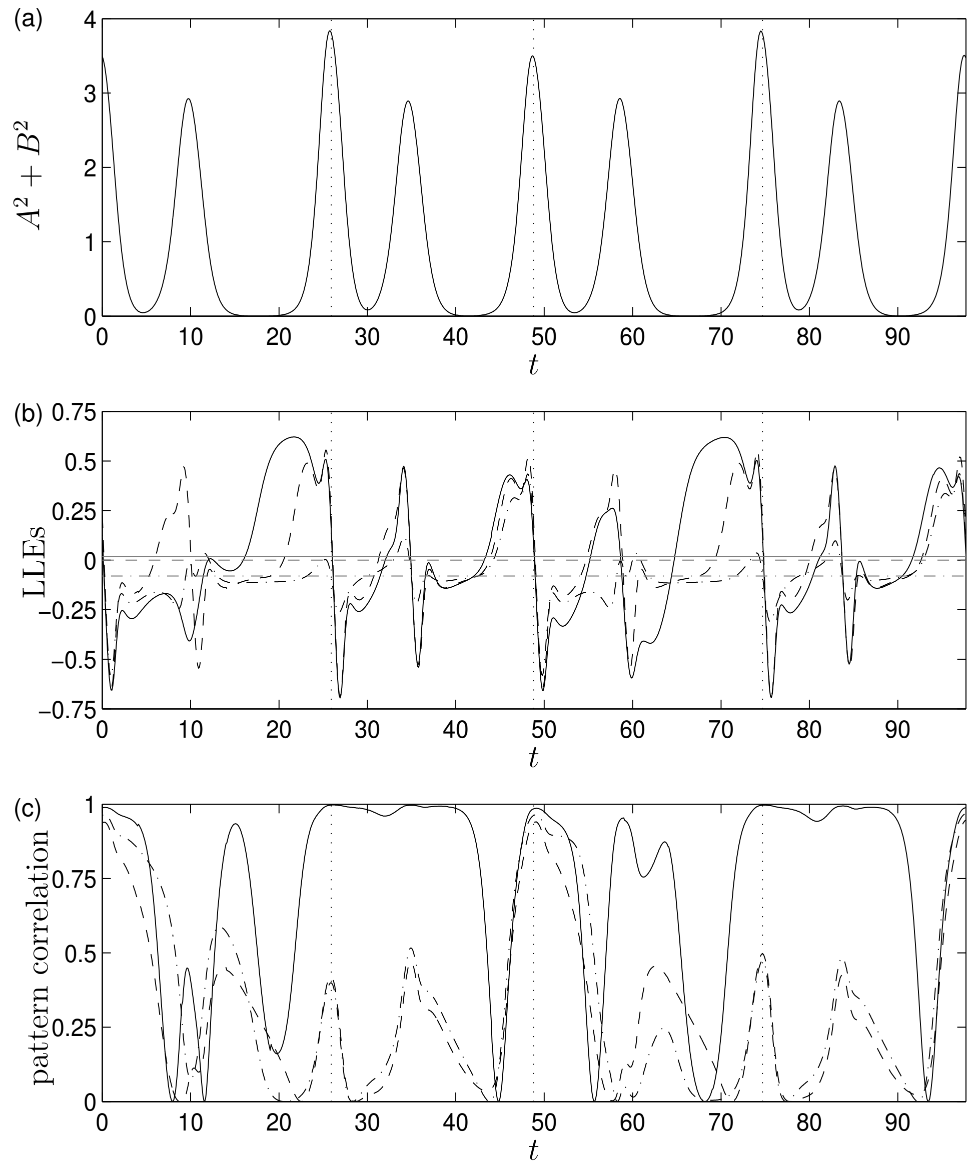

FIGURE 2.5: (a) Background flow 'energy' as measured by $A^2 + B^2$, (b) local Lyapunov exponents (LLEs) of $\boldsymbol{\phi}_1$ (solid), $\boldsymbol{\phi}_2$ (dashed), $\boldsymbol{\phi}_3$ (dash-dot), and (c) pattern correlation between $\boldsymbol{\phi}_1$ and $\boldsymbol{\phi}_2$ (solid), $\boldsymbol{\phi}_2$ and $\boldsymbol{\phi}_3$ (dashed), and $\boldsymbol{\phi}_3$ and $\boldsymbol{\phi}_1$ (dash-dot) as a function of time for the same time interval as figure 2.4. The horizontal grey lines in (b) give the Lyapunov exponent associated with each Lyapunov vector. Vertical dotted lines give the location of the Poincaré section $B = \gamma A$, $A > 0$.

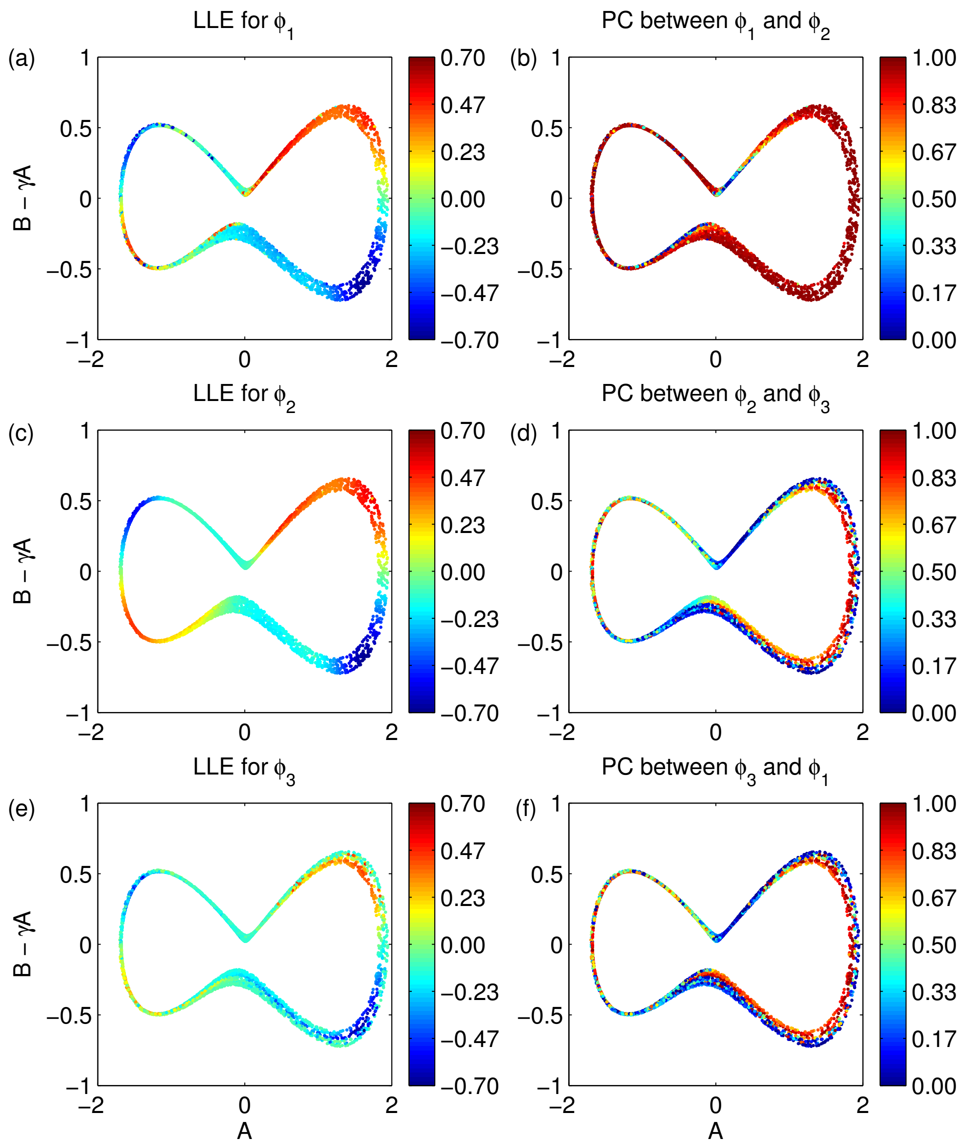

FIGURE 2.6: Scatter plots of A vs. $B-\gamma A$ at 4000 equally spaced times. Colors give the local Lyapunov exponent (left panels) and pattern correlations (right panels) at each time.

niently visualized in the $(A, B - \gamma A)$ plane (Fig. 2.6). In this representation, the wave-mean oscillation takes the form of a 'dog-bone' shaped structure. The sense of motion on the attractor is clockwise. The amplitude vacillation is strongest on the right-hand side of the dog-bone, where the trajectories show the most spread. Most of the following discussion will focus on this region of the attractor.

The Lyapunov vector $\boldsymbol{\phi}_2$, which is proportional to the time-derivative of the aperiodic trajectory, grows and decays as the background trajectory grows and decays and shows little variation transverse to the attractor (Fig. 2.6c). The growth of $\boldsymbol{\phi}_1$ starts earlier than that of $\boldsymbol{\phi}_2$ and is slightly stronger on the 'outside' edge of the attractor (Fig. 2.6a); thus, the high-activity phases of $\boldsymbol{\phi}_1$ coincide with the high-amplitude phases of the background trajectory. In contrast, growth of $\boldsymbol{\phi}_3$ is weaker and starts later than the growth of $\boldsymbol{\phi}_2$ (Fig. 2.6e). Both growth and decay of $\boldsymbol{\phi}_3$ are strongest on the inside edge of the attractor.

The behavior of the projections between the Lyapunov vectors is similar, in general, to that deduced from the short aperiodic segment. The first two Lyapunov vectors are nearly collinear at most points on the attractor, with a brief episode of near-orthogonality near the beginning of the right-hand growth cycle (Fig. 2.6b). There is an addition region of near-orthogonality near the beginning of the left-hand growth cycle, but this region is localized on the inward-facing part of the attractor. Thus, a period of near-orthogonality follows a low-amplitude phase, but not a high amplitude phase. The projections of both $\boldsymbol{\phi}_1$ and $\boldsymbol{\phi}_2$ onto $\boldsymbol{\phi}_3$ are again of similar magnitude and generally smaller than their projections onto each other, with near-orthogonality prevalent during high-amplitude phases and near-collinearity prevalent during low-amplitude phases.

2.6 Discussion

The method described in this paper allows the first n Lyapunov vectors to be constructed in a norm-independent manner from the first n asymptotic forward and backward singular vectors. The method has been demonstrated here for two idealized geophysical examples and are found to provide a useful picture of the phase-space dynamics of linear disturbances.

Several studies have successfully used the leading Lyapunov vector to understand the physics of aperiodic flow and the maintenance of chaotic behavior (e.g., Vastano and Moser, 1991; Vannitsem and Nicolis, 1997; Wei and Frederiksen, 2004). Even though Lyapunov exponents and thus Lyapunov vectors are defined asymptotically, Lyapunov vectors can be surprising useful for understanding short-time dynamics, such has transient error growth (Trevisan and Pancotti, 1998). Next-to-leading and even decaying Floquet vectors capture interesting dynamical processes in time-periodic systems (Wolfe and Samelson, 2006). As demonstrated in section 2.5.2 non-leading, but norm-independent, Lyapunov vectors are be similarly useful in the analysis of aperiodic flow. The algorithm presented here allows these Lyapunov vectors to be obtained in an efficient manner.

It is interesting to consider whether a version of this method might be obtained to estimate atmospheric Lyapunov vectors from operational forecast models, for which forward singular vectors are routinely calculated (e.g., Buizza and Palmer, 1995). It should be noted that the ensemble initialization cycle usually includes an analysis phase which adjusts the nonlinear trajectory in a manner which may be inconsistent with the dynamical equations, and the effect of this on the convergence of the singular vectors is not yet known.

A practical obstacle to the extraction of atmospheric Lyapunov vectors from operational singular vectors will be the limited degree to which operational singular vectors can be considered asymptotic, as the simple baroclinic wave example suggests that the required optimization times may span more than one baroclinic life cycle. However, the method may still yield interesting approximate results and future work may lead to useful extensions and refinements of the approach.

2.7 Acknowledgement

The authors gratefully acknowledge the Office Naval Research, Grants N00014-98-1-0813 and N00014-06-1-0369, Code 322 OM, for support of this work. The suggestions of two anonymous referees substantially improved this text.

2.8 References

Bennetin, G., L. Galgani, A. Giorgilli, and J.-M. Strelcyn, 1980: Lyapunov characteristic exponents for smooth dynamical systems and for Hamiltonian systems: A method for computing all of them. *Meccanica*, **15**, 9–21.

Buizza, R., P. L. Houtekamer, Z. Toth, G. Pellerin, M. Wei, Y. B. Zhu, L. Galgani, A. Giorgilli, and J.-M. Strelcyn, 2005: A comparison of the ECMWF, MSC and NCEP global ensemble prediction systems. *Mon. Wea. Rev.*, **133**, 1076–1097.

Buizza, R. and T. Palmer, 1995: The singular vector structure of the atmospheric general circulation. *J. Atmos. Sci.*, **52**, 1434–1456.

Coddington, E. A. and N. Levinson, 1955: *Theory of Ordinary Differential Equations*. Krieger Publishing Company.

Drazin, P. G. and W. H. Reid, 2004: *Hydrodynamical Stability*. Cambridge University Press, Cambridge, UK, second edition.

Eckmann, J.-P. and D. Ruelle, 1985: Ergodic theory of chaos and strange attractors. *Rev. Mod. Phys.*, **57**, 617–656.

Farrell, B. F., 1989: Optimal excitation of baroclinic waves. *J. Atmos. Sci.*, **46**, 1193–1206.

Farrell, B. F. and P. J. Ioannou, 1996: Generalized stability theory part I: autonomous operators. *J. Atmos. Sci.*, **53**, 2025–2040.

Frederiksen, J. S., 1997: Adjoint sensitivity and finite-time normal mode disturbances during blocking. *J. Atmos. Sci.*, **54**, 1144–1165.

Goldhirsch, I., P. L. Sulem, and A. Orszag, 1987: Stability and lyapunov stability of dynamical systems: a differential approach and a numerical method. *Phyisca D*, **27**, 311–337.

Golub, G. H. and C. F. Van Loan, 1996: *Matrix Computations*. The Johns Hopkins University Press Ltd, London, 3rd edition edition.

Legras, B. and R. Vautard, 1996: A guide to Liapunov vectors. *Predictability, Volume I*, European Centre for Medium-Range Weather Forecasts, 143–156.

Lorenz, E. N., 1963: Deterministic non-periodic flow. *J. Atmos. Sci.*, **20**, 130–141.

— 1965: A study of the predictability of a 28-variable atmospheric model. *Tellus*, **17**, 321–333.

— 1984: The local structure of a chaotic attractor in four dimensions. *Physica D*, **13**, 90–104.

Oseledec, V., 1968: A multiplicative ergodic theorem. Lyapunov characteristic numbers for dynamical systems. *Trans. Moscow Math. Soc.*, **19**, 179–210.

Pedlosky, J., 1971: Finite-amplitude baroclinic waves with small dissipation. *J. Phys. Oceanogr.*, **28**, 587–597.

— 1987: *Geophysical Fluid Dynamics*. Springer, second edition.

Pedlosky, J. and C. Frenzen, 1980: Chaotic and periodic behavior of finite-amplitude baroclinic waves. *J. Atmos. Sci.*, **37**, 1177–1196.

Samelson, R. M., 2001a: Lyapunov, floquet, and singular vectors for baroclinic waves. *Nonlinear Processes Geophys.*, **8**, 439–448.

— 2001b: Periodic orbits and disturbance growth for baroclinic waves. *J. Atmos. Sci.*, **58**, 436–450.

Shimada, I. and T. Nagashima, 1979: A numerical approach to the ergodic problem of dissipative dynamical systems. *Prog. Theor. Phys.*, **61**, 1605–1616.

Sparrow, C., 1982: *The Lorenz Equations: Bifurcations, Chaos, and Strange Attractors*. Springer-Verlag.

Trevisan, A. and R. Legnani, 1995: Transient error growth and local predictability: a study of the Lorenz system. *Tellus*, **47A**, 103–117.

Trevisan, A. and F. Pancotti, 1998: Periodic orbits, Lyapunov vectors, and singular vectors in the Lorenz system. *J. Atmos. Sci.*, **55**, 390–398.

Vannitsem, S. and C. Nicolis, 1997: Lyapunov vectors and error growth patterns in a T21L3 quasigeostrophic model. *J. Atmos. Sci.*, **54**, 357–361.

Vastano, J. A. and R. D. Moser, 1991: Short-time Lyapunov exponent analysis and the transition to chaos in Taylor-Couette flow. *J. Fluid Mech.*, **233**, 83–118.

Wei, M. and J. S. Frederiksen, 2004: Error growth and dynamical vectors during southern hemisphere blocking. *Nonlinear Processes Geophys.*, **11**, 99–118.

Wolfe, C. L. and R. M. Samelson, 2006: Normal-mode analysis of a baroclinic wave-mean oscillation. *J. Atmos. Sci.*, in press.

Yoden, S. and M. Nomura, 1993: Finite time lyapunov stability analysis and its application to atmospheric predictability. *J. Atmos. Sci.*, **50**, 1531–1543.

3 NORMAL-MODE ANALYSIS OF A BAROCLINIC WAVE-MEAN OSCILLATION

Christopher L. Wolfe and Roger M. Samelson

Journal of the Atmospheric Sciences

American Meteorological Society

45 Beacon Street

Boston, MA 02108

In press

3.1 Introduction

The stability theory of geophysical flows has traditionally focused on stationary flows. While great strides toward understanding the variability of the atmosphere and oceans have been made by studying stationary flows (e.g., Charney, 1947; Eady, 1949), the assumption of stationarity is clearly an artifice since all physical flows exhibit time-variability on a range of scales, from the sub-inertial to the millennial. It is thus desirable to relax the stationarity assumption and it is expected that a stability theory of time-dependent flows will allow similar fundamental insights into atmospheric and oceanic variability. A time-dependent stability theory is also of great interest to the forecasting community, as a significant portion of the forecast error at moderate lead times is ascribed to large-scale instabilities growing on the evolving flow (Toth and Kalnay, 1993, 1997).

An important first step toward a stability theory of flows with arbitrary time-dependence is the study of time-periodic flows. Time-periodic flows offer many of the same challenges—and potential for new insights—as flows with arbitrary time-dependence, but are more computationally tractable since full information about the evolution of disturbances to a time-periodic flow may be obtained by model integration over a single period. A number of recent studies have examined periodic flows in geophysical models (Itoh and Kimoto, 1996; Kazantsev, 1998, 2001) and their stability (Samelson, 2001b; Pedlosky and Thomson, 2003; Poulin et al., 2003). Samelson and Wolfe (2003, hereafter SW03), reported some preliminary results concerning the model currently under study.

The present study gives the first complete numerical normal-mode analysis of the linear stability of a strongly nonlinear wave-mean oscillation in a two-layer channel model of the baroclinic instability. Although unstable, the basic wave-mean oscillation is periodic in time. The time-dependent normal modes (Floquet vectors) of a time-periodic flow can be obtained numerically using standard methods for the solution of linear differential equations with periodic coefficients (e.g., Coddington and Levinson, 1955, chap. 3). As for steady parallel flow, these normal modes are intrinsic dynamical objects that can provide physical insight into the mechanisms of disturbance growth and decay.

The mathematical elements of stability theory for steady parallel flow generally involve solutions to ordinary differential equations and are well known for many geophysically relevant examples (e.g., Drazin and Reid, 2004, chap. 4). Along with regular normal modes, they sometimes require singular neutral modes, which may fail to be continuously differentiable, for a complete description of the disturbance evolution. When the basic flow is both time-periodic and non-parallel, the normal-mode problem is generally non-separable. The corresponding mathematical theory for the Floquet analysis of partial differential equations is not as well established as that for ordinary differential equations, although some results are available (Kuchment, 1993). For example, the possibility that analogs of singular neutral modes may exist in such flows has received limited attention. One goal of the present study is to examine this possibility in a specific geophysical model.

The format of the paper is as follows: In section 3.2, we discuss the model formulation and review some basic elements of Floquet theory. We then briefly describe the basic wave-mean oscillation and its relation to the general behavior of the model in section 3.3. Section 3.4 is devoted to a detailed discussion of the results of the Floquet analysis. The sensitivity of the results to changes in resolution are discussed in section 3.5. The significance of the results are discussed in section 3.6.

Finally, we summarize in section 3.7.

3.2 Formulation

3.2.1 Model

The model studied here is the well known Phillips (1954) quasi-geostrophic channel model and is described extensively in Pedlosky (1987, chap. 7). For the present study, the Coriolis parameter f is constant, the equilibrium layer depths are equal, and the background flow is steady, uniform, and zonal. The evolution of disturbances to the background flow is governed by

$$\frac{\partial q_n}{\partial t} + U_n \frac{\partial q_n}{\partial x} + J(\psi_n, q_n) - (-1)^n F U_s \frac{\partial \psi_n}{\partial x} = -r\nabla^2 \psi_n \qquad n = 1, 2, \tag{3.1}$$

where the ψ_n and q_n are the disturbance streamfunctions and potential vorticities, respectively, and the background flow has been chosen so that $U_1 = -U_2 = U_s/2$. The two parameters controlling the behavior of the system are the Froude number F and the Ekman dissipation parameter r. (Note that we have absorbed a factor of two which appears in Pedlosky (1987, chap. 7) into the definition of r.)

These equations are solved in a periodic channel of nondimensional zonal and meridional extents 2 and 1, respectively. This is the same geometry as that studied by Klein and Pedlosky (1986). The disturbance streamfunctions are represented using the spectral expansion

$$\psi_n(x, y, t) = \sum_{|k|=1}^{N_k} \sum_{l=1}^{N_l} {A_{kl}}^n(t) e^{i\pi k x} \sin l\pi y + \sum_{l=1}^{N_l} {A_{0l}}^n(t) \cos l\pi y, \tag{3.2}$$

where ${A_{-kl}}^n = \overline{{A_{kl}}^n}$ since ψ_n is real. The linear terms in eq. (3.1) are evaluated directly, while the Jacobian term is evaluated on the physical grid. The time-differencing algorithm is Runge-Kutta order two, unless otherwise noted. The primary results of this paper were obtained using $N_x = 72$ zonal and $N_y = 62$ meridional grid points (note $N_k \equiv N_x/2 + 1,\ N_l \equiv N_y$), for a total of 8928 variables, and a time step of $\Delta t = 0.003$. Numerical convergence properties are discussed in section 3.5.

The evolution of linear disturbances to an arbitrary basic flow (ψ_n, q_n) satisfying eq. (3.1) is governed by

$$\underbrace{\frac{\partial q_n'}{\partial t}}_{\text{A}} + \underbrace{U_n \frac{\partial q_n'}{\partial x} + J(\psi_n, q_n')}_{\text{B}} - \underbrace{(-1)^n F U_s \frac{\partial \psi_n'}{\partial x} + J(\psi_n', q_n)}_{\text{C}} = -\underbrace{r\nabla^2 \psi_n'}_{\text{D}} \quad n = 1, 2, \tag{3.3}$$

where ψ_n' and q_n' are the perturbation streamfunctions and potential vorticities, respectively. The labeled terms in the above equation represent (A) local change of disturbance PV, (B) advection of disturbance PV by the background flow, (C) advection of background PV by the disturbance flow, and (D) Ekman dissipation of the disturbance flow. These term labels will appear in the term-balance analysis of section 3.4. Equation (3.3) is solved using the same spectral decomposition used to solve equation (3.1).

Note that equations (3.1) and (3.3) are invariant under the exchanges

$$\begin{cases} \psi_1(x) \to -\psi_2(-x), \\ \psi_2(x) \to -\psi_1(-x), \end{cases} \tag{3.4}$$

$$\begin{cases} \psi_1'(x) \to \pm\psi_2'(-x), \\ \psi_2'(x) \to \pm\psi_1'(-x). \end{cases} \tag{3.5}$$

The existence of these symmetries implies that there exist solutions to the evolution equations with the same properties. The nonlinear solutions discussed in section 3.3

satisfy the symmetry (3.4) exactly, as does the basic cycle. Additionally, most of the Floquet vectors described in section 3.4 satisfy one of the two symmetries (3.5).

3.2.2 Floquet Theory

When the basic flow (ψ_n, q_n) is T-periodic, equation (3.3) is a linear, homogeneous partial differential equation with T-periodic coefficients which, after expansion into zonal and meridional Fourier modes, is amenable to analysis using Floquet theory. Floquet's theorem (Coddington and Levinson, 1955, chap. 3) states that any solution to the truncated spectral expansion of eq. (3.3) may be written as a fixed sum of the $2N_xN_y$ Floquet eigenvectors $\Phi_n^j(x,y,t)$, where (for non-degenerate systems) $\Phi_n^j(x,y,t) = \phi_n^j(x,y,t)e^{\lambda_j t}$. The Floquet structure function $\phi_n^j(x,y,t)$ is T-(or $2T$-)periodic and affects the transient growth and decay of the Floquet vector, while the (possibly complex) Floquet exponent λ_j determines the asymptotic stability of the vector. If $\mathrm{Im}\,[\lambda_j]\,T/2\pi$ is a rational number of the form p/q (where $p > 0$, and p and q are relatively prime), then the real and imaginary parts of $\phi^j(t)e^{i\mathrm{Im}[\lambda_j]t}$ have period qT. If $\mathrm{Im}\,[\lambda_j]\,T/2\pi$ is irrational, then the real and imaginary parts of $\phi^j(t)e^{i\mathrm{Im}[\lambda_j]t}$ are quasi-periodic. Since eq. (3.3) is unchanged by complex conjugation, complex Floquet vectors necessarily come in conjugate pairs.

The Floquet vectors were calculated by integrating a complete set of initial conditions to eq. (3.3) over one period T of a periodic basic cycle to construct the monodromy matrix $\mathbf{M}$. In practice, $\mathbf{M}$ was non-degenerate. The eigenvectors and eigenvalues of $\mathbf{M}$ are the Floquet vectors $\Phi_n^j(x,y,t)$ and the so-called Floquet multipliers μ_j, respectively. The Floquet exponents are given by $\lambda_j = \frac{1}{T}\log\mu_j$. The number of operations required to compute $\mathbf{M}$ grows like N^5, so that increasing the model resolution by a factor of two increases the computational burden of the

Floquet calculation by a factor of 32. There exist methods for computing subsets of the Floquet vectors iteratively (e.g., Lust et al., 1998); a calculation which scales like N^3 per Floquet vector. These methods were used to obtain some of the results discussed in SW03, however, our present interest in obtaining a complete set of Floquet vectors precludes the use of such methods.

As Floquet exponents characterize the asymptotic growth of disturbances to a periodic trajectory, they are intimately related to the Lyapunov exponents of that trajectory. Consider an arbitrary linear disturbance $\boldsymbol{\xi}_0$ to a trajectory $\boldsymbol{x}(t)$ of an N-dimensional dynamical system. Under fairly general conditions (primarily, that $\boldsymbol{x}(t)$ exists and is bounded as $t \rightarrow \pm\infty$), the limit

$$\chi^{\pm} = \lim_{t\rightarrow\pm\infty} \frac{1}{t} \ln \frac{\|\boldsymbol{\xi}(t)\|}{\|\boldsymbol{\xi}_0\|} \tag{3.6}$$

exists and is finite (Oseledec, 1968). Further $\chi^+ = \lambda_1^+$ (the leading forward Lyapunov exponent) independent of $\boldsymbol{\xi}_0$, unless $\boldsymbol{\xi}_0$ belongs to a set $\mathcal{S}_2^+$ of measure zero . If $\boldsymbol{\xi}_0 \in \mathcal{S}_2$, then $\chi^+ = \lambda_2^+ < \lambda_1^+$, where λ_2^+ is the second forward Lyapunov exponent, unless—again—$\boldsymbol{\xi}_{\mathbf{0}}$ belongs to a set $\mathcal{S}_3^+$ of measure zero relative to $\mathcal{S}_2^+$. This argument may be applied recursively to obtain M nested subspaces $\{\mathcal{S}_n^+\}$, each associated with a forward Lyapunov exponent λ_n^+, where $M \leq N$ and $\lambda_{n+1}^+ < \lambda_n^+$. Similar set of M nested subspaces $\{\mathcal{S}_n^-\}$ is obtained as $t \rightarrow -\infty$, with an associated set of backward Lyapunov exponents λ_n^-, where $\lambda_n^- = -\lambda_{M-n+1}^+$. If the intersection space $\mathcal{S}_n = \mathcal{S}_n^+ \cap \mathcal{S}_{M-n+1}^-$ is one-dimensional, then $\mathcal{S}_n$ defines a Lyapunov vector, which grows at the rate $\lambda_n = \lambda_n^+$ as $t \rightarrow +\infty$ and decays at the rate $-\lambda_n = \lambda_{M-n+1}^-$ as $t \rightarrow -\infty$. If $\dim \mathcal{S}_n = d > 1$, then d linearly-independent Lyapunov vectors may be chosen arbitrarily from this space; in this case it is customary to assign d equal Lyapunov exponents to $\mathcal{S}_n$ so that the Lyapunov spectrum contains N (degenerate)

	(k,l)	growth rate
1	$(2,1)$	1.6502
2	$(1,1)$	1.0561
3	$(2,2)$	0.9712
4	$(3,1)$	0.8230
5	$(1,2)$	0.6804
6	$(1,3)$	0.0596

TABLE 3.1: Zonal and meridional wavenumbers k and l, respectively, and growth rates of the six unstable linear disturbances to the zonally uniform state.

exponents.

For a periodic trajectory, the Lyapunov exponents of the trajectory are given by the real parts of the Floquet exponents. Further, if the Floquet exponent λ_i is real, then the i^{th} Lyapunov vector is equal to the i^{th} Floquet vector, and if the Floquet exponents $\{\lambda_i, \lambda_{i+1}\}$ form a complex conjugate pair, then the i^{th} and $(i+1)^{\text{th}}$ Lyapunov vectors lie in the subspace spanned by the real and imaginary parts of the i^{th} Floquet vector. In this sense, Lyapunov vectors generalize Floquet vectors to trajectories of arbitrary time-dependence.

3.3 Nonlinear Wave-Mean Oscillations

3.3.1 Aperiodic Trajectory

For the present study, we considered the most strongly supercritical set of parameters studied by Klein and Pedlosky (1986): $\gamma = 0.20$ and $\Delta = 45$, where

$$\Delta = F - \pi^2 - 4r^2, \tag{3.7a}$$

$$\gamma = r\sqrt{\frac{8}{\Delta}}. \tag{3.7b}$$

This corresponds here to $U_s = 1$, $r \approx 0.4743$, and $F \approx 55.77$. For these parameters, the zonally uniform solution $\psi_1 = \psi_2 = 0$ of (3.1) is unstable to six linear disturbances (Table 3.1). The most rapidly growing linear mode $(2, 1)$ dominates the early evolution of random disturbances to the zonally uniform state, but the $(k, l) = (1, 1)$ Fourier mode eventually dominates the subsequent evolution of the flow. The eventual dominance of a mode with larger scales than the most rapidly growing linear mode is often seen in nonlinear models of the baroclinic instability (Hart, 1981; Pedlosky, 1981).

For large times, the solution approaches a chaotic attractor. The dominance of the $(1, 1)$ mode allows the trajectory to be conveniently represented in the $(A, \partial_t A)$ phase plane, where A is the amplitude of the $(1, 1)$ mode (Fig. 3.1). Numerical estimates based on a long integration ($T \sim 10^4$, using a resolution of 48×40) indicate that the first three Lyapunov exponents, calculated using standard methods (Shimada and Nagashima, 1979; Bennetin et al., 1980), are positive, confirming that the attractor is chaotic (Fig. 3.2). The resulting Kaplan-Yorke dimension (Grassberger and Procaccia, 1983) for this attractor is 7.008 ± 0.004.

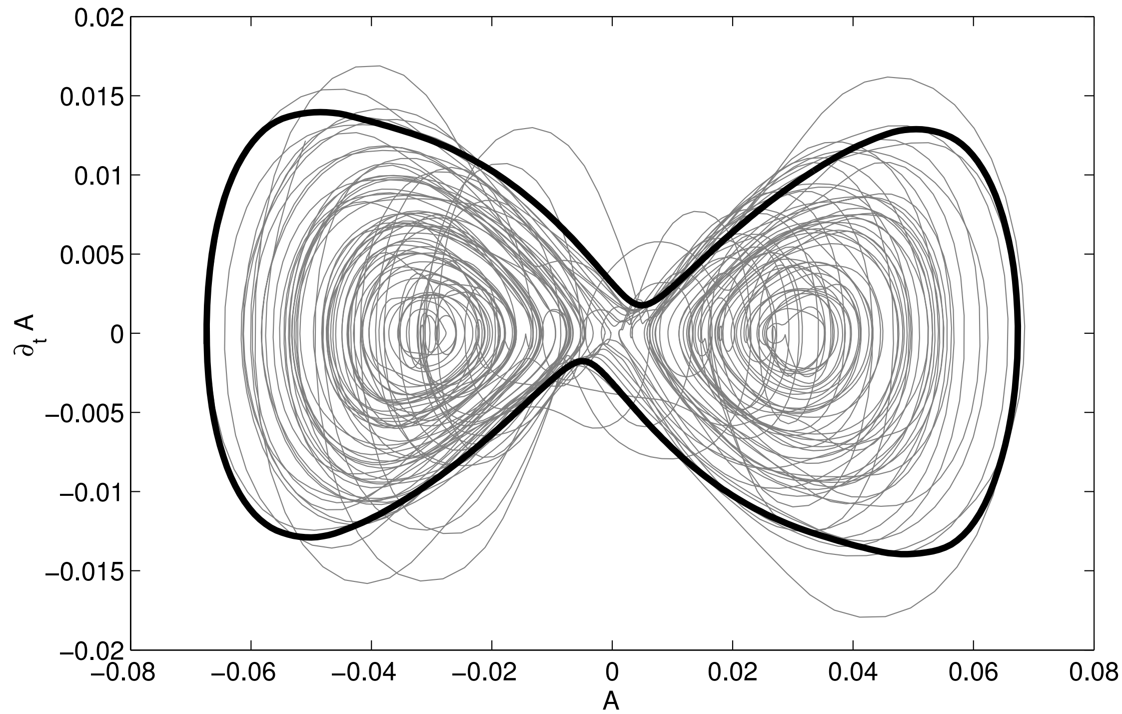

FIGURE 3.1: Chaotic attractor (gray) and the unstable periodic cycle of section 3.3.2 (solid black) plotted in the $(A, \partial_t A)$ phase plane, where A is proportional to the amplitude of the $(1,1)$ Fourier mode. For clarity, only a small portion of the very long ($t \sim 10^4$) chaotic trajectory is shown.

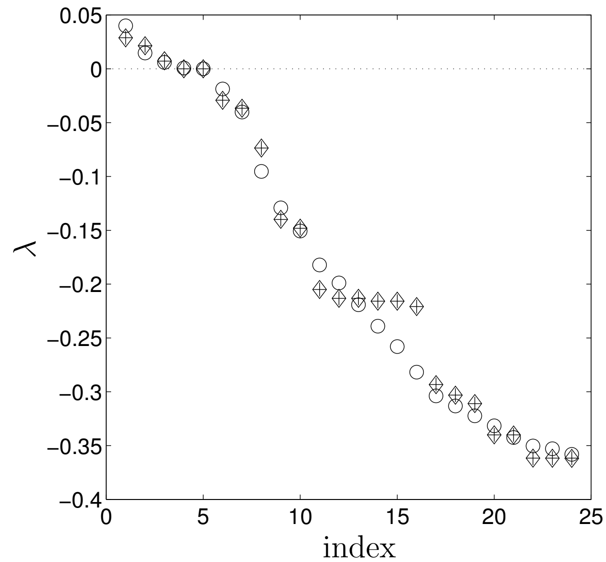

FIGURE 3.2: The first 24 Lyapunov exponents (○'s) of the attractor and the unstable periodic orbit (+'s) shown in figure 3.1, in order of decreasing magnitude. Also shown are the real parts of the first 24 Floquet exponents of the unstable periodic orbit (◇'s). The fifth Lyapunov and Floquet exponents have been set to zero, as explained in section 3.4.3. The errors associated with the Lyapunov exponents are smaller than the symbols used to plot them.

3.3.2 Periodic Basic Cycle

Chaotic attractors, such as that discussed above, are often accompanied by a set of unstable periodic cycles which "fill out" (more precisely, and under specific technical conditions which may or may not hold in the present case, are dense in) the attractor. Certain mean properties of the flow on the chaotic attractor (e.g., Lyapunov exponents, heat flux, etc) may be recovered by constructing suitable averages over unstable periodic cycles (Cvitanović et al., 2005). Often, surprisingly good results are obtained using just a few low-order cycles (Kazantsev, 1998, 2001).

The basic cycle and the methods used to obtain it were described in detail in SW03; a brief recapitulation is provided here for completeness. A low-order unstable periodic cycle associated with the above attractor was found by first searching for near recurrences in a long aperiodic trajectory, and then refining the resulting first-guess initial condition using the Newton-Picard iteration code PDEcont (Lust et al., 1998). The orbit obtained by this code returns to its initial condition with a relative error of less than 10^{-8}. The periodic orbit so obtained forms the basis for the following Floquet analysis and will henceforth be referred to as "the basic cycle." It has a period of $T \approx 38.488$ and, like the attractor, is dominated by the $(1, 1)$ Fourier components and so may be plotted in the same $(A, \partial_t A)$ phase plane as the attractor (Fig. 3.1).

The basic cycle begins as a nearly-zonal flow with a small super-imposed perturbation (Fig. 3.3, top panels). This perturbation grows into a pair of eddies which grow in amplitude as they advect heat (proportional to $\psi_T = \psi_1 - \psi_2$) down-gradient, across the channel. By $t/T = 15/50$, the cross-channel heat flux reduces the background potential vorticity gradient sufficiently to halt and then reverse the growth of the eddies (Fig. 3.3, middle panels). Toward the end of the decay phase, the weakening eddies advect heat up-gradient, extracting energy from the wave and re-establishing the nearly-zonal initial state, now shifted down-channel by one-half the channel length (Fig. 3.3, bottom panels). After passing through a second growth and decay phase the flow returns to its initial state.

As expected, the leading Lyapunov exponents of the cycle are good approximations to the leading Lyapunov vectors of the chaotic attractor (Fig. 3.2), with a relative error in the Lyapunov multipliers e^{λ_j} of less than 10%. Further, the time-averaged heat flux for the basic cycle $\overline{F_T} = 0.1554$, where

$$\overline{F_T} = \frac{F}{2} \lim_{T\to\infty} \frac{1}{T} \int^T \!\! \iint \frac{\partial \psi_2}{\partial x} \psi_1 \, dx \, dy \, dt, \tag{3.8}$$

which approximates that of the chaotic attractor ($\overline{F_T} = 0.1531 \pm 0.0004$) to better

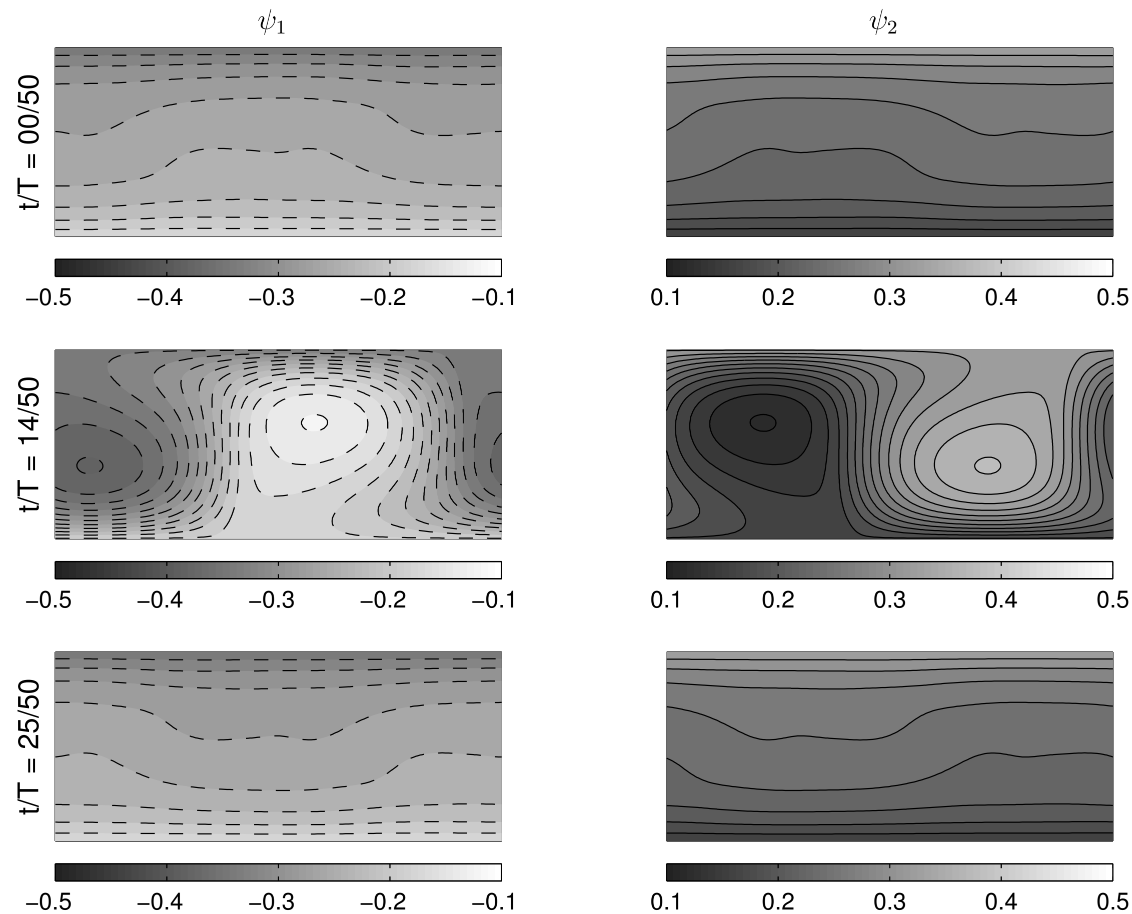

FIGURE 3.3: Contours of the upper- (lhs) and lower-layer (rhs) streamfunction vs x (horizontal axis) and y (vertical axis) during the evolution of the unstable periodic orbit. Negative contours are dashed. For $t/T > 25/50$, the cycle repeats itself shifted half-way down the channel.

than 2%. This suggests that mean quantities may be obtained fairly accurately by averaging over the basic cycle rather than long trajectories on the attractor.

3.4 Time-Dependent Normal Modes

3.4.1 Overview

The time-dependent normal modes for linear disturbances to the basic cycle described in section 3.3.2 are the Floquet vectors (FVs), described in section 3.2.2, which completely characterize the evolution of these disturbances. The spatio-temporal characteristics and asymptotic stability of the FVs thus determine if and how the basic cycle is unstable. In the present case, three of the FVs are unstable and two are neutral, indicating that the basic cycle is, in fact, unstable. The number of unstable and neutral modes found here is independent of resolution and thus is a characteristic of the basic cycle only. The rest of the Floquet spectrum is completed by a large number of decaying modes, the exact number of which depends on resolution. As in Samelson (2001b), the FVs in the present study fall into two physically meaningful classes, described below.

The real parts of the Floquet exponents are equal to the Lyapunov exponents of the basic cycle to within the accuracy of the Lyapunov exponents for all the cases that were checked (Fig. 3.2). That this must necessarily be the case follows from the discussion of the relationship between Lyapunov and Floquet exponents in section 3.2.2. Thus, the numerical equality between these two quantities provides a useful check of the consistency of the numerics.

The majority of the 8928 Floquet vectors of the 72×62 model have exponents whose real parts which lie near, but slightly above, the dissipation rate r, while a small number of vectors have exponents whose real parts which are significantly greater (the "leading" vectors), or less (the "trailing" vectors), than the dissipation rate (Fig. 3.4a). Thus, the bulk of the Floquet vectors are stable and decay at rates near the dissipation rate of the model. The leading vectors either grow or decay weakly while the trailing vectors decay much more rapidly than the dissipation rate.

Floquet vectors with decay rates well separated from the dissipation rate tend to be dominated by disturbances with large scales, while those with decay rates near the dissipation rate have much smaller scales, where the scale is measured by the time-averaged mean wavenumber $\overline{K}$ (Fig. 3.4), defined by

$$(\bar{k}, \bar{l}) = \frac{\sum \pi(|k|, |l|) |{A_{kl}}^n|^2}{\sum |{A_{kl}}^n|^2}, \tag{3.9a}$$

$$\overline{K} = \frac{1}{T} \int_0^T \left[\bar{k}^2 + \bar{l}^2\right]^{1/2} dt, \tag{3.9b}$$

where the sums are taken over all possible values of k, l, and n. These two classes will be referred to as the "wave-dynamical" and "damped-advective" classes, respectively, and will be discussed in sections 3.4.2 and 3.4.4. Those Floquet vectors with large scales have—with few exceptions—purely real Floquet exponents (i.e. they are frequency-locked to the basic cycle). Two Floquet vectors have exponents exactly equal to zero (Fig. 3.4a). These neutral modes, which are a subset of the wave-dynamical class, arise from continuous symmetries of the basic system and are described in section 3.4.3. While the large scale FVs are dominated by a small number of Fourier components, the fine-scale FVs tend to contain significant contributions from many Fourier components. These FVs have complex Floquet exponents with real parts that lie near the dissipation rate and imaginary parts which are distributed approximately uniformly between $\pm\pi/T$. For most of the complex Floquet exponents, $\mathrm{Im}\,[\lambda_j]\, T/2\pi$ is not well approximated (to within 10^{-6})

by any rational number with denominator smaller than 100. The associated Floquet vector structure functions ϕ_n^j thus either have long periods ($\gtrsim 100T$) or may be quasi-periodic.

The transition from wave-dynamical behavior to damped-advective behavior is gradual and there are modes at intermediate wavenumbers ($3\pi \leq \overline{K} \leq 4\pi$) which show characteristics of both classes. Nevertheless, the modes with $\overline{K} < 3\pi$ show characteristics which clearly place them in the wave-dynamical class whereas those with $\overline{K} > 4\pi$ clearly belong to the damped-advective class. These dividing lines are shown in figure 3.4. The intermediate class will not be discussed in a separate section, since these modes do not have any features which clearly distinguish them from the modes in the other classes. There are 62 wave-dynamical, 831 intermediate, and 8035 damped-advective modes at the resolution considered here (72×62).

3.4.2 Wave-Dynamical Modes

The wave-dynamical (WD) Floquet vectors are characterized by large-scale, quasi-stationary wave-patterns, decay rates well separated from the model dissipation rate (Fig. 3.4), and large, transient amplitude fluctuations. These modes depend on the vertical shear of the background flow for their growth and maintenance. The characteristics of the leading ten and trailing nine WD modes are summarized in table 3.2.

The leading twelve WD modes, of which the first three are unstable, are described in Samelson and Wolfe (2003). That study used an approximate monodromy matrix constructed from and projected into the subspace spanned by the gravest 36 zonal and 40 meridional Fourier modes of a 48×40 resolution model to obtain the Floquet vectors, instead of the full monodromy matrix at 72×62 resolution.

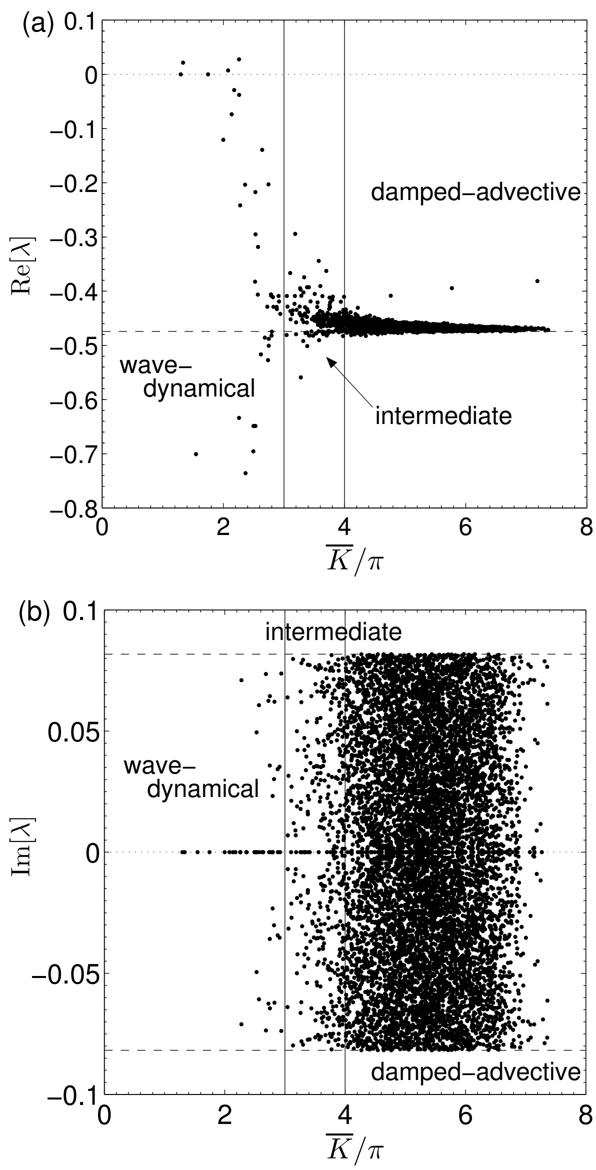

FIGURE 3.4: "Dispersion relations" for Floquet vectors. (a) Real part of the Floquet exponent λ (growth rate) vs. the mean total wavenumber $\overline{K}$ of each mode. The Ekman dissipation rate is given by the dashed line. (b) Imaginary part of the Floquet exponent λ vs. the mean total wavenumber of each mode. The dashed line shows $\mathrm{Im}[\lambda] = \pm\pi/T$. 36 Floquet vectors with $\overline{K} > 8\pi$ are not shown.

index	λ	$\overline{K}/\pi$	(k,l)
1	0.0277	2.2	$(2,1)$
2	0.0215	1.3	$(1,1)$
3	0.0073	2.0	$(2,2)$
4	0.0000	1.7	$(1,1)$
5	0.0000	1.2	$(1,1)$
6	-0.0289	2.1	$(2,1)$
7	-0.0378	2.2	$(1,2)$
8	-0.0736	2.1	$(2,2)$
9	-0.1207	2.0	$(1,1)$
10	-0.1393	2.6	$(1,3)$
$\vdots$	$\vdots$	$\vdots$	$\vdots$
8920	-0.5167	2.6	$(2,1)$
8921	-0.5273	2.7	$(3,1)$
8922	-0.5590	3.3	$(2,2)$
8923	-0.6338	2.3	$(3,1)$
8924	-0.6487	2.4	$(1,2)$
8925	-0.6488	2.4	$(1,2)$
8926	-0.6956	2.5	$(2,1)$
8927	-0.7006	1.5	$(1,1)$
8928	-0.7358	2.4	$(2,1)$

TABLE 3.2: Floquet exponent λ, mean wavenumber $\overline{K}$, and dominate Fourier component (k,l) of the leading ten and trailing nine wave dynamical modes. The temporal and zonal-translation neutral modes (section 3.4.3) are entries four and five, respectively.

The approximate method was only able to obtain the leading twelve WD vectors accurate to within a 10% first-return error. In contrast, the first twelve WD modes obtained by the current method return to their initial conditions to within 10^{-10}. Despite the relative inaccuracy of the method and lower resolution used by SW03, the large scale structures of the leading WD modes obtained using the two methods are remarkably similar. In general, the leading WD modes appear to be robust to changes in resolution or computational method. Modes obtained with one resolution or method can be identified in the spectrum determined using another resolution or method with only modest changes in structure or Floquet exponent.

Since the leading modes obtained in the present study are similar to those described in SW03, only the leading WD mode will be described here as an example (Fig. 3.5, compare to SW03's Fig. 5). This mode is dominated by the second along-channel Fourier component, which is also the most unstable normal mode of the spatially homogeneous system. Comparison with the basic cycle (Fig. 3.3) shows that this disturbance grows and decays in phase with the basic cycle and represents an intensification and down-channel shift of one eddy and a weakening and up-channel shift of the other. The net effect is to narrow and intensify one cross-channel jet while broadening and weakening the other.

The other growing and weakly decaying WD modes show a similar pattern: They are dominated by large scales and grow and decay nearly in phase with the basic cycle (Fig. 3.6). In spatial structure, the third growing mode is similar to the first, as it is dominated by the second along-channel Fourier component (as well as the second cross-channel Fourier component), while the second growing mode has the $(1, 1)$ Fourier component as its primary component and thus has a spatial structure similar to that of the basic cycle (table 3.2).

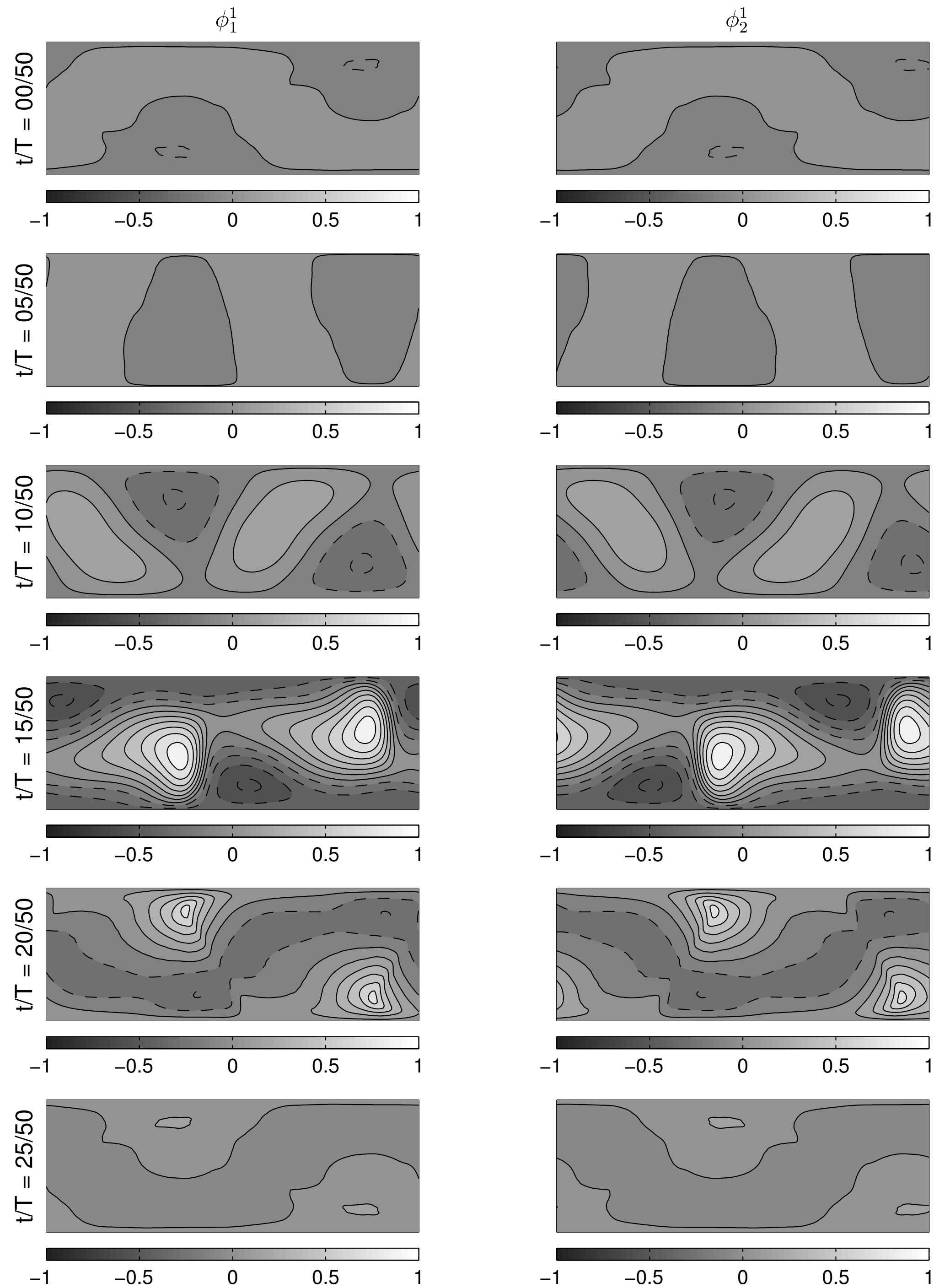

FIGURE 3.5: Contours of the upper- (lhs) and lower-layer (rhs) streamfunction vs x (horizontal axis) and y (vertical axis) during the evolution of the Floquet structure function ϕ^1 for which $\lambda \approx 0.0277$. Negative contours are dashed.

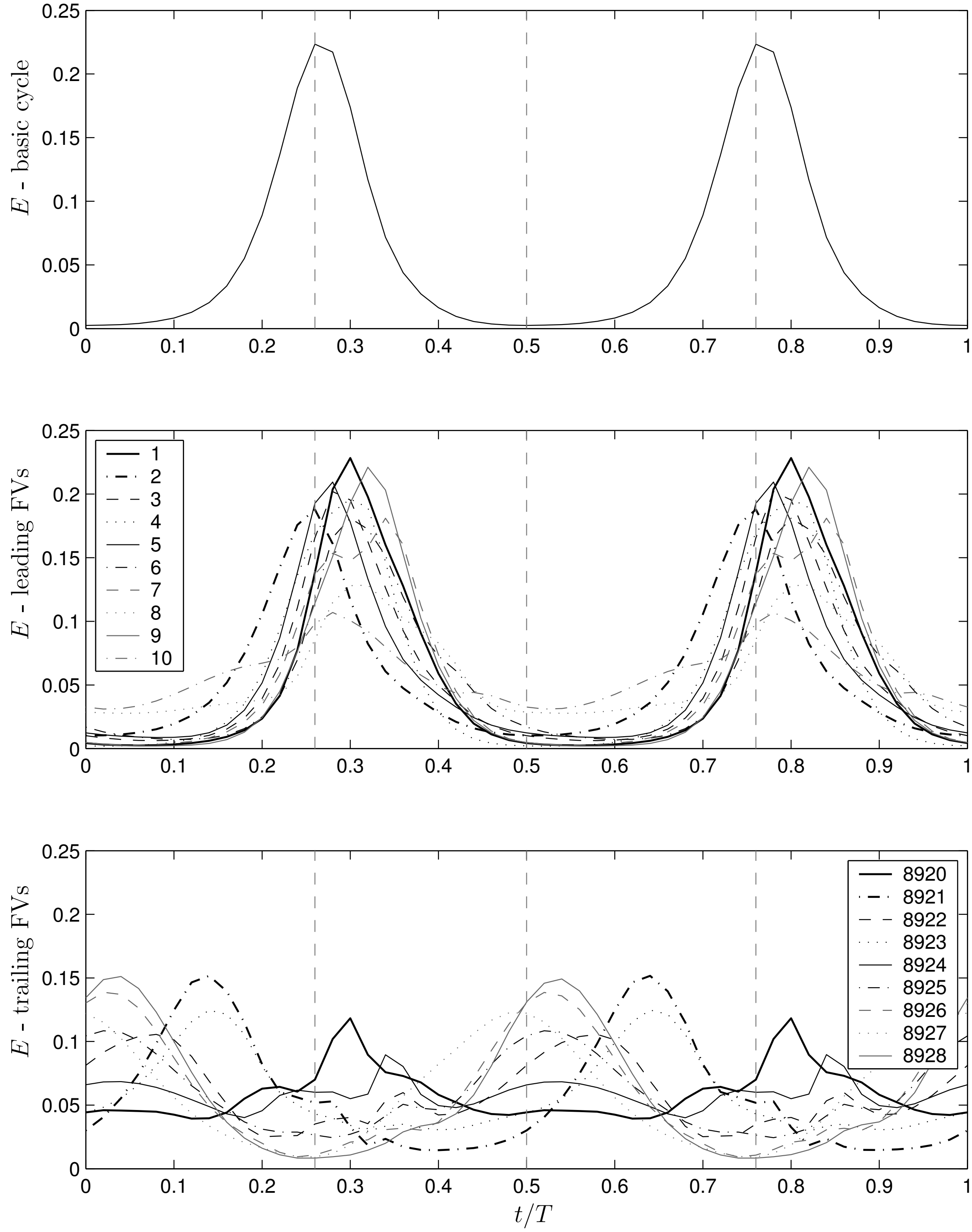

FIGURE 3.6: Total wave energy E as a function of normalized time t/T. Top panel: basic cycle. Middle panel: ten most rapidly growing Floquet vectors. Bottom panel: nine most rapidly decaying Floquet vectors. The legends give the FV index of each mode.

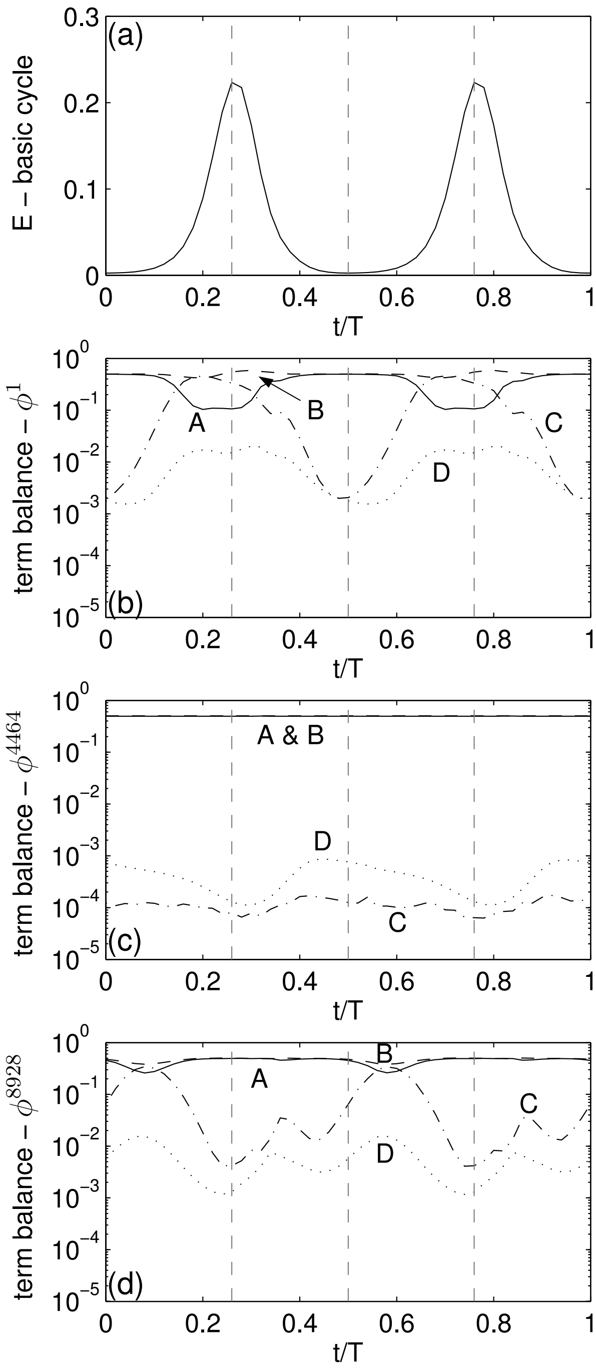

FIGURE 3.7: (a) Wave energy of the deviation of the basic cycle from its zonal mean. (b–d) Relative magnitudes of the terms A (solid), B (dashed), C (dash-dot), and D (dotted) in eq. (3.3) for FVs (b) ϕ^1, (c) ϕ^{4464}, and (d) ϕ^{8928}. In (c), the terms A and B have the same magnitude and are plotted on top of each other. The vertical dashed lines pick out the cycle extrema.

While the leading WD mode structure function ϕ^1 is growing during the basic cycle growth phase, the perturbation dynamics are dominated by the exchange of PV with the mean flow (Fig. 3.7; terms B and C in (3.3)). During this time, the perturbation PV flux is strongly down the background flow PV gradient (Fig. 3.8b), as measured by the normalized perturbation enstrophy production

$$\boldsymbol{u}'q' \star \nabla q \equiv \frac{\iint \boldsymbol{u}'q' \cdot \nabla q \, dxdy}{\left[\iint \|\boldsymbol{u}'q'\| \, dxdy \iint \|\nabla q\| \, dxdy\right]^{1/2}}, \tag{3.10}$$

where $\boldsymbol{u}'$ and q' are computed from the Floquet structure functions. Between growth phases, the leading Floquet vectors are advected by the background flow and eroded by Ekman dissipation (Fig. 3.7b). During this time, the perturbation PV flux is only weakly down-gradient. The leading FVs do not appear to undergo an inviscid decay phase like that seen in the basic cycle. The growth-phase counter-gradient PV flux is largest in the growing FVs (ϕ^1 through ϕ^3), smaller in the weakly decaying FVs, and insignificant for $\phi^n, n \geq 18$. The behavior of the perturbation heat flux (not shown) is similar.

In addition to the growing and weakly decaying modes, there is a complementary set of inviscidly damped WD modes (Fig. 3.9). These modes have spatial scales similar to the leading Floquet vectors, but decay at rates much greater than the frictional dissipation rate. Samelson (2001b) found a similar inviscidly damped mode in a weakly nonlinear model of the baroclinic instability. SW03 could not compute these modes because of limitations in their computational method.

The spatial scales of three most rapidly decaying Floquet vectors follow a pattern similar to the leading three Floquet vectors, with the structure functions ϕ^{8926} and ϕ^{8928} dominated by the second along-channel Fourier component and ϕ^{8927} dominated by the first along-channel Fourier component (Table 3.2). These trailing

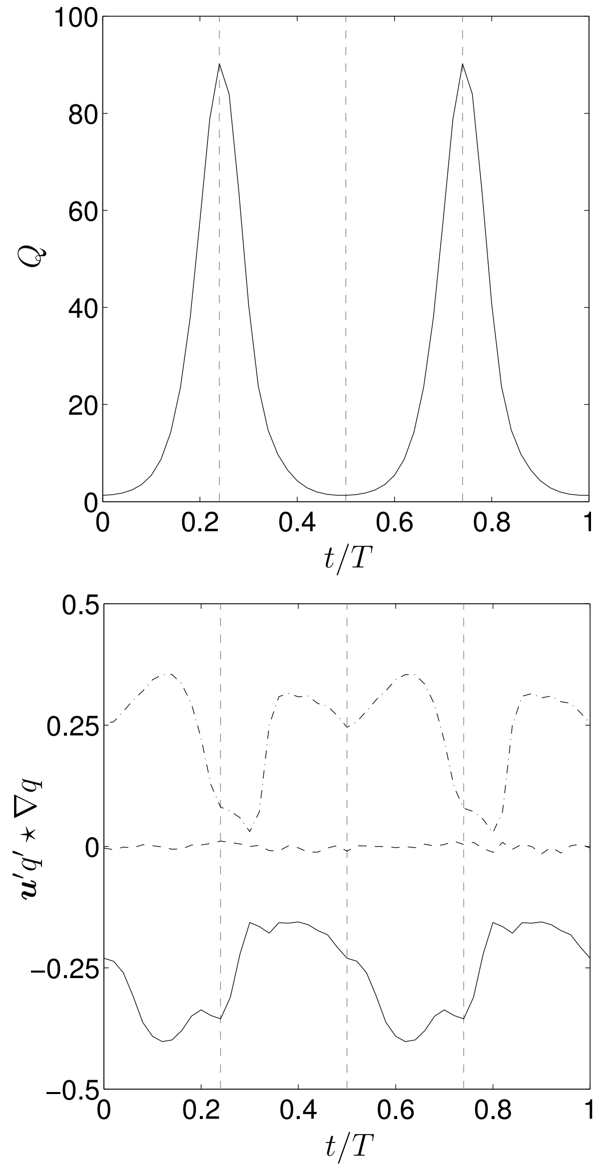

FIGURE 3.8: Upper panel: Time evolution of basic cycle potential enstrophy Q. Lower panel: Correlation of perturbation PV flux with the background PV gradient ($\boldsymbol{u}'q' \star \nabla q$) for wave-dynamical modes ϕ^1 (solid), ϕ^{8928} (dash-dot), and damped-advective mode ϕ^{4464} (dotted) as a function of time. The vertical dashed lines pick out the cycle extrema.

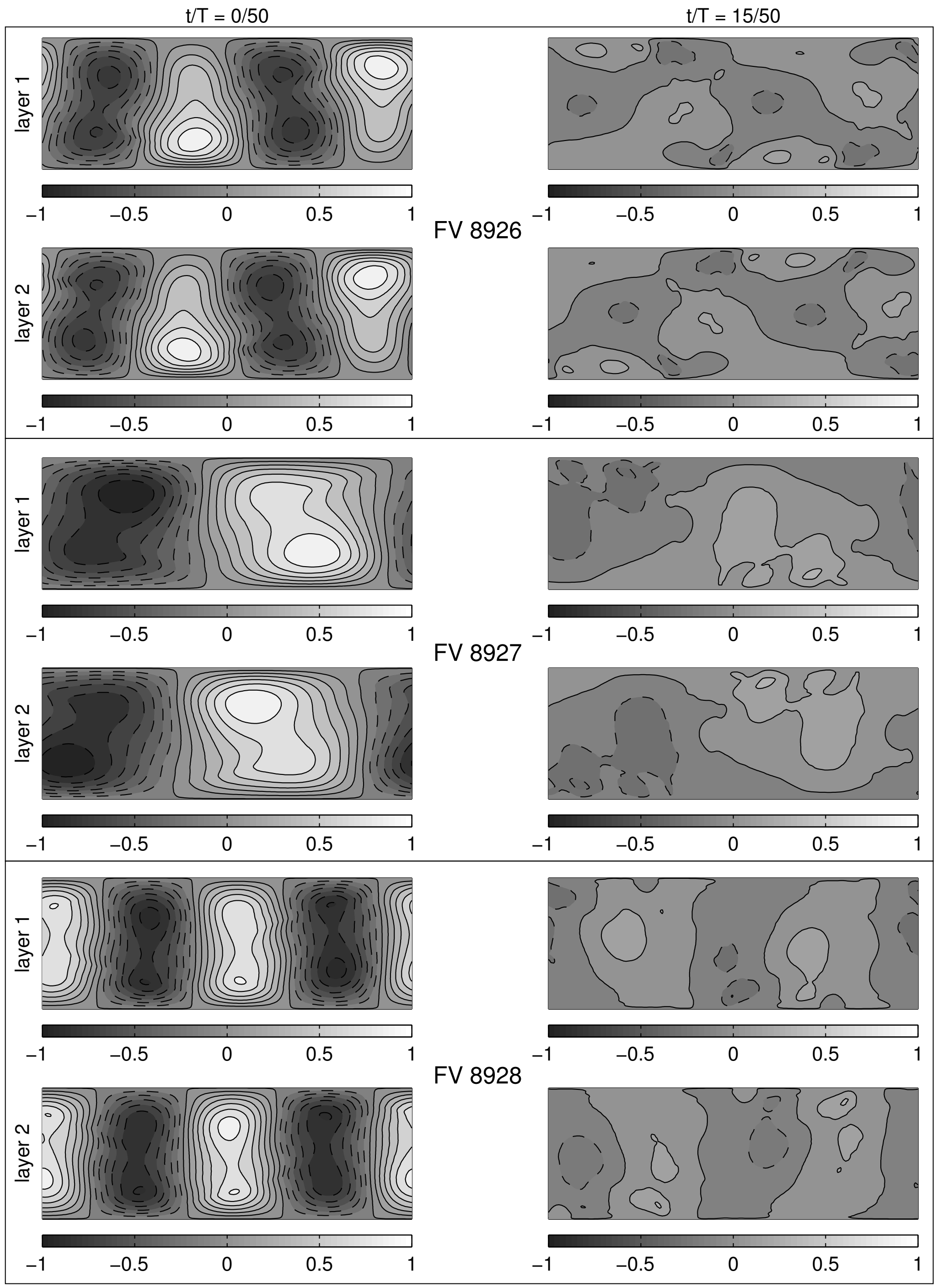

FIGURE 3.9: Contours of the upper- and lower-layer streamfunction vs x (horizontal axis) and y (vertical axis) of the structure functions of the three most rapidly damped FVs at the beginning of the cycle (left panels) and at $t/T = 15/50$ (right panels). Negative contours are dashed.

modes are nearly completely out of phase with the basic flow (Fig 3.6) and obtain their maximum amplitude while the basic cycle is most zonally homogeneous. Thus, the leading modes grow while the basic cycle is growing, and the trailing modes grow while the basic cycle is either decaying or at very low amplitude. For $t/T \geq 25/50$, ϕ^{8926} and ϕ^{8928} repeat their growth/decay cycle shifted halfway down-channel; ϕ^{8927} repeats its growth/decay cycle shifted halfway down-channel with the opposite sign. These disturbances have a slight eastward phase shift with height, which is unfavorable for baroclinic growth, and decay rapidly as the basic cycle enters its growth phase. Note that the eastward phase shift of the modes shown in fig. 3.9 is not as dramatic as the westward phase shift of the leading WD mode shown in fig. 3.5. This is in fact consistent with the classical Phillips model with dissipation: Growing modes must have a significant westward phase shift merely to maintain themselves against dissipation. A small eastward phase shift can result in a large decay rate because the inviscid decay created by the unfavorable phase shift is added to the already large viscous decay rate of the mode. The apparent north/south phase shift seen in fig. 3.9 is likely due to the north/south asymmetry of the basic cycle.

In contrast to the leading FVs, the peak in PV exchange (terms B and C in (3.3)) for the trailing FVs occurs before the growth phase of the basic cycle, while the basic cycle is most zonally uniform (Fig. 3.7d shows ϕ^{8928}; the other trailing FVs are similar), and results in strong up-gradient flux of PV (Fig. 3.8). The up-gradient PV flux is at a minimum when the basic cycle reaches its maximum amplitude, then rebounds to moderate levels during the decay phase of the basic cycle. The trailing modes are thus inviscidly damped throughout most of the basic cycle.

In summary, the leading WD modes grow by advecting PV and heat down-gradient while the basic cycle is growing and are able to continue to do so even when the background flow is highly zonally inhomogeneous (Figs. 3.6 & 3.8). The down-gradient PV and heat flux becomes weak during the decay phase of the basic cycle, during which time the disturbances amplified during the growth phase are advected and distorted by the background flow. The trailing FVs reach their largest amplitude when the background flow is most zonal and advect PV and heat up-gradient, leading to rapid inviscid decay (Figs. 3.6 & 3.8). Dissipation is never a leading order effect (Fig. 3.7), but acts continuously and is sufficient to reduce the growth rates of the three leading FVs and stabilize the others. Note, however, that, since the basic flow has neither temporal nor spatial symmetry, a physically consistent quadratic disturbance quantity cannot be defined, and the rigor of this interpretation of the wave-mean interaction is necessarily limited.

3.4.3 Neutral Modes

Two of the wave-dynamical modes are neutral, with Floquet exponent exactly equal to zero (Table 3.2). These modes exist as a consequence of the two continuous symmetries—time and zonal translation—of the nonlinear evolution equation (3.1). The temporal neutral mode has larger scales than the zonal-translation neutral mode. The spatio-temporal structure of these modes is described in SW03, where the temporal and zonal-translation modes are referred to as Φ^4 and Φ^5, respectively. SW03, however, did not identify Φ^5 as a neutral mode.

To see how these neutral modes arise from continuous symmetries of the nonlinear evolution equation, represent a general nonlinear equation for the evolution of the state vector ψ by

$$\psi_t = \mathcal{N}(\psi), \tag{3.11}$$

where $\mathcal{N}$ is the nonlinear evolution operator and ψ is either steady, time-periodic, or uniformly bounded in time t and may depend on space $\boldsymbol{x}$. Linear disturbances ψ' to ψ satisfy

$$\psi'_t = \mathcal{L}_\psi \psi', \tag{3.12}$$

where $\mathcal{L}_\psi$ is the linearization of $\mathcal{N}$ about ψ. Particular interest attaches to 'normal-mode type' solutions to eq. (3.12), i.e., solutions of the form

$$\psi'(\boldsymbol{x}, t) = \phi(\boldsymbol{x}, t) e^{\lambda t}, \tag{3.13}$$

where the structure function ϕ is steady, time-periodic, or uniformly bounded in time depending on the time-dependence of ψ. The evolution of ϕ is governed by the (linear) equation

$$\phi_t + \lambda \phi = \mathcal{L}_\psi \phi. \tag{3.14}$$

Suppose now that $\mathcal{N}$ is invariant to changes in the continuous variable ξ, which may be, for example, x or t. Then, if $\psi(\xi)$ is a solution to (3.11), so also is $\psi(\xi + \delta\xi)$ for any value of $\delta\xi$. (The dependence of ψ on variables other than ξ has been suppressed.) If $\delta\xi$ is small, then

$$\psi(\xi + \delta\xi) = \psi(\xi) + \delta\xi \psi_\xi(\xi) + \mathcal{O}(|\delta\xi|^2). \tag{3.15}$$

Substitution into (3.11) gives

$$\psi_t + \delta\xi \psi_{\xi t} = \mathcal{N}\left(\psi + \delta\xi \psi_\xi\right) + \mathcal{O}(|\delta\xi|^2) \tag{3.16a}$$

$$= \mathcal{N}(\psi) + \delta\xi \mathcal{L}_\psi \psi_\xi + \mathcal{O}(|\delta\xi|^2), \tag{3.16b}$$

which simplifies to

$$\left(\psi_\xi\right)_t = \mathcal{L}_\psi \left(\psi_\xi\right) \tag{3.17}$$

after the limit $\delta\xi \to 0$ is taken. Note that ψ_ξ is steady, time-periodic, or uniformly bounded in time if ψ is.

Comparison of eq. (3.17) to eq. (3.14) shows that $\phi = \psi_\xi$ is a solution to eq. (3.14) with $\lambda = 0$. Thus, if $\mathcal{N}$ is invariant to changes in ξ, ψ_ξ can be identified as the structure function of a neutral normal mode. If the nonlinear solution ψ is time-periodic, then so is the structure function ψ_ξ and we can thus identify ψ_ξ as a neutral Floquet vector. Since (3.1) is invariant to translations in time t and the zonal coordinate x, neutral modes will exist that are proportional to temporal and along-channel derivatives of the basic cycle. The former corresponds to an infinitesimal shift in time of the basic wave-mean oscillation while the later corresponds to an infinitesimal along-channel shift in the position of the oscillation.

In practice, neither of the numerically determined neutral modes have Floquet exponents exactly equal to zero due to numerical errors. For the temporal neutral mode, small departures of the basic cycle from exact periodicity break the time translation invariance of the basic cycle leading to small departures of the mode from neutrality. The departures from exact periodicity are small ($< 10^{-6}$) so the magnitude of the corresponding exponent is less than 10^{-8}.

The precision with which the zonal-translation neutral mode is determined is limited both by the ability of the space-differencing scheme to resolve the fourth derivative of the basic cycle (three from the gradient of the potential vorticity and one from the neutral mode itself) and by the fact that imposing a numerical grid transforms the continuous zonal symmetry into a discrete symmetry. The basic cycle contains enough power at high wavenumbers and the numerical grid is course enough even at the relatively high resolution of 72×62 that the magnitude of the numerically determined Floquet exponent is greater than 10^{-3}. Numerical experiments which computed a subset of the Floquet vectors show that, when the resolution is increased to 128×64, Φ^5 converges to neutrality to within 10^{-4} (almost 100 times smaller than

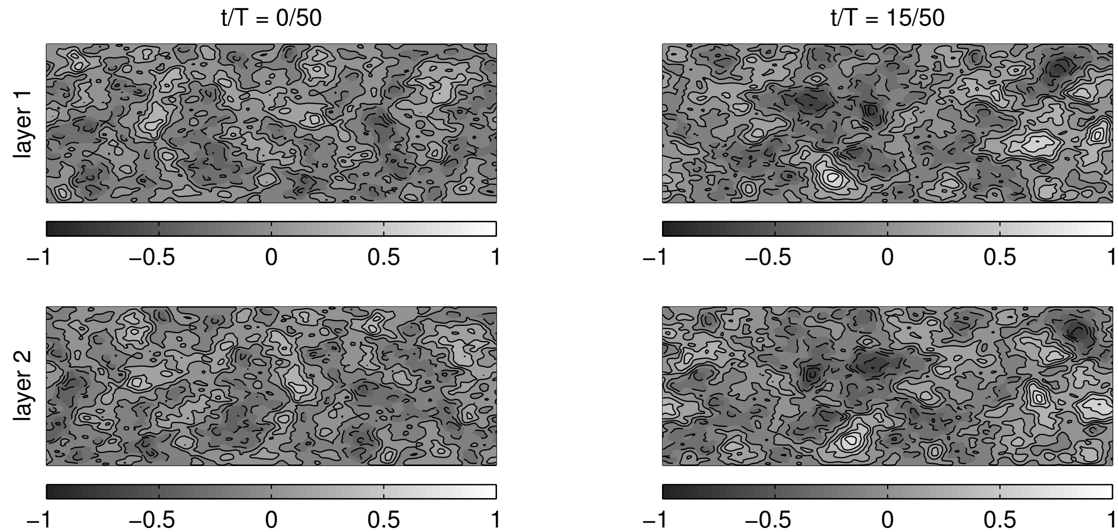

FIGURE 3.10: Contours of the upper- (lhs) and lower-layer (rhs) streamfunction vs x (horizontal axis) and y (vertical axis) during the evolution of the Floquet structure function ϕ^{4464} for which $\lambda \approx -0.9865r - i0.3336\pi/T$. Negative contours are dashed.

the next largest Floquet exponent). For consistency with the rest of the calculations, the solution of Φ^5 has been held at 72×62, but the numerically determined zonal-translation neutral vector has been replaced by the along-channel derivative of the basic cycle, and the corresponding exponent has been set to zero.

3.4.4 Damped-Advective Modes

The vast majority ($\approx 95\%$ at 72×62 resolution) of the Floquet spectrum is made up of vectors with small, irregular spatial features that are advected by the mean flow and decay nearly at the dissipation rate r; they are thus called 'damped-advective' (DA) modes (Fig. 3.4). Samelson (2001b) found a related set of damped modes in the weakly nonlinear problem. SW03 did not find a set of DA in the fully nonlinear problem due to limitations of their numerical method.

The evolution of the structure function ϕ^{4464}, which is representative of this class, is characterized by the creation, decay, and advection of incoherent fine-scale eddies (Fig. 3.10). These modes do not appear to have any coherent phase shift with height. The perturbation PV flux of this mode is uncorrelated with the background PV gradient (Fig. 3.8); the perturbation heat flux (not shown) is similarly uncorrelated with the background temperature gradient. This mode is thus unable to effectively exchange vorticity or energy with the background flow and can only decay by Ekman dissipation. Consistent with this fact, analysis of the term balance for this mode shows that the dynamics reduces to passive advection of the disturbance PV by the background flow (Fig. 3.7c). Although the dissipation term (D) remains small throughout the evolution of this mode, it remains larger than the only term which can affect growth (term C). The dominance of terms A and B reflects the leading order passive advective dynamics of the mode. The net effect of the relatively small, continuous viscous decay is a large reduction in the amplitude of the mode over the basic cycle.

The other DA modes are similar: they have complex exponents, little or no phase shift with height or correlation between the perturbation PV (heat) fluxes with the background PV (temperature) gradient, and term balances dominated by passive advection. For a given mode amplitude, the dissipation term for the DA modes is generally larger than for the WD modes, because the DA modes have smaller scales. A few DA modes with very fine spatial scales (off the right-hand side of figure 3.4) decay significantly slower than the dissipation rate ($\mathrm{Re}\,[\lambda] \sim -0.4$) due to the fact that the Runge-Kutta time-stepping algorithm anomalously amplifies high wavenumber Fourier modes (e.g., Durran, 1998, chap. 2). In a subset of numerical solutions using the Adams-Bashforth scheme, which does not amplify these Fourier modes, these vectors had the same spatial structures as those found with the Runge-

Kutta scheme, but decayed with rates near r like the other DA modes.

In addition to having small spatial scales (i.e., large values of $\overline{K}$), the DA modes typically have broad wavenumber spectra (Fig. 3.11). For example, the potential enstrophy wavenumber spectrum of ϕ^{4464} is essentially flat (Fig 3.11b), as is the case for almost all of the DA modes, as evidenced by the fact that the energy and potential enstrophy wavenumber spectra averaged over all DA modes with $4\pi < \overline{K} < 8\pi$ (8291 modes) are almost identical to the spectra of ϕ^{4464} (Fig 3.11). This result is not specific to the choice of ϕ^{4464}, as nearly all of the DA modes are statistically similar to each other. Note that, if the enstrophy wavenumber spectra remain flat in the continuum limit, the integral of the spectra (the total enstrophy) will be unbounded.

Many of the features of the DA modes are similar to those of the continuum modes which are frequently encountered in the study of scalar advection and the stability of shear flow (e.g., Drazin and Reid, 2004, chap. 4). In models with continuous shear—such as the model discussed here—the spectrum of discrete normal modes is generally not complete and must be supplemented by a set of continuum normal modes in order to describe the evolution of arbitrary initial disturbances (Orr, 1907). Such continuum modes are "weak" solutions to the governing equations because, while their streamfunctions fields are continuous, their vorticity fields contain singular structures and the associated enstrophy is unbounded. From one point of view, the continuum modes appear as a consequence of applying the normal-mode formalism to a system which may be alternatively formulated as an advective solution to an initial value problem (Orr, 1907; Case, 1960). The two formalisms are equivalent for steady parallel shear flow, but the physical interpretation of the advective solution is intuitively more appealing.

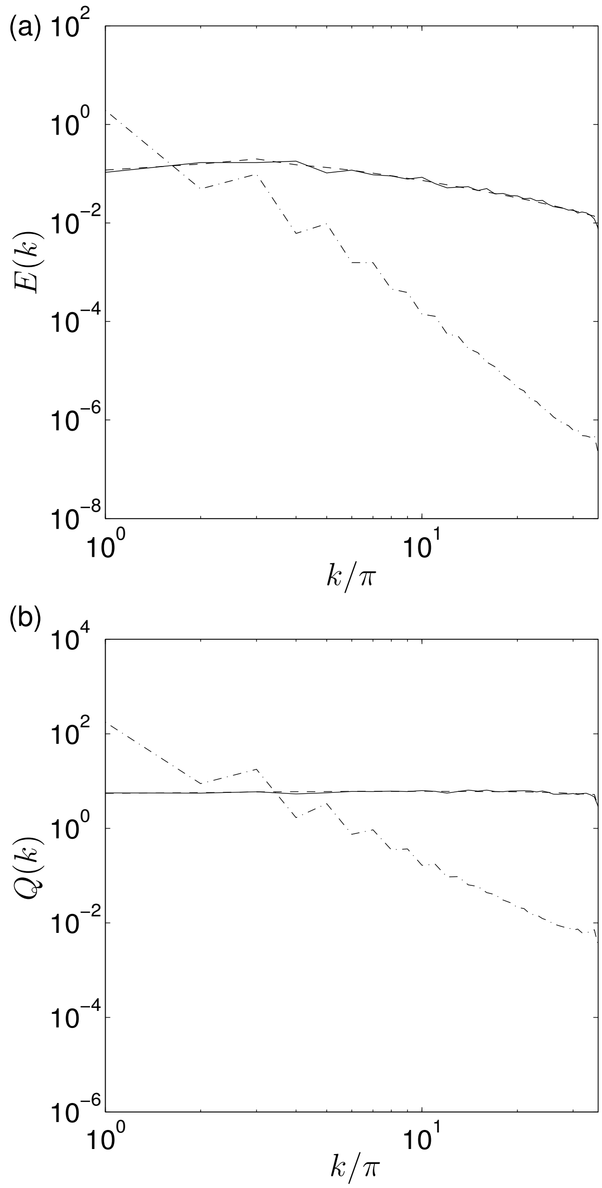

FIGURE 3.11: Zonal wavenumber spectra of (a) wave energy $E(k)$ and (b) potential enstrophy $Q(k)$ for the DA mode ϕ^{4464} (solid) and averaged over all DA modes with $4\pi < \overline{K} < 8\pi$ (dashed). The wavenumber spectra of the basic cycle (dash-dot) are shown for reference.

When represented by a finite dimensional numerical model, the continuous spectrum is artificially truncated and rendered discrete. The spatial structures of the resulting numerically determined continuum modes are generally sensitive to the exact nature of the numerical model, but the wavenumber spectra may often contain significant contributions at high wavenumber; in particular, if the PV wavenumber spectrum is nearly flat, it may indicate that the numerical model is attempting to resolve singular structures in the PV. Thus, it is tempting to view the DA modes obtained here as representing generalizations of the classical singular modes to time-dependent background flows. The DA modes appear to have unbounded enstrophies in the continuum limit and, consistent with the expected sensitivity of continuum modes to the details of the numerical model, they are not robust to changes in resolution. Floquet spectra calculated at slightly different resolutions produce sets of DA modes which are statistically similar, but there is no direct correspondence between the individual vectors produced at different resolutions (see section 3.5). However, such a view is necessarily speculative, since it is based in part on the lack of convergence of the numerical results to individually well-defined modes, and since it is not known whether the time-dependent basic flow should possess an analogous set of singular continuum modes. Consequently, the DA modes are best viewed as representing, as a class, a generalized solution to the damped-advective initial value problem. This point is discussed further in section 3.6.

3.5 Convergence of the Numerical Method

The continuous limit of the basic cycle possesses, in principle, an infinite set of Floquet vectors. It would be of interest to determine, in the continuous limit, the number of FVs in each class and whether either class contains a continuum of modes. There are few theoretical results which would constrain the number of discrete normal modes in the continuous limit, so estimates of this number must be obtained as part of the numerical solution.

Full Floquet spectra were obtained for resolutions of 24×22, 36×32, 48×40, 54×45, and 72×62. As resolution increases, the corresponding distributions of λ and $\overline{K}_\phi$ rapidly approach limiting distributions dominated by the damped-advective modes (Figs 3.12, 3.13). The spike at $\mathrm{Im}\,[\lambda] = 0$ (Fig. 3.12b) and its disappearance as the resolution is increased indicates that the number of wave-dynamical modes with $\mathrm{Im}\,[\lambda] = 0$, N_{Re}, increases much more slowly than the total number of Floquet vectors. The rate with which N_{Re} increases becomes slower at high resolutions (Fig 3.13). This suggests that N_{Re} may be finite in the continuous limit.

The distribution of potential-vorticity-mean wavenumber $\overline{K}_q$ (Fig. 3.12d) does not converge to a limiting distribution, but takes the form of a series of spikes at progressively higher wavenumber. The positions of the maxima are consistent with a white enstrophy spectra for the damped-advective modes (see Fig. 3.11), for which the expected value of the mean wavenumber is $\overline{K}_q = K_{\max}/2$, where $K_{\max}$ is the maximum resolved wavenumber (Fig. 3.12d).

The total number of WD modes (i.e., those with $\overline{K} < 3\pi$), N_{WD} fluctuates at low resolutions, but appears to have reached a limiting value $N_{\mathrm{WD}} = 62$ at the highest two resolutions considered (Fig. 3.13). It is not clear whether this represents the true number of WD modes in the continuum limit or whether more WD modes will appear at higher resolution. Nevertheless, this result strongly suggests that the number of WD modes is bounded in the limit of an infinitely finely resolved model. In contrast to N_{WD} and N_{Re}, the number of intermediate and DA modes increases

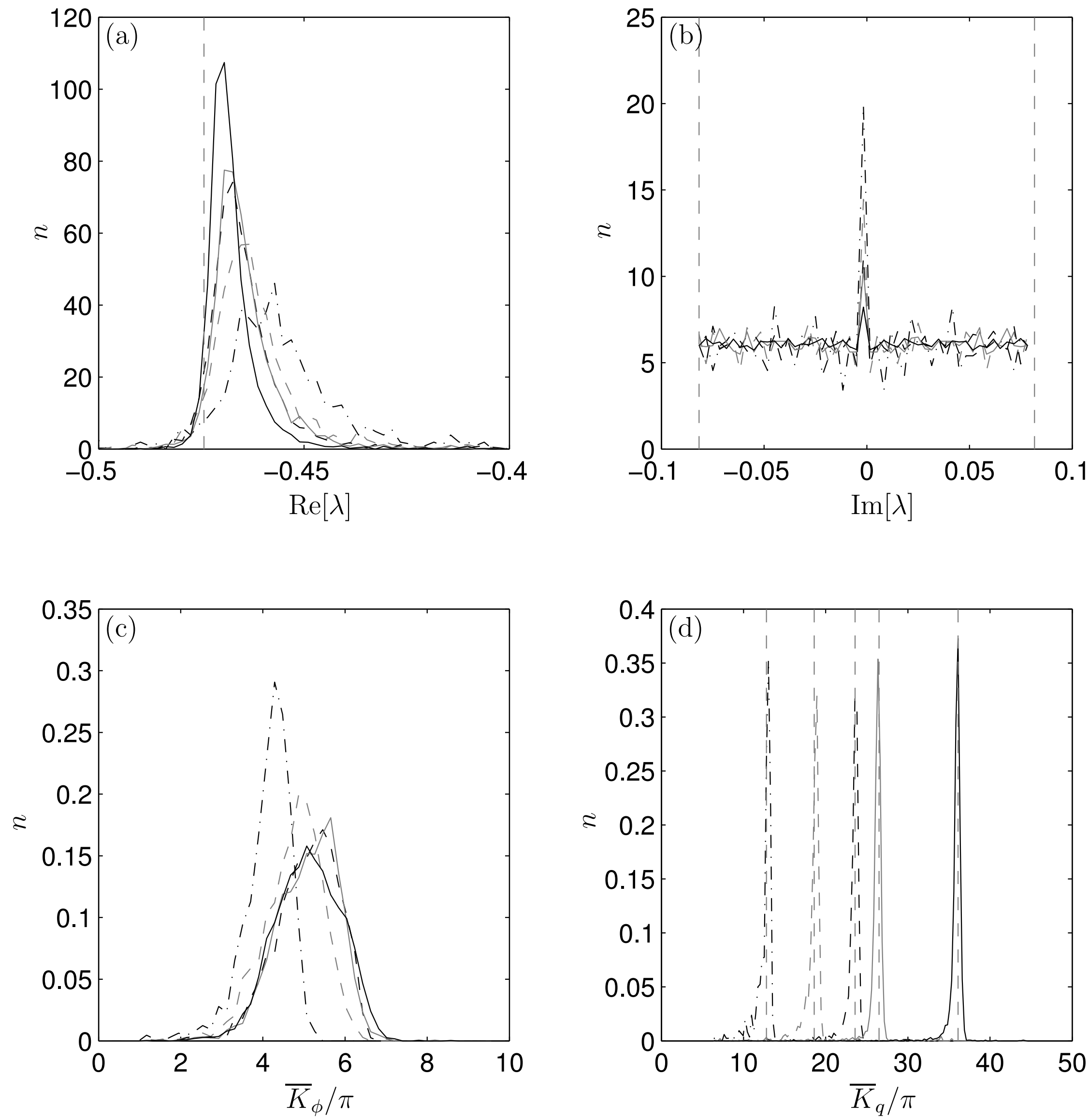

FIGURE 3.12: Normalized histograms of (a) Floquet vector growth rate Re[λ], (b) imaginary part of the Floquet vector Im[λ], (c) mean total wavenumber $\overline{K}_\phi$ of the streamfunction ϕ, and (d) mean total wavenumber $\overline{K}_q$ of the potential vorticity q. The line style gives the model resolution: 24×22 (dash-dot black), 36×32 (dashed gray), 48×40 (dashed black), 54×45 (solid gray), and 72×62 (solid black). In panel (a), the dashed vertical line gives the frictional dissipation rate $-r$. In panel (b), the dashed vertical lines are at $\pm\pi/T$. In panel (d), the dashed vertical lines are at $K_{\max}/2$. The PDFs have negligible amplitude outside the ranges shown. 50 bins where used in all cases.

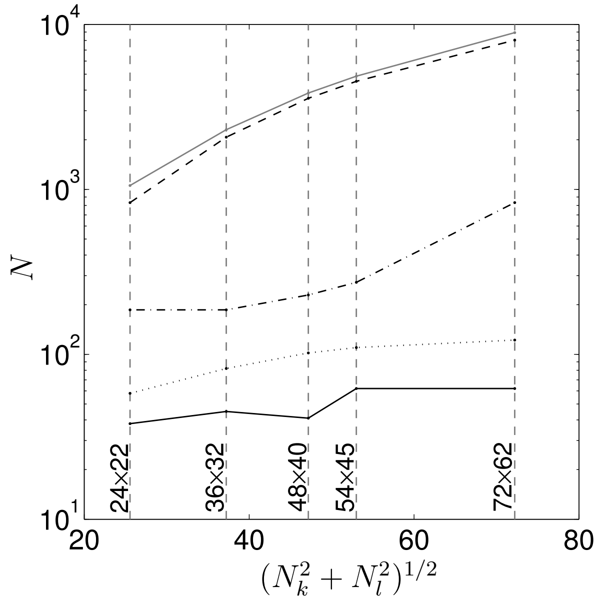

FIGURE 3.13: Number of wave-dynamical N_{WD} (solid), intermediate N_{In} (dash-dot), and damped-advective N_{DA} (dashed) modes and the total number of modes $2N_xN_y$ (gray) as a function of model resolution. Also shown is the number of modes with real Floquet exponents N_{Re} (dotted).

rapidly as resolution increases. Whether the DA modes eventually merge into a continuum is an open question.

3.6 Discussion

We have obtained a complete set of Floquet vectors for a baroclinic wave-mean oscillation at high resolution. The Floquet vectors fall into two classes that have direct physical interpretations, the wave-dynamical (WD) and damped-advective (DA) modes.

The WD class (which includes the two neutral modes) consists of two groups, one which contains vectors which grow or weakly decay (the leading vectors) and one which contains vectors which rapidly decay (the trailing vectors). The two groups are distinguished primarily by their phase-shift with height and their growth-phase relationship with the basic cycle: the leading vectors have a westward phase shift and grow while the basic cycle is growing while the trailing vectors are tilted slightly eastward and decay during the basic cycle growth phase. The leading vectors are important for determining the asymptotic stability of the oscillation and, indeed, the existence of three WD modes with $\mathrm{Re}\,[\lambda] > 0$ confirms that the basic cycle is unstable.

The DA class has many more members than the wave-dynamical class, but they are all similar in spatial structure and decay rate. Due to their dominance of the Floquet spectrum, any initial disturbance which contains small scale features will excite a large number of DA modes. These modes will then describe most of the variance at small scales before the asymptotic growth of the leading wave-dynamical modes begins to dominate. This occurs very quickly since the e-folding decay time of each DA mode is $\sim 1/r \approx 0.05T$. The dynamics of the damped-advective modes are, to first order, advection of the PV field by the background flow. These modes share many characteristics with the singular modes of parallel shear flow, including flat PV wavenumber spectra and sensitivity to the details of the model configuration.

The existence of these two classes of normal-mode solutions to the numerical Floquet eigenvalue problem indicates a dynamical splitting of the linear disturbance problem for this time- and space-dependent baroclinic flow. On the one hand, a small set of discrete, large-scale, growing or decaying normal-mode structures is easily identified. These modes have immediate physical interpretations and are analogous to the familiar normal modes of steady parallel flow. They appear naturally as intrinsic time-dependent eigenmodes of the linear disturbance flow. In contrast, the individual members of the large set of damped-advective modes should be interpreted to represent, in sum, the frictionally damped advection of small-scale potential vorticity anomalies by the basic flow. From a physical point of view, the solution of this portion of the linear-disturbance initial value problem might be most appropriately conceptualized, and perhaps even quantitatively computed, by using the method of characteristics to follow initial disturbances along Lagrangian fluid trajectories. This would be a natural extension of Orr's (1907) characteristic-based solution for advective motions in parallel shear flow, which provides an intuitive alternative to the singular neutral mode description that arises from the corresponding normal-mode eigenvalue problem (Case, 1960).

As discussed in SW03, the unstable wave-dynamical modes have intriguing similarities to the unstable modes of the spatially homogeneous flow $\psi_n = 0$. In particular, the dominant Fourier component of these modes corresponds, respectively, to the first three normal modes of the spatially homogeneous flow (compare tables 3.1 & 3.2). Both occur in the order $(2,1)$, $(1,1)$, $(2,2)$ although the leading WD modes also contain strong contributions from other Fourier components. The correspondence of the three most rapidly decaying wave-dynamical modes with the three most stable modes of the homogeneous flow (which occur in the reverse order of the unstable modes) is even stronger, since the trailing WD modes have their largest amplitude when the background flow is most zonally uniform. The growth (resp. decay) rates of the leading (resp. trailing) WD modes are greatly reduced from those of the homogeneous, steady flow. This is evidently primarily due to a reduction in the time-mean vertical shear from its undisturbed value of $U_s = 1$ and the introduction of a time-mean barotropic shear due to modifications to the mean flow by the basic cycle. The former effect reduces the potential energy available for growing disturbances, while the latter reduces the ability of disturbances to maintain the proper phase shift necessary to extract energy (i.e., the 'barotropic governor' effect (James, 1987)).

It is interesting to note that the spatially homogeneous state $\psi_n = 0$ appears to be a better predictor of the spatial structure and ordering of the leading WD modes than the time- and zonal-mean of the basic cycle. The latter state is unstable to a single linear disturbance (not shown) which is dominated by the $(1, 1)$ Fourier component and closely resembles WD mode ϕ^2. The growth rate of this mode is 0.0763, only slightly greater than the growth rate of ϕ^2 (0.0215). Disturbances to the time- and zonal-mean flow which resemble WD modes ϕ^1 and ϕ^3 are both stable, with the analog of ϕ^1 more stable than that of ϕ^3. The analogs to the trailing WD modes are also disordered, with the first, second, and third most stable disturbances to the time- and zonal-mean flow corresponding, respectively, to the second, third, and first mode stable WD modes. While an analysis of the time-mean of a non-stationary flow often does not provide a good estimate of the stability characteristics of the non-stationary flow, it is perhaps surprising that this estimate is even worse, with regard to mode structure and ordering, than that provided by the analysis of the $\psi_n = 0$ state.

While the addition of high order (proportional to $\nabla^n\psi$, with $n \geq 4$) dissipation is known to remove singular modes from the spectrum of fluid stability problems (Case, 1960), the Ekman dissipation—which reduces to Rayleigh damping of the PV at high wavenumbers—used here is compatible with the existence of singular modes. Numerical experiments at low resolution show that the addition of weak damping proportional to $\nabla^4\psi$ produced no systematic change in the general spatial structure of the DA modes. The decay rates of the DA modes were enhanced, but the mean PV spectra of the DA modes remained white.

With the reasonable assumption that averages over the basic cycle provide useful estimates of averages over the chaotic attractor (Samelson, 2001a), we may cautiously generalize several of the results. The scales of the unstable modes on the attractor should be similar to the scales of the background flow and have PV fluxes which are strongly correlated to the background PV gradient, especially when the background PV gradient is large. Disturbances which have scales significantly smaller than those of the background flow will tend to project onto the generalizations of the DA modes; thus, these disturbances will be simply advected and rapidly damped. As a consequence, an arbitrary initial disturbance should become dominated by large scale structures correlated with the background PV gradient in a time which is short compared to the time-scales of the background flow. This would greatly reduce the size of the space which must be searched to find initial disturbances with a large impact on the flow at moderate lead times.

3.7 Summary

The Floquet vectors (FVs) obtained here are the time-dependent normal modes for linear disturbances to the time-periodic background flow. The FVs split into two dynamical classes which have direct physical interpretations: wave dynamical (WD) modes and damped-advective (DA) modes. The WD modes are dominated by large-scale disturbances which are frequency-locked to the basic cycle. These vectors grow and decay via the same mechanisms as the basic cycle, by advecting heat (resp. vorticity) across the background temperature (resp. PV) gradient. The number of WD modes is much smaller than the total number of numerically determined FVs and these modes appear to form a discrete set. By contrast, the DA modes dominate the numerical FV spectrum and the DA class, taken as a whole, appears to represent a generalized solution to the damped advection problem, but individual DA modes do not appear to have natural physical interpretations. These modes have fine scales and decay at or near the frictional damping rate, but the detailed spatial structures of individual modes are not stable with respect to small changes in resolution or numerical method.

Accurate ensemble forecasting requires that the ensembles be initialized in such a way that their subsequent evolution is representative of the possible future states of the atmosphere or ocean. This initialization should also be economical, so that the broadest possible set of future states is achieved by the smallest possible ensemble. In the present case, the asymptotic stability of the basic cycle is determined by the leading WD modes so these modes are a natural choice for the ensemble initial conditions. These modes have the advantage that they are few in number and that they are fluid instabilities which are related, in a straightforward manner, to the background flow. This implies that the modes which are most interesting from the standpoint of geophysical fluid dynamical instability theory are also natural choices for ensemble initial conditions. Extensions of this work are in progress to address these questions also from the point of view of optimal disturbance theory.

3.8 Acknowledgement

The authors gratefully acknowledge the Office Naval Research (Grant N00014-98-1-0813) for support of this work. Computational resources were provided by the National Partnership for Advanced Computational Infrastructure and the San Diego

Supercomputer Center. CLW's committee members A. Bennett, R. deSzoeke, R. Miller, and S. Yim provided helpful suggestions that improved this work. The suggestions of an anonymous reviewer substantially improved this text.

3.9 References

Bennetin, G., L. Galgani, A. Giorgilli, and J.-M. Strelcyn, 1980: Lyapunov characteristic exponents for smooth dynamical systems and for Hamiltonian systems: A method for computing all of them. *Meccanica*, **15**, 9–21.

Case, K. M., 1960: Stability of inviscid plane Couette flow. *Phys. Fluids*, **3**, 143–148.

Charney, J. G., 1947: The dynamics of long waves in a baroclinic westerly current. *J. Meteor.*, **4**, 135–163.

Coddington, E. A. and N. Levinson, 1955: *Theory of Ordinary Differential Equations*. Krieger Publishing Company.

Cvitanović, P., R. Artuso, R. Mainieri, G. Tanner, and G. Vattay, 2005: *Chaos: Classical and Quantum*. Neils Bohr Institute, Copenhagen, ChaosBook.org.

Drazin, P. G. and W. H. Reid, 2004: *Hydrodynamical Stability*. Cambridge University Press, Cambridge, UK, second edition.

Durran, D. R., 1998: *Numerical Methods for Wave Equations in Geophysical Fluid Dynamics*. Springer-Verlag.

Eady, E. T., 1949: Long waves and cyclone waves. *Tellus*, **1**, 33–52.

Grassberger, P. and I. Procaccia, 1983: Measuring the strangeness of strange attractors. *Physica*, **9D**, 189–208.

Hart, J. E., 1981: Wavenumber selection in nonlinear baroclinic instability. *J. Atmos. Sci.*, **38**, 400–408.

Itoh, H. and M. Kimoto, 1996: Multiple attractors and chaotic itineracy in a quasi-geostrophic model with realistic topography: Implications for weather regimes and low-frequency variability. *J. Atmos. Sci.*, **53**, 2217–2231.

James, I. N., 1987: Suppression of baroclinic instability in horizontally sheared flows. *J. Atmos. Sci.*, **44**, 3710–3720.

Kazantsev, E., 1998: Unstable periodic orbits and attractor of the barotropic ocean model. *Nonlinear Processes Geophys.*, **5**, 193–208.

— 2001: Sensitivity of the attractor of the barotopic ocean model to external influences: approach by unstable periodic orbits. *Nonlinear Processes Geophys.*, **8**, 281–300.

Klein, P. and J. Pedlosky, 1986: A numerical study of baroclinic instability at large supercriticality. *J. Atmos. Sci.*, **43**, 1243–1262.

Kuchment, P., 1993: *Floquet Theory for Partial Differential Equations*. Birkhauser Verlag, Basel.

Lust, K., D. Roose, A. Spence, and A. Champneys, 1998: An adaptive Newton-Picard algorithm with subspace iteration for computing periodic solutions. *SIAM J. Sci. Comp.*, **19**, 1188–1209.

Orr, W. M., 1907: The stability or instability of the steady motions of a perfect liquid and of a viscous liquid. *Proc. Roy. Irish Acad.*, **27**, 9–138.

Oseledec, V., 1968: A multiplicative ergodic theorem. Lyapunov characteristic numbers for dynamical systems. *Trans. Moscow Math. Soc.*, **19**, 179–210.

Pedlosky, J., 1981: The nonlinear dynamics of baroclinic wave ensembles. *J. Fluid Mech.*, **102**, 169–209.

— 1987: *Geophysical Fluid Dynamics*. Springer, second edition.

Pedlosky, J. and J. Thomson, 2003: Baroclinic instability of time-dependent currents. *J. Fluid Mech.*, **490**, 189–215.

Phillips, N. A., 1954: Energy transformations and meridional circulations associated with simple baroclinic waves in a two-level, quasi-geostrophic model. *Tellus*, **6**, 273–286.

Poulin, F. J., G. R. Flierl, and J. Pedlosky, 2003: Baroclinic instability of oscillatory shear flow. *J. Fluid Mech.*, **481**, 329–353.

Samelson, R. M., 2001a: Lyapunov, floquet, and singular vectors for baroclinic waves. *Nonlinear Processes Geophys.*, **8**, 439–448.

— 2001b: Periodic orbits and disturbance growth for baroclinic waves. *J. Atmos. Sci.*, **58**, 436–450.

Samelson, R. M. and C. L. Wolfe, 2003: A nonlinear baroclinic wave-mean oscillation with multiple normal mode instabilities. *J. Atmos. Sci.*, **60**, 1186–1199.

Shimada, I. and T. Nagashima, 1979: A numerical approach to the ergodic problem of dissipative dynamical systems. *Prog. Theor. Phys.*, **61**, 1605–1616.

Toth, Z. and E. Kalnay, 1993: Ensemble forecasting at NMC: the generation of perturbations. *Bull. Am. Met. Soc.*, **12**, 2317–2330.

— 1997: Ensemble forecasting at NCEP and the breeding method. *Mon. Wea. Rev.*, **125**, 3297–3319.

4 SINGULAR VECTORS AND TIME-DEPENDENT NORMAL MODES OF A BAROCLINIC WAVE-MEAN OSCILLATION

Christopher L. Wolfe and Roger M. Samelson

To be submitted to the *Journal of the Atmospheric Sciences*

American Meteorological Society

45 Beacon Street

Boston, MA 02108

In preparation

4.1 Introduction

Geophysical flows are continually subjected to disturbances on a wide range of temporal, spatial, and amplitude scales. These disturbances often excite instabilities which cause the flows to evolve away from their previously observed or expected states. Classical studies of disturbance growth, encompassing the well-known normal-mode instability theories of fluid dynamics, concentrated on the asymptotic development of disturbances to idealized flows. Since the development of operational numerical forecasting, increasing attention has focused on the transient development of disturbances. For flows with complex time-dependence, however, the distinction between asymptotic and transient stability is often not clear. For example, many forced-dissipative flows evolve toward aperiodic attractors where all trajectories are asymptotically unstable, yet disturbances to these trajectories may go through periods of dramatic transient growth and decay.

The transient development of disturbances is typically quantified using singular values and their associated singular vectors. Singular vectors are disturbances which produce the greatest linear growth in a specified inner product over a specified optimization time interval (Lorenz, 1965; Farrell, 1989). The asymptotic stability of trajectories on aperiodic attractors is described (under suitable mathematical conditions) by Lyapunov exponents which give the average growth rate of volume elements in the attractor. In contrast to singular vectors, Lyapunov vectors associated with the Lyapunov exponents may be defined in a manner which is independent of inner product or time-interval (e.g., Eckmann and Ruelle, 1985; Trevisan and Pancotti, 1998; Wolfe and Samelson, 2006b). Lyapunov vectors often undergo significant transient growth and decay in addition to their asymptotic, exponential evolution.

Both singular vectors and an analog of Lyapunov vectors, bred vectors, are currently in use at operational forecasting centers as initial conditions for ensemble forecasting systems (Buizza et al., 2005). Bred vectors are generated through a repeated 'breeding' cycle by which the differences between the analysis and the ensemble members are rescaled and added back to the analysis to generate a new set of ensemble initial conditions (Toth and Kalnay, 1993, 1997). Since the ensemble forecast models are nonlinear, bred vectors of sufficient magnitude are nonlinear disturbances. If the amplitude of the bred vectors is constrained so that they disturbances remain linear, the process by which bred vectors are generated is analogous to the methods used to estimate the Lyapunov exponents of dynamical systems (Oseledec, 1968; Eckmann and Ruelle, 1985).

In the present contribution, we examine the mathematical and physical relationships between singular vectors and Lyapunov vectors. The relationship between these quantities is of interest not only because of the connections to ensemble forecasting, but also because Lyapunov exponents and vectors are intrinsic, asymptotic properties of a dynamical system's attractor, whereas singular values and vectors depend both on the choice of inner product and the time-interval of interest. Further, the connection between transient and asymptotic stability in strongly time-dependent systems has primarily been studied using either highly simplified, low-order models (e.g. Lorenz, 1965; Trevisan and Pancotti, 1998; Samelson, 2001b) or models with complexity comparable to global circulation models (e.g. Buizza and Palmer, 1995; Palmer, 1996; Wei and Frederiksen, 2004). Examples of accessible, intermediate complexity models are few (with exceptions; see, e.g., Moore and Mariano, 1999; Samelson and Tziperman, 2001; Miller and Ehret, 2002). One goal of the present contribution is to present an accessible system wherein the relationships between asymptotic and transient stability may be examined in detail.

The system under study is the nonlinear Phillips (1954) model. This model is chosen because it is relatively well understood and occupies a middle ground in complexity between the low-dimensional models used in classical predictability studies and operational forecast models. The intermediate complexity of the model allows the representation of non-trivial physics while still admitting a relatively complete analysis.

Most of the present analysis focuses on a single unstable, nonlinear, time-periodic oscillation (cycle) of the model. Periodic cycles are convenient because full information about the evolution of linear disturbances can be obtained by a single integration over the cycle. Additionally, time-periodicity imposes a definite modal structure on the linear space tangent to the cycle in the form of Floquet vectors, which are intrinsic quantities that completely characterize the evolution of linear disturbances to the cycle. Floquet vectors may be unambiguously identified as both normal modes and Lyapunov vectors. The wave-mean oscillation that will be considered here and the associated Floquet vectors are described in detail in Wolfe and Samelson (2006a, hereafter WS), which should be considered a companion to the present contribution.

The format of the paper is as follows: In section 4.2, we briefly describe the model and basic cycle used for the present analysis. We then briefly review the characteristics of the Floquet vectors associated with the basic cycle in section 4.3. Section 4.4 is devoted to a detailed discussion of the singular vectors and their relationship to the Floquet vectors. In section 4.5, we examine the relationship of the Floquet vectors and singular vectors to the local structure of the system's attractor. A method for recovering the Floquet vectors from the singular vectors is described and demonstrated in section 4.6. The significance of the results are discussed in section 4.7. Finally, we summarize in section 4.8.

4.2 Model and Basic Cycle

The model studied here is the Phillips (1954) quasigeostrophic channel model and is described in Pedlosky (1987, §7). For the present study, the Coriolis parameter f is constant, the equilibrium layer depths are equal, and the background flow is steady, uniform, and zonal. The evolution of arbitrary amplitude disturbances to the background flow is governed by

$$\begin{aligned} &\frac{\partial q_n}{\partial t} + U_n \frac{\partial q_n}{\partial x} + J(\psi_n, q_n) - (-1)^n F U_s \frac{\partial \psi_n}{\partial x} = -r\nabla^2 \psi_n \\ &q_n = \nabla^2 \psi_n + (-1)^n F(\psi_1 - \psi_2) \end{aligned} \qquad n = 1, 2 \tag{4.1}$$

where ψ_n and q_n are the disturbance streamfunctions and potential vorticities, respectively, and the background flow has been chosen so that $U_1 = -U_2 = U_s/2$. The two parameters controlling the behavior of the system are the Froude number F and the Ekman dissipation parameter r. In the notation of Klein and Pedlosky (1986), we use

$$\Delta \equiv F - \pi^2 - 4r^2 = 45,$$

$$\gamma \equiv r\sqrt{\frac{8}{\Delta}} = 0.20$$

for the present study, which corresponds to the most strongly supercritical set of parameters considered by Klein and Pedlosky (1986).

The equations were solved in the manner described in WS, except that Adams-Bashforth three-level time-differencing scheme was used throughout. Also, since the singular vector calculation is numerically more stable than the Floquet problem, we were able to use a slightly lower resolution than WS. Thus, the results of the present study were obtained using $N_x = 48$ zonal and $N_y = 40$ meridional grid points, for a total of 3840 variables, and a time step of $\Delta t = 0.0015$.

The wave-mean oscillation considered here is a fully nonlinear, time-periodic solution to (4.1) and will henceforth be referred to as the "basic cycle." It has a period of $T \approx 38.498$, and begins as a nearly-zonal flow with a small superimposed perturbation. This perturbation grows into a pair of eddies which grow in amplitude as they advect heat (proportional to $\psi_T = \psi_1 - \psi_2$) down-gradient, across the channel. By $t = 0.3T$, these eddies are strongly nonlinear and have closed streamfunction contours. The cross-channel heat flux produced by these eddies reduces the background potential vorticity gradient sufficiently to halt and then reverse the growth of the eddies. Toward the end of the decay phase, the weakening eddies advect heat up-gradient, extracting energy from the wave and re-establishing the nearly-zonal initial state, now shifted down-channel by one-half the channel length. After passing through a second growth and decay phase the flow returns to its initial state.

The period of the basic cycle is much longer than either the advective or viscous time scales,

$$T_a = \frac{1}{U_{\max}} \approx 0.02T \tag{4.2}$$

$$T_v = \frac{1}{r} \approx 0.05T, \tag{4.3}$$

respectively. Since the basic cycle undergoes two growth and decay episodes in each period, the characteristic time scale for baroclinic wave growth is

$$T_w \approx 0.25T. \tag{4.4}$$

Based on the above scales, we expect advective alignment of disturbances to be important only on extremely short time scales. Baroclinic processes related to the growth and maintenance of the basic cycle are expected to dominate disturbance growth for moderate to long time scales.

4.3 Floquet Vectors

For a detailed discussion of the Floquet vectors and their spatio-temporal structure, see WS. A short summary of the results of WS is included here for completeness.

Floquet vectors (FVs) $\boldsymbol{\phi}_i$ are the eigenvectors of the one-period linear disturbance propagator $\mathcal{L}(T)$ and completely characterize the evolution of linear disturbances to a time-periodic cycle. The spatio-temporal characteristics and asymptotic stability of the FVs thus determine if and how the basic cycle becomes unstable. In the present case, three of the FVs are unstable and two are neutral, indicating that the basic cycle is, in fact, unstable. The number of unstable and neutral modes is independent of resolution and thus is a characteristic of the basic cycle only. The rest of the Floquet spectrum is completed by a large number of decaying modes, the exact number of which depends on resolution.

The exponential growth of the unstable FVs is relatively slow, with e-folding times of

$$T_1 \approx 0.9T,$$

$$T_2 \approx 1.2T,$$

$$T_3 \approx 3.6T,$$

for the first, second, and third FVs, respectively. While these time scales are longer than the transient baroclinic wave growth time scale T_w, the leading FVs undergo significant transient growth and decay in phase with the basic cycle. The maximum transient growth rate of the unstable FVs is inner product dependent, but is on average about ten times faster than the exponential growth rate in most physically motivated inner products.

In addition to the three unstable FVs, the Floquet spectrum contains two neutral modes $\boldsymbol{\phi}_4$ and $\boldsymbol{\phi}_5$ which are proportional to the time and zonal, respectively, derivatives of the basic cycle. These neutral modes arise as a consequence of the two continuous symmetries, temporal- and zonal-translation, of (4.1).

The majority of the FVs have exponents whose real parts lie near the dissipation rate r, while a small number of vectors have exponents whose real parts are significantly greater, or less, than the dissipation rate. Thus, the bulk of the FVs are stable and decay at rates near the dissipation rate of the model. The leading vectors either grow or decay weakly while the trailing vectors decay much more rapidly than the dissipation rate.

FVs with decay rates well separated from the dissipation rate tend to be dominated by disturbances with large scales, while those with decay rates near the dissipation rate have much smaller scales. These two classes will be referred to as the "wave-dynamical" (WD) and "damped-advective" (DA) classes, respectively. Those FVs with large scales have—with few exceptions—purely real Floquet exponents (i.e. they are frequency-locked to the basic cycle). While the large scale FVs are dominated by a small number of Fourier components, the fine-scale FVs tend to contain significant contributions from many Fourier components. These FVs have complex Floquet exponents with real parts that lie near the dissipation rate and imaginary parts which are distributed approximately uniformly between $\pm\pi/T$ (i.e., their periods differ from that of the basic cycle).

An important property of these FVs from the point of optimal disturbances (singular vectors) is that they are non-orthogonal in the inner products considered in section 4.4. This follows from the fact that the one-period propagator $\mathcal{L}(T)$ is non-normal (i.e., it does not commute with its adjoint $\mathcal{L}(T)^\dagger$) in these inner products. A further consequence of the non-normality of $\mathcal{L}(T)$ is that the adjoint FVs $\boldsymbol{\theta}_i$, the eigenvectors of the adjoint propagator, are distinct from the 'forward' FVs $\boldsymbol{\phi}_i$. The $\boldsymbol{\theta}_i$ are non-orthogonal, as well, but can be ordered so that they satisfy the following orthogonality relationship with the $\boldsymbol{\phi}_i$:

$$\langle \boldsymbol{\theta}_i, \boldsymbol{\phi}_j \rangle = \Pi_{ij}^{-1}\delta_{ij}, \tag{4.5}$$

where $\mathbf{\Pi}$ is a diagonal matrix whose nonzero entries are the 'projectabilities' of the adjoint FVs onto the forward FVs (Zhang, 1988).

If the chosen inner product $\langle \cdot, \cdot \rangle$ is characterized by the matrix $\mathbf{N}$ such that

$$\langle \boldsymbol{v}, \boldsymbol{w} \rangle = \boldsymbol{v}^{\mathrm{T}}\mathbf{N}\boldsymbol{w}, \tag{4.6}$$

then the adjoint propagator satisfies

$$\mathbf{N}\mathcal{L}(T)^\dagger = \mathcal{L}(T)^{\mathrm{T}}\mathbf{N}. \tag{4.7}$$

The $\boldsymbol{\theta}_i$ may then be defined in terms of the $\boldsymbol{\phi}_i$ as

$$\mathbf{T} = \mathbf{N}^{-1}\mathbf{F}^{-\mathrm{T}}\mathbf{\Pi}^{-1}, \tag{4.8}$$

where $\mathbf{T}$ and $\mathbf{F}$ are matrices whose columns are the $\boldsymbol{\theta}_i$ and $\boldsymbol{\phi}_i$, respectively. While matrix inversion is not necessarily more efficient then eigenvalue decomposition, computation of the adjoint FVs via (4.8) ensures that they are automatically sorted properly.

The primary property of the $\boldsymbol{\theta}_i$ which will be of use in the present study is that, for large optimization times, the adjoint FV $\boldsymbol{\theta}_i$ is the optimal excitation of $\boldsymbol{\phi}_i$ with respect to the inner product defining the adjoint. (Farrell (1989) and Buizza and Palmer (1995) demonstrate this fact for stationary flows. The extension to time-periodic flows is straightforward.) That is, $\boldsymbol{\theta}_i$ is the smallest perturbation at time t_0 which will produce an excitation of $\boldsymbol{\phi}_i$ at unit amplitude at a later time t_1.

4.4 Singular Vectors

4.4.1 Formulation

Singular vectors (SVs) optimize the growth of perturbations in a specified inner product over a specified optimization interval $\tau = t_1 - t_0$. Let $\boldsymbol{\xi}_j(t)$ represent the j^{th} most rapidly growing SV. Since the FVs span the space of linear disturbances, $\boldsymbol{\xi}_j(t)$ may be written as a fixed sum of FVs,

$$\boldsymbol{\xi}_j(t) = \sum_{i=1}^{N} \boldsymbol{\phi}_i(t) p_{ij} = \mathbf{F}(t)\boldsymbol{p}_j. \tag{4.9}$$

The projection coefficients $\boldsymbol{p}_j$ are independent of time, so if the $\boldsymbol{\phi}_i(t)$ are known, $\boldsymbol{\xi}_j(t)$ is determined for all time. The SV optimization problem leads, in the usual way (e.g. Buizza et al., 1993), to the generalized eigenvalue problem

$$\mathbf{F}(t_1)^{\mathrm{T}}\mathbf{N}\mathbf{F}(t_1)\boldsymbol{p}_j = \sigma_j^2 \mathbf{F}(t_0)^{\mathrm{T}}\mathbf{N}\mathbf{F}(t_0)\boldsymbol{p}_j \tag{4.10}$$

for the SVs and the singular values σ_j, where $\mathbf{N}$ is the matrix which characterizes the specified inner product. Note that the $\boldsymbol{p}_j$ are not invariant under an arbitrary rescaling of the FVs; in what follows, we have chosen the FVs to have unit amplitude in the specified norm at the initialization time t_0.

The SV $\boldsymbol{\xi}_j$ may equivalently be written as a fixed sum of adjoint FVs $\boldsymbol{\theta}_i(t)$,

$$\boldsymbol{\xi}_j(t) = \sum_{i=1}^{N} \boldsymbol{\theta}_i(t) q_{ij} = \mathbf{T}(t)\boldsymbol{q}_j. \tag{4.11}$$

Such an expansion is useful since, for large optimization intervals, the optimal excitation of the normal mode $\boldsymbol{\phi}_i$ is the corresponding adjoint normal mode $\boldsymbol{\theta}_i$ (Farrell, 1989; Buizza and Palmer, 1995). The $\boldsymbol{q}_j$ satisfy the generalized eigenvalue problem

$$\mathbf{T}(t_1)^{\mathrm{T}}\mathbf{N}\mathbf{T}(t_1)\boldsymbol{q}_j = \sigma_j^{-2}\mathbf{T}(t_0)^{\mathrm{T}}\mathbf{N}\mathbf{T}(t_0)\boldsymbol{q}_j, \tag{4.12}$$

but if—as in the present case—the complete set of FVs is available, the $\boldsymbol{q}_j$ may be more efficiently computed using

$$\boldsymbol{q}_j = \mathbf{T}(t_0)^{-1}\mathbf{F}(t_0)\boldsymbol{p}_j = \boldsymbol{\Pi}\mathbf{F}(t_0)^{\mathrm{T}}\mathbf{N}\mathbf{F}(t_0)\boldsymbol{p}_j, \tag{4.13}$$

where the last equality follows from (4.8). Note that the RHS of (4.13) is merely the RHS of (4.10) weighted by the projectability factors $\boldsymbol{\Pi}$.

The SVs depend on the initialization and optimization times t_0 and t_1 as well as on the inner products defined by the matrix $\mathbf{N}$. We have calculated SVs using inner products $\langle \cdot, \cdot \rangle$ corresponding to the streamfunction variance (SA), wave energy (WE), and potential enstrophy (PV). These inner products are defined as follows:

$$\langle \boldsymbol{v}, \boldsymbol{w} \rangle_{\mathrm{SA}} = \sum_{n=1}^{2} \iint \psi_n^{(\boldsymbol{v})} \psi_n^{(\boldsymbol{w})}\, dx\, dy, \tag{4.14}$$

$$\begin{aligned}\langle \boldsymbol{v}, \boldsymbol{w} \rangle_{\mathrm{WE}} = \sum_{n=1}^{2} \frac{1}{2} \iint \nabla\psi_n^{(\boldsymbol{v})} \cdot \nabla\psi_n^{(\boldsymbol{w})}\, dx\, dy \\ + \frac{F}{2} \iint (\psi_1^{(\boldsymbol{v})} - \psi_2^{(\boldsymbol{v})})(\psi_1^{(\boldsymbol{w})} - \psi_2^{(\boldsymbol{w})})\, dx\, dy,\end{aligned} \tag{4.15}$$

$$\langle \boldsymbol{v}, \boldsymbol{w} \rangle_{\mathrm{PV}} = \sum_{n=1}^{2} \iint q_n^{(\boldsymbol{v})} q_n^{(\boldsymbol{w})}\, dx\, dy, \tag{4.16}$$

where $\psi^{(\boldsymbol{v},\boldsymbol{w})}$ and $q^{(\boldsymbol{v},\boldsymbol{w})}$ denote the streamfunction and potential vorticity associated with the state vectors $\boldsymbol{v}$ and $\boldsymbol{w}$ and the integrals are taken over the entire domain.

4.4.2 Results

Singular vectors are computed for the unstable basic cycle. The dependence on both the initialization time t_0 and optimization interval τ is investigated by computing SVs with fixed t_0, but variable τ, and fixed τ, but variable t_0. The eigenvalue problem eq. (4.10) for the SVs yields as many SVs as model variables (in this case, 3840). A subset of the calculations were repeated at higher resolution with little change in the structure of the extremal (i.e., most rapidly growing and decaying) SVs. The SVs in the middle of the spectrum—which are not the focus of the present contribution—changed in number and detailed physical structure with changes in resolution, but their overall statistical character remained the same. See WS for a detailed discussion of the effects of resolution on the structure of linear disturbances to the basic cycle.

4.4.2.1 Fixed initialization time

The singular values undergo a short period of super-Lyapunov (i.e., faster than the exponential growth rate of the FVs) growth and decay for short optimization intervals (Fig. 4.1). The rapid transient growth period is more pronounced in the SA inner product than in the WE inner product, while the SVs in the WE inner product similarly show more transient growth than the SVs in the PV inner product (Fig. 4.2). In all cases the growth rate singular values becomes comparable to the effective exponential growth rate of the FVs,

$$\lambda_{\mathrm{eff},j}(t_2) = \frac{1}{t_2 - t_1} \ln \frac{\|\phi_j(t_2)\|}{\|\phi_j(t_1)\|}, \tag{4.17}$$

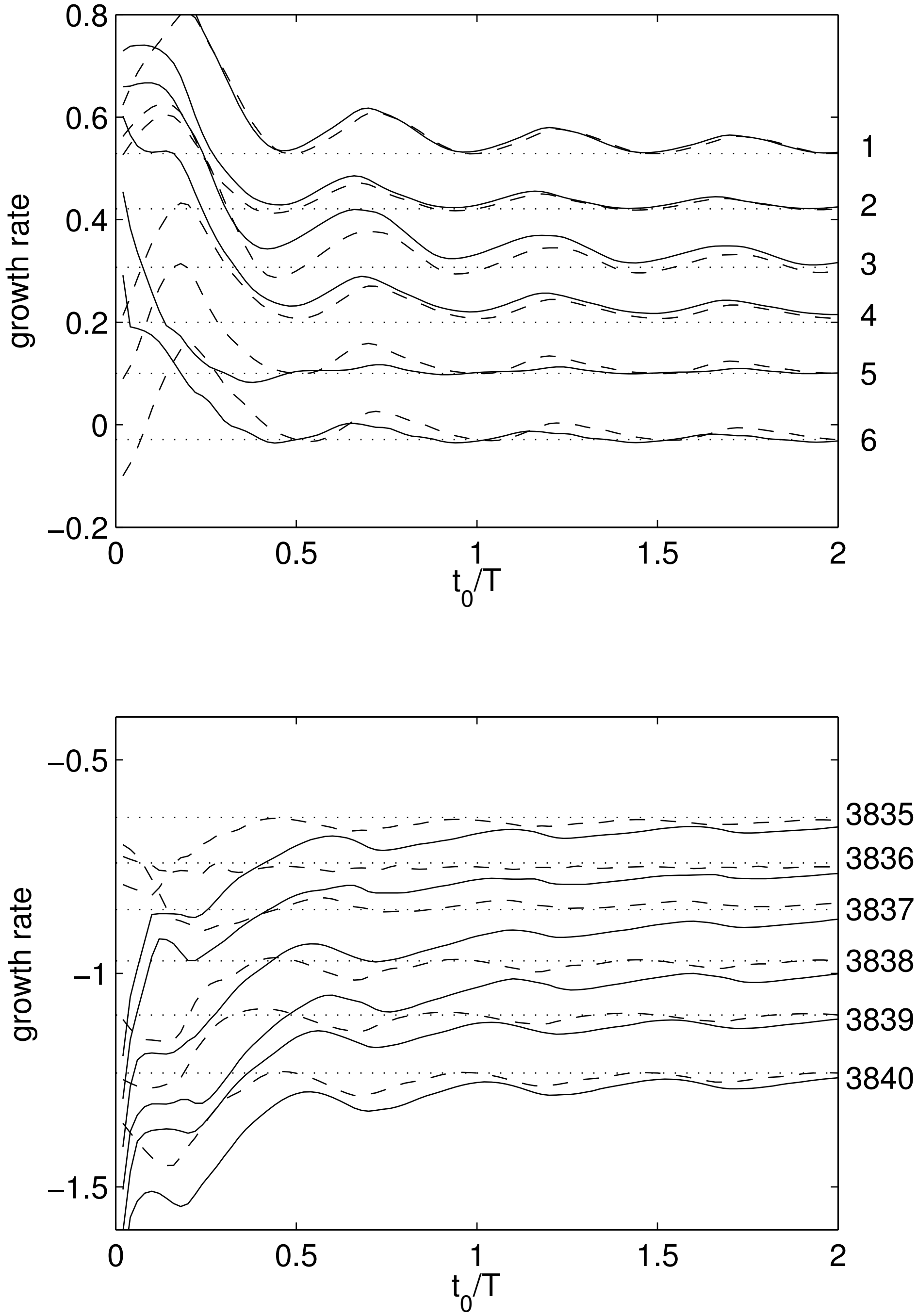

FIGURE 4.1: Effective exponential growth rate $\lambda_{\rm eff} = \ln \sigma(\tau)/\tau$ of the first (upper panel) and last (lower panel) ten SVs (solid) and FVs (dashed) in the WE norm, as well as the respective Floquet exponents (dotted) as a function of optimization interval τ/T. The growth rates have been offset from each other by 0.1 clarity. The least rapidly growing (upper panel) and decaying (lower panel) vectors have zero offset. The indices of the FVs and SVs are given to the right of the panels.

for optimization intervals greater than a few advective time scales T_a, or roughly one baroclinic growth time scale $T_w \approx 0.25T$ (Fig. 4.1). Further, the growth rates of the SVs asymptotically approach the Floquet exponents as the optimization interval τ increases.

Once $\tau \gtrsim T_w$, the SVs in each inner product divide into two classes much like the FVs. The first class, which may be identified with the wave-dynamical (WD) class, is made up of vectors whose singular values either grow or decay at rates which are significantly different than the dissipation rate. The second class is made up of a large number of SVs which decay at or near the dissipation rate, and SVs may be identified with the damped-advective (DA) class. These SVs were calculated, but are omitted from figure 4.2 for clarity. The WD singular values show pronounced oscillations on the time scale of the basic cycle wave growth time scale T_w. These oscillations are in phase with the basic cycle in the SA inner product, but slightly trail the basic cycle in the WE and PV inner product. This difference is most likely due to the fact that energy and PV disturbances continue to sharpen during the early parts of the basic cycle decay phase.

While the WD singular values are well separated relative to the DA singular values, the separation is not perfect and the SVs exchange stability frequently, which makes the ranking of the SVs ambiguous. For this section, the numerical ranking of the SVs is based on the ranking of the corresponding singular values at the largest optimization interval considered ($\tau = 2T$). Thus, $\boldsymbol{\xi}_1$ is the leading SV at time $\tau = 2T$, but since the SVs exchange stability as the optimization interval is changed, $\boldsymbol{\xi}_1$ may not be the leading SV for $\tau < 2T$. Since the physical structures of the SVs change continuously as the optimization interval is varied, the individual SVs may be consistently identified even if the singular values cross.

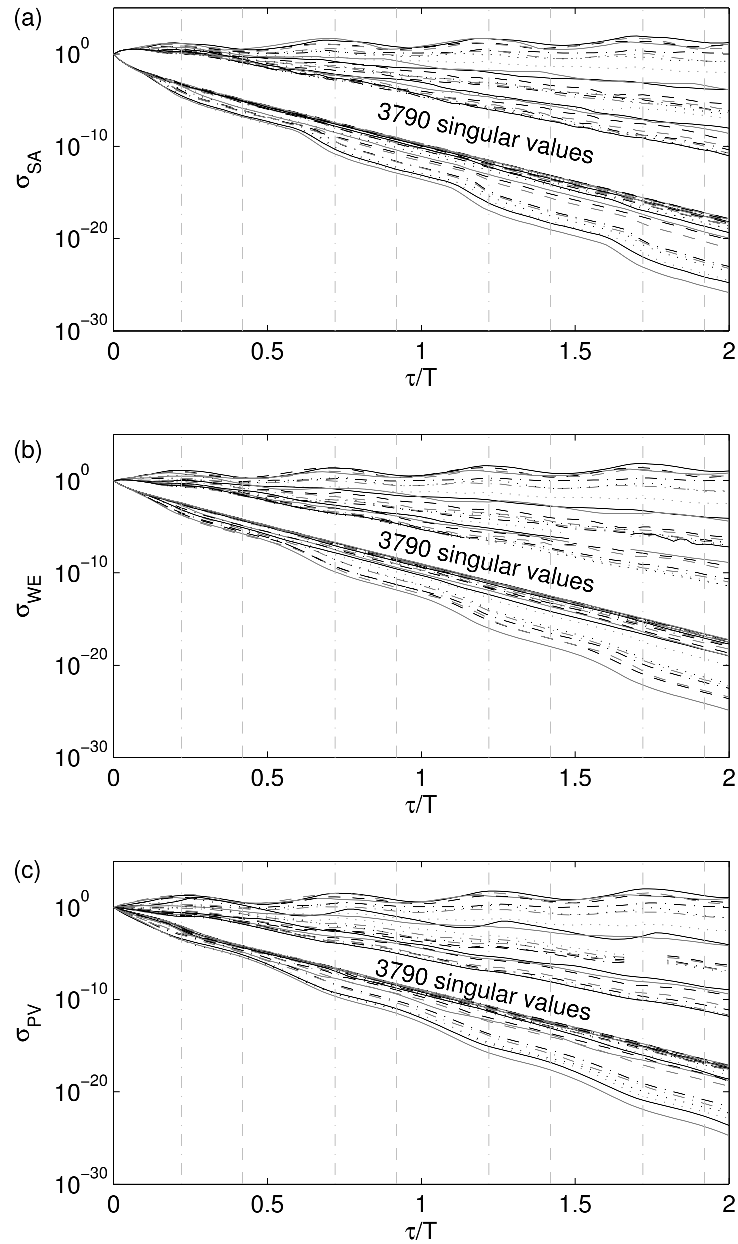

FIGURE 4.2: Singular values in the (a) SA, (b) WE, and (c) PV inner products vs optimization interval τ/T for fixed initialization time t_0 near a basic cycle minimum. For clarity, on the the first and last 25 singular values are shown. Some of the singular values did not converge in the WE and PV inner product at large optimization times; these values are omitted. The maxima and minima of the basic cycle are denoted by the vertical dash-dotted and dashed lines, respectively.

For the remainder of this section, the discussion will focus on the SVs computed in the WE inner product, with comments on the SA and PV SVs only when their behavior differs significantly from the WE SVs. This focus on the WE SVs is reasonable both because they typically show behavior which is intermediate between the SA and PV SVs and because the WE inner product is the analog, in the Phillips model, of the 'total energy' inner product commonly used to compute singular vectors in atmospheric global circulation models (Buizza and Palmer, 1995; Palmer, 1996).

The leading WE SVs show significant contributions from a large number of FVs (Fig. 4.3). The largest contributions often come from weakly decaying WD FVs or from DA FVs, while the leading FVs are typically subdominant. By contrast, the leading SVs are relatively simple functions of a small number of the adjoint FVs (Fig. 4.4). In fact, for $\tau \gtrsim 2T_w$, the leading SVs are nearly optimal excitations of the leading FVs. Thus, by the optimization time, the leading SVs will be nearly collinear with the leading FVs. Note that both $\boldsymbol{\xi}_2$ and $\boldsymbol{\xi}_5$ (resp. $\boldsymbol{\xi}_3$ and $\boldsymbol{\xi}_6$) have large projections onto $\boldsymbol{\theta}_2$ and $\boldsymbol{\theta}_4$ (resp. $\boldsymbol{\theta}_3$ and $\boldsymbol{\theta}_6$), but the roles of the adjoint FVs are reversed. This occurs because $\boldsymbol{\theta}_2$ and $\boldsymbol{\theta}_4$ (resp. $\boldsymbol{\theta}_3$ and $\boldsymbol{\theta}_6$) are orthogonal, or nearly so, in all three inner products, to all of the leading adjoint FVs except each other.

For short optimization intervals $\tau \approx T_a$, the leading WE SVs show the classic 'chevron' shape formed by the disturbances leaning into the horizontal shear (Zeng, 1983; Buizza and Palmer, 1995), which is maximum at the channel walls (Fig. 4.5a shows $\boldsymbol{\xi}_1$, the other leading SVs are similar). By the optimization time, the shear has straightened out the disturbances (Fig. 4.5b). Once the optimization interval approaches T_w (Figs. 4.5c–h), the leading SVs show little sensitivity to the precise

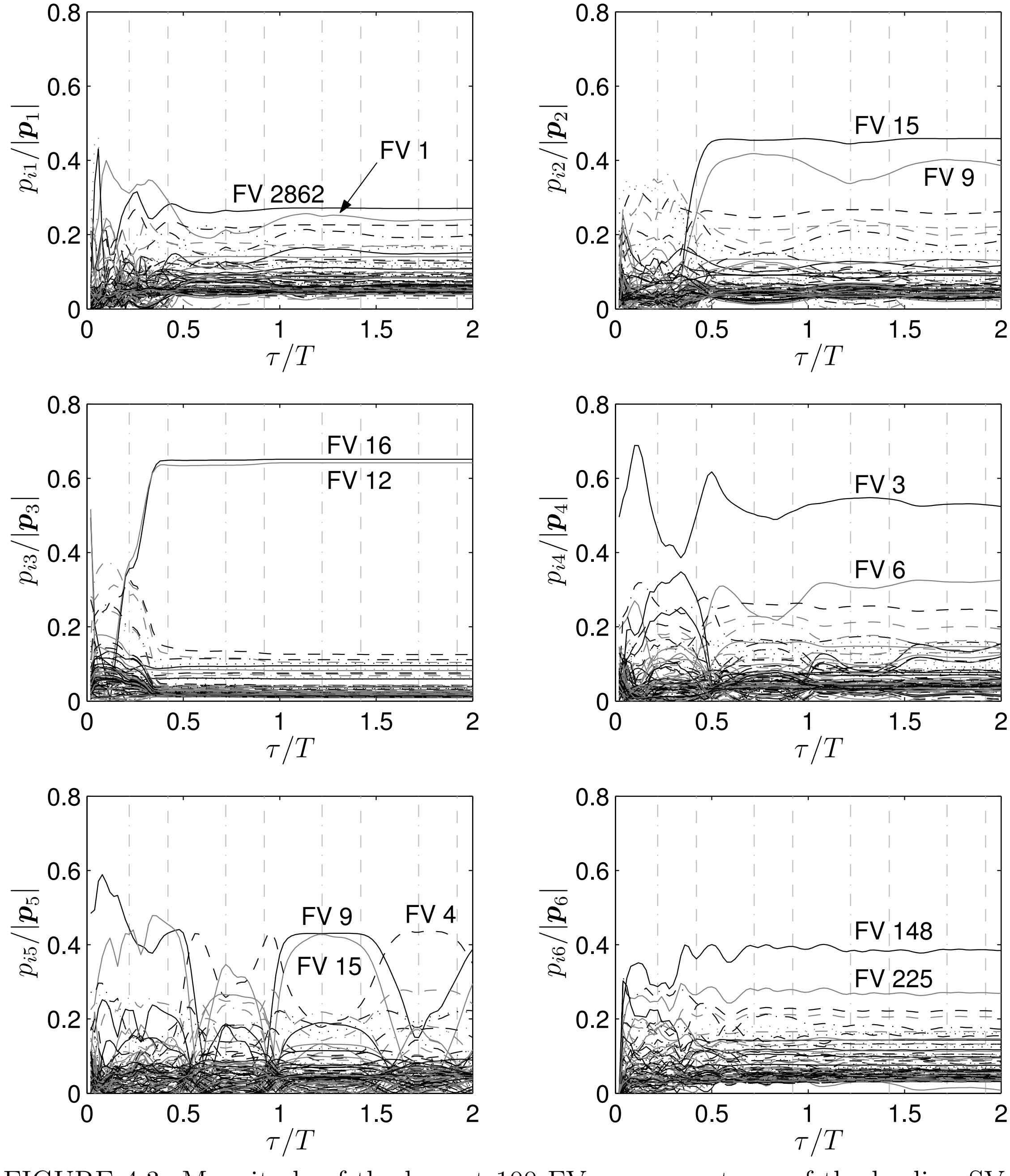

FIGURE 4.3: Magnitude of the largest 100 FV components $\boldsymbol{p}_j$ of the leading SVs $\boldsymbol{\xi}_j$ in the WE inner product vs optimization interval τ/T for fixed initialization time t_1. The Floquet index of the dominant SV component is noted in each plot. The vertical lines are as in figure 4.2

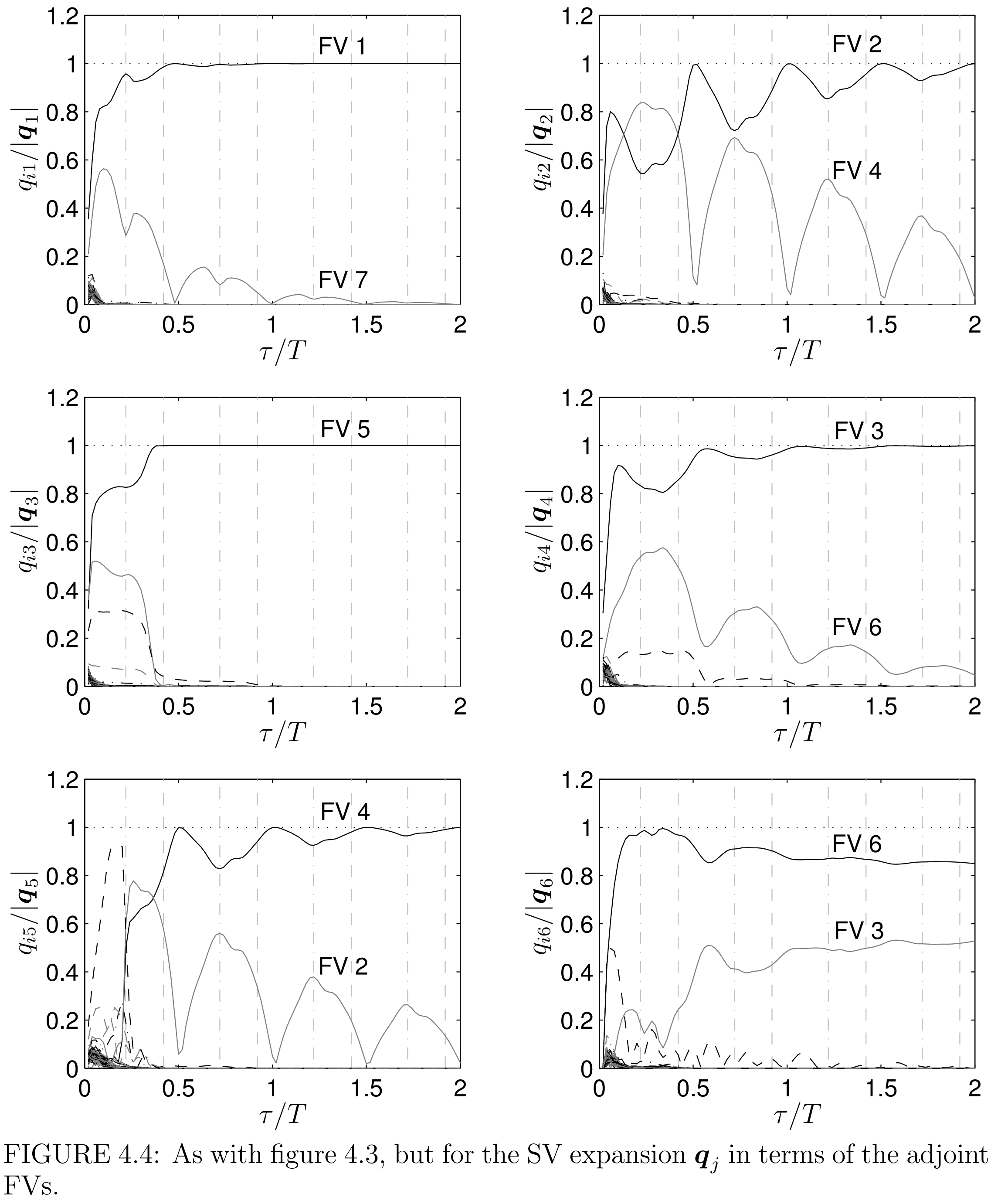

FIGURE 4.4: As with figure 4.3, but for the SV expansion $\boldsymbol{q}_j$ in terms of the adjoint FVs.

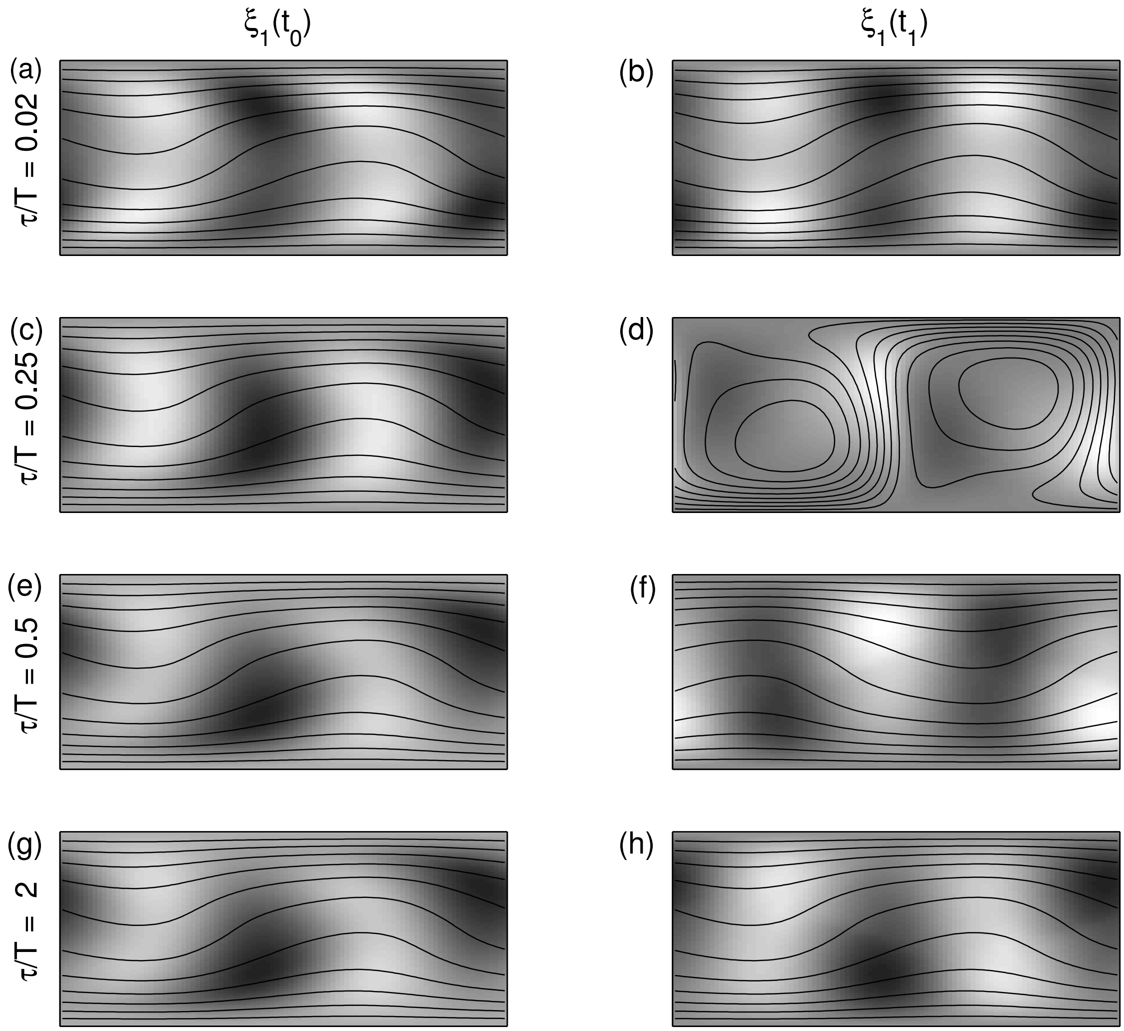

FIGURE 4.5: The initial $\boldsymbol{\xi}_1(t_0)$ (left panels) and final $\boldsymbol{\xi}_1(t_1)$ (right panels) upper layer streamfunction of the leading WE SV (colors) initialized near the basic cycle minimum at four optimization intervals τ. Also shown is the upper level streamfunction of the basic cycle (contours). Since the SVs are linear disturbances, the color scale is arbitrary.

value of the optimization time, consistent with their FV decompositions (Figs 4.3 & 4.4). While baroclinic processes dominate the growth processes for longer optimization intervals, the initial disturbances still show some tendency to lean into the shear, forming distorted chevron shapes (Figs. 4.5c, e, & g). Interestingly, all of the leading SVs show a westward phase shift with height, even those whose optimization intervals are much less than the baroclinic time scale T_w. Thus, even those disturbances which obtain most of their transient growth through advective alignment are set up to continue their growth due to baroclinic processes. As expected from the adjoint Floquet decomposition $\boldsymbol{q}_1$ (Fig. 4.4), the final conditions of the leading SV (Figs. 4.5d, f & h) strongly resemble the leading FV (see WS, figure 5).

For optimization intervals $\tau \gtrsim 2T_w$, the most rapidly damped SVs project onto only the most rapidly damped FVs (Fig. 4.6). This is a consequence of the optimization problem which defines the SVs: the most rapidly damped SVs can only project onto the most rapidly damped FVs, since if they did not they would decay less rapidly. As with the leading SVs, the FV components of the most rapidly decaying SVs tend to occur in alternating pairs due to the fact that the FV pairs $\boldsymbol{\phi}_{3835,3839}$, $\boldsymbol{\phi}_{3836,3840}$, and $\boldsymbol{\phi}_{3837,3838}$ are orthogonal (to within numerical precision), in all three inner products, to all the other rapidly decaying FVs except each other.

For $\tau \approx T_a$ (Fig. 4.7a), the initial conditions for the rapidly decaying SVs are localized in regions of strong shear and take the form of very fine-scale disturbances which tilt 'out' of the shear (i.e., in the opposite sense as the leading SVs). By the optimization time, these disturbances have been advected downstream and extended by the shear into thin filaments (Fig. 4.7b). The initial conditions of the rapidly decaying SVs become independent of the optimization interval even more quickly than the leading SVs and, by $\tau \approx T_w$ strongly resemble the most rapidly decaying

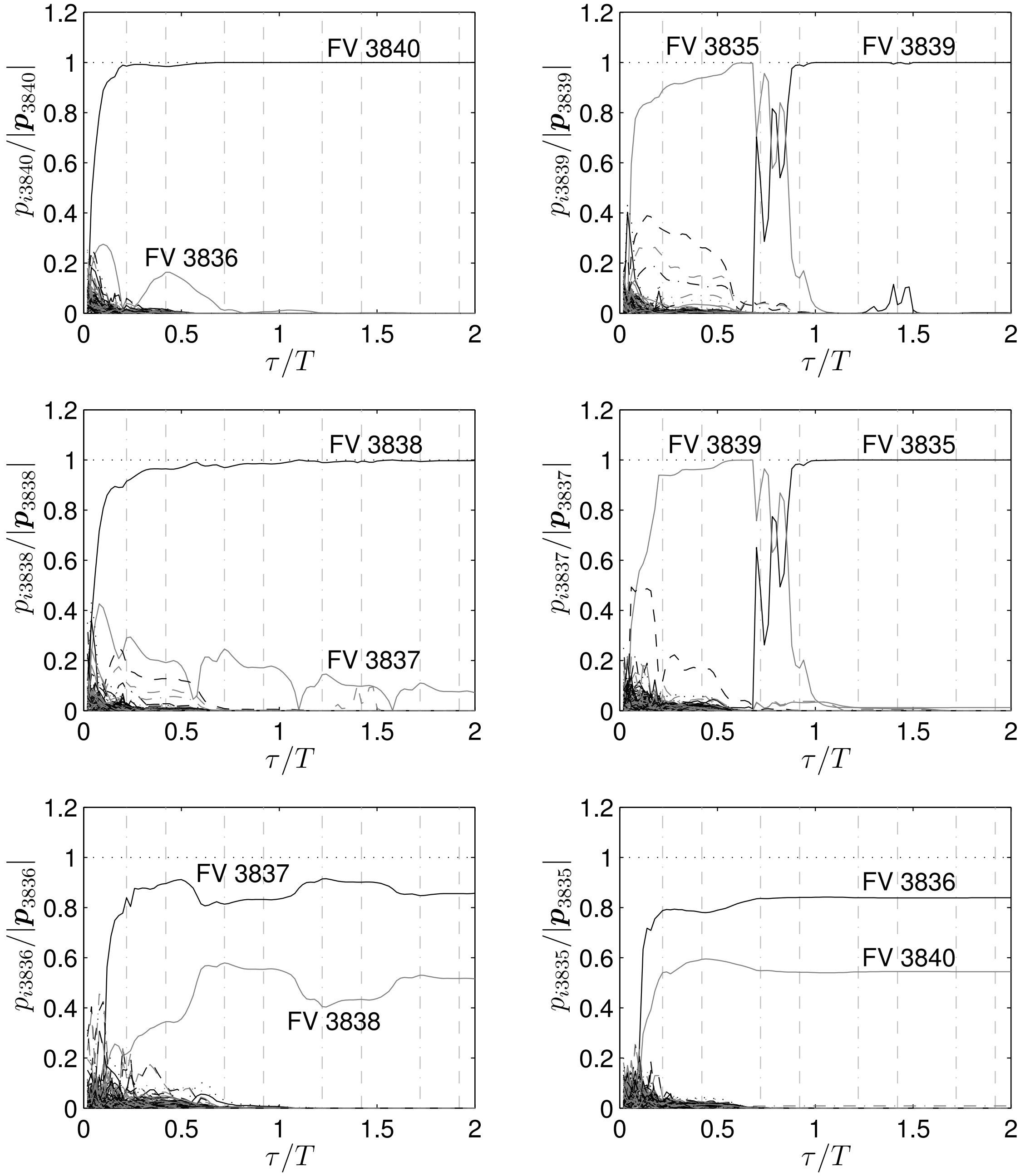

FIGURE 4.6: As with figure 4.3, but for the most rapidly decaying SVs.

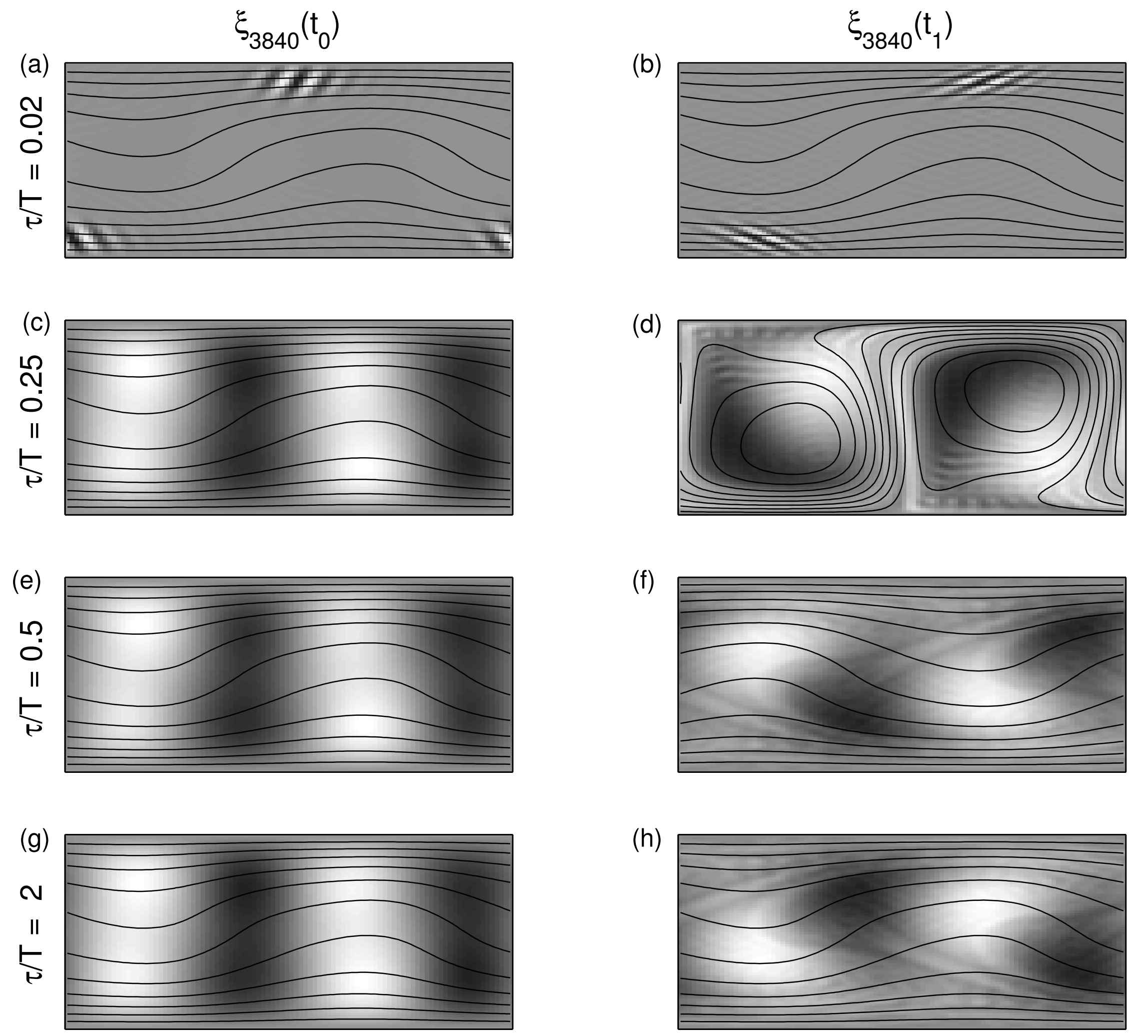

FIGURE 4.7: As with figure 4.5, but for the SV $\boldsymbol{\xi}_{3840}$.

norm	$\|\mathbf{F}_0\mathbf{N}\mathbf{F}_0 - \mathbf{I}\|_2$
SA	153
WE	46.9
PV	12.8

TABLE 4.1: 2-norm of the off-diagonal part of the matrix of inner products $\mathbf{F}_0\mathbf{N}\mathbf{F}_0$ in the three inner products. The extremal possibilities are $\|\mathbf{F}_0\mathbf{N}\mathbf{F}_0 - \mathbf{I}\|_2 = 0$ if all FVs are orthogonal and $\|\mathbf{F}_0\mathbf{N}\mathbf{F}_0 - \mathbf{I}\|_2 = 3839$ if all FVs are collinear.

FVs (compare figs. 4.7c, e, & g to WS fig. 9). The final conditions at moderate to long optimization intervals appear filamented (Fig. 4.7d) or ragged (Figs. 4.7f & h). These structures are not very meaningful physically because they are determined by the very small amplitude Floquet components that are left after the trailing FVs decay away. These components are primarily determined by the requirement that the final conditions of the decaying SVs are orthogonal to all the less rapidly decaying SVs and their small amplitude makes them subject to numerical noise.

Both the leading and most rapidly decaying SVs appear to be converging to constant linear combinations of FVs as τ increases, for all inner products considered (Figs. 4.3, 4.4, & 4.6). The rate of convergence, however, is different for different SVs, as $\boldsymbol{\xi}_4$ and $\boldsymbol{\xi}_5$ still show marked oscillations in their (adjoint) FV decompositions for the largest optimization intervals shown. In fact, the SVs converge exponentially at a rate which may be estimated from the Floquet exponents to orthogonalizations of the FVs as the optimization time $|\tau| \to \infty$ (Wolfe and Samelson, 2006b). This convergence will be explored more fully in in section 4.6.

The Floquet decompositions of the SVs in the other two inner products are qualitatively similar. The primary difference is that, as the number of derivatives in the inner product decreases, the number of FVs contributing significantly to each SV increases. This is due to the fact that the FVs themselves become closer to orthogonal as the number of derivatives in the inner product increases (Table 4.1). Additionally, the physical structures of the SVs in the SA inner product are of significantly finer scale, while those in the PV inner product take the form of channel-scale disturbances. The scale evolution of the SVs in all three inner products is explored more fully in section 4.4.2.2.

Essentially identical results obtain if the initialization time is chosen to be near a cycle maximum, except that the initial, advective growth is more rapid due to the stronger shear field present near the cycle maximum.

4.4.2.2 Fixed optimization interval $\tau = T$

The results of the previous section show that, for a fixed initialization time, the leading SVs rapidly approach optimal excitations of the leading FVs while the rapidly decaying SVs tend toward the rapidly deacying FVs. It is not immediately clear, however, that this result holds for arbitrary initialization times. Further, the background flow and FVs undergo significant changes in spatial structure as the basic cycle evolves. The SVs may be expected to undergo similar changes in structure as the initialization time varies throughout the basic cycle. It is of interest to determine if the SVs remain relatively simple functions of the FVs even though both are repectively strongly time-dependent.

To this end, we examine the SVs as a function of initialization time with optimization interval fixed to $\tau = T$, the period of the basic cycle. This choice of the optimization interval simplifies the interpretation of changes in the SVs initial and final conditions because the state of the basic cycle is identical at the initialization and optimization times. The interval $\tau = T$ encompases two baroclinic life cycles and falls within the 'medium-range' time scale of operational forecasting (about 6–10 days). It should be noted that realistic forecast errors are unlikely to remain linear over this time scale, so direct application of the results of this section to forecasting problems must be made with care. Nevertheless, this time scale remains interesting from the point of view of the general theory of linear disturbance growth. The 'short-range' case of $\tau = T_w$, over which forecast errors are likely evolve linearly, is discussed in section 4.4.2.3.

For the present section, the numerical ranking of the SVs is based on the ranking of the corresponding singular values the largest initialization time considered ($t_0 = T$). Thus, $\boldsymbol{\xi}_1$ is the leading SV at time $t_0 = T$, but since the SVs exchange stability as the initialization time changes, $\boldsymbol{\xi}_1$ may not be the leading SV for $t_0 < T$.

The SVs again divide into the WD and DA classes. The WD singular values show large (factor of 10) oscillations on the time scales of the basic cycle. The WE singular values lag slightly behind the basic cycle (Fig. 4.8) as do the PV singular values (not shown), while the singular values in SA inner product oscillate in phase with the basic cycle. The singular value structure is qualitatively similar for all three inner products. Quantitatively, the maximum growth factors for the WE and PV inner products are similar (21 and 35, respectively), while the maximum growth possible in the SA inner product is 5 times larger than for the PV inner product. While the most rapidly growing SV varies with initialization interval, the five most rapidly growing SVs always have singular values greater than unity. $\boldsymbol{\xi}_6$ sometimes grows and sometimes decays. This basic result holds in the all three inner products.

As with the fixed initialization time calculations, the leading SVs have significant contributions from a large number of FVs (not shown). In addition, the Floquet

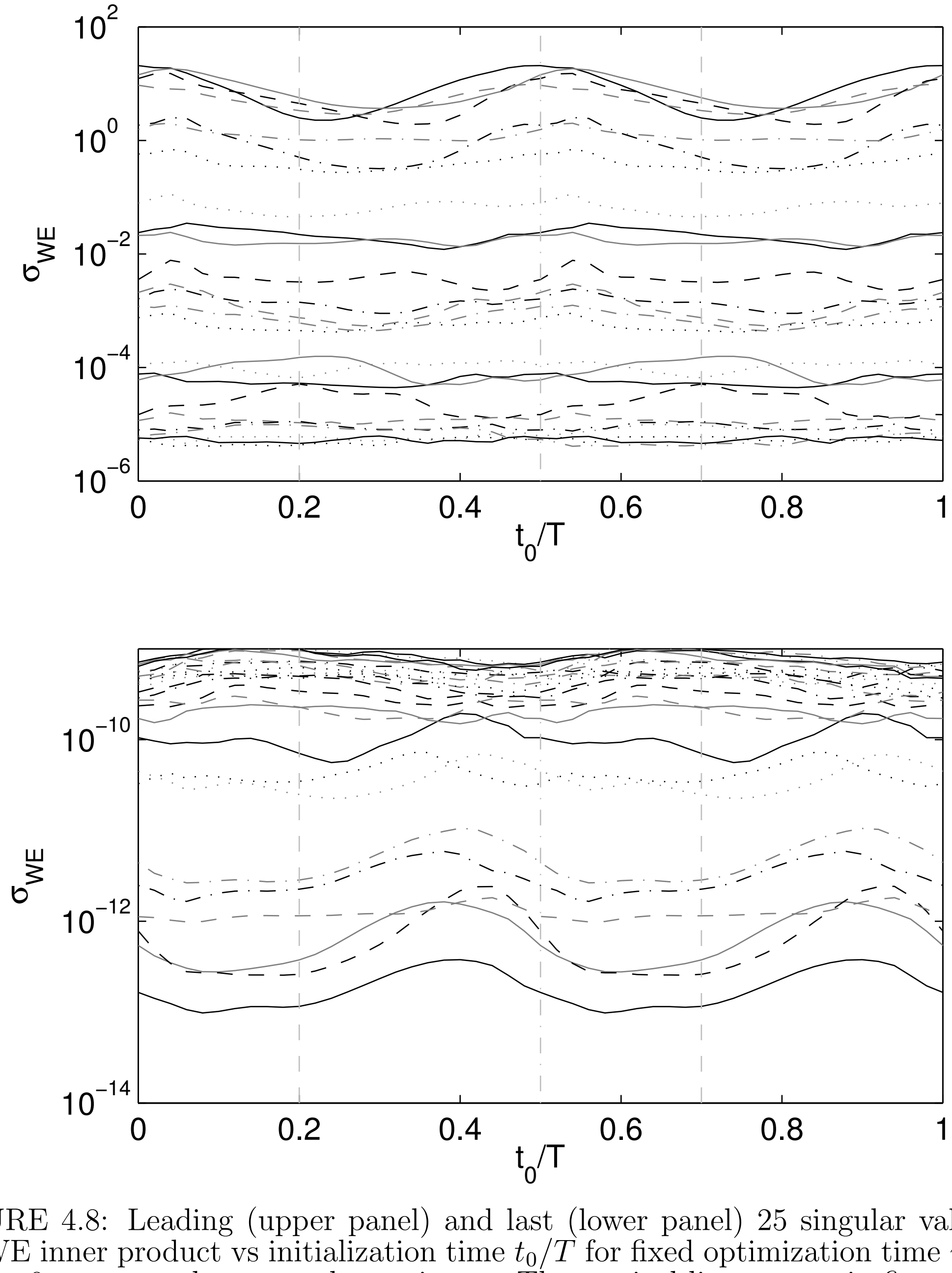

FIGURE 4.8: Leading (upper panel) and last (lower panel) 25 singular values in the WE inner product vs initialization time t_0/T for fixed optimization time $\tau = T$. $t_0/T = 0$ corresponds to a cycle maximum. The vertical lines are as in figure 4.2.

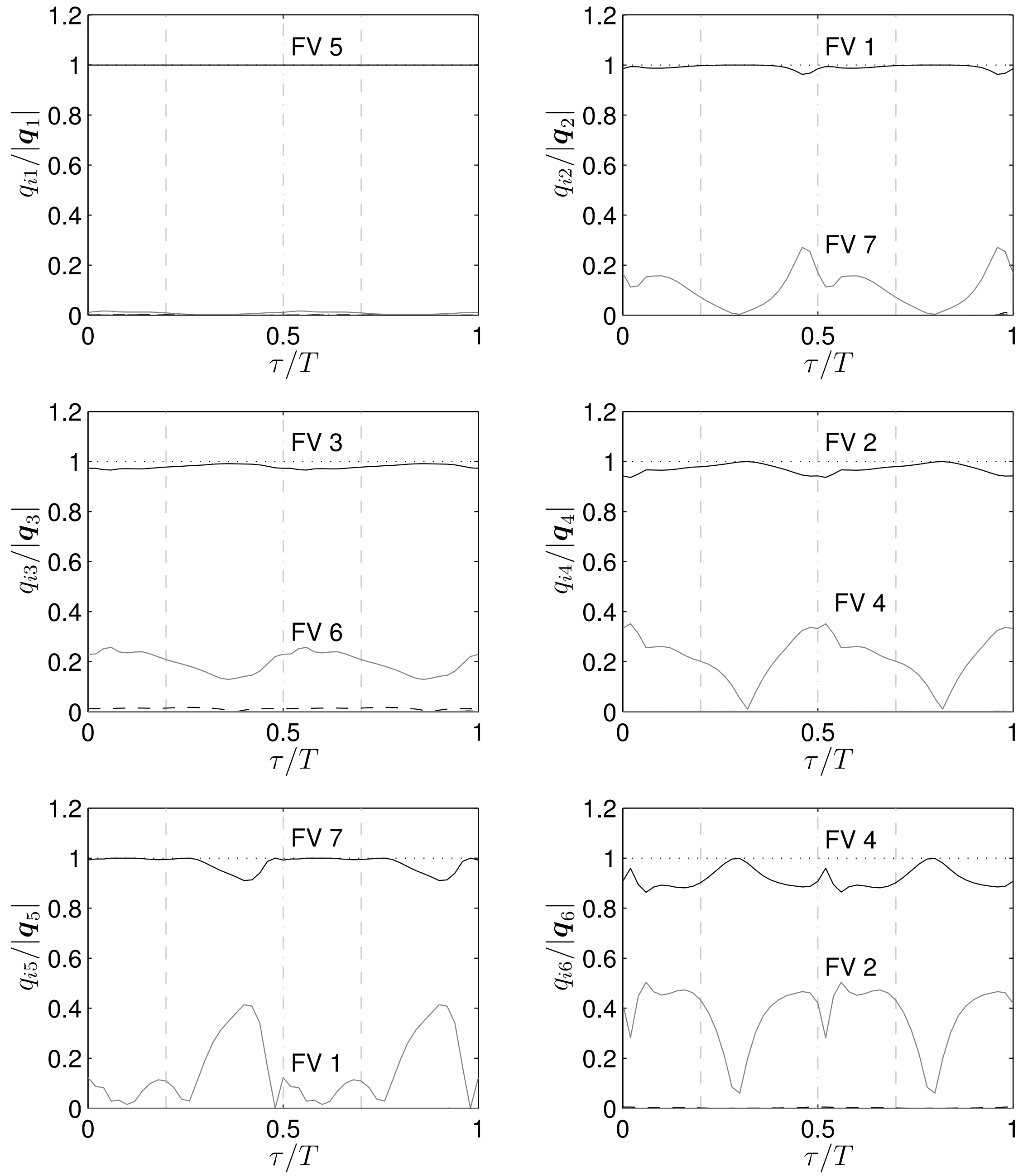

FIGURE 4.9: Magnitude of the largest 100 FV adjoint components $\boldsymbol{q}_j$ of the leading SVs in the WE inner product vs initialization time t_0/T for fixed optimization interval $\tau = T$. The vertical lines are as in figure 4.2.

decompositions are strong functions of time, showing significant oscillations on the time scale of the basic cycle. By contrast, the leading SVs are relatively simple functions of a small number of the adjoint FVs (Fig. 4.9). In fact, for each initialization time, the leading five SVs are nearly optimal excitations of *same* FVs. Both $\boldsymbol{\xi}_2$ and $\boldsymbol{\xi}_5$ (resp. $\boldsymbol{\xi}_4$ and $\boldsymbol{\xi}_6$) have large projections onto $\boldsymbol{\theta}_1$ and $\boldsymbol{\theta}_7$ (resp. $\boldsymbol{\theta}_2$ and $\boldsymbol{\theta}_4$), but the roles of the adjoint FVs are reversed. As in the previous sections, this occurs because $\boldsymbol{\theta}_1$ and $\boldsymbol{\theta}_7$ (resp. $\boldsymbol{\theta}_2$ and $\boldsymbol{\theta}_4$) are orthogonal, in all three inner products, to all of the leading adjoint FVs except each other.

The most rapidly decaying SVs also project onto the same FVs, regardless of initialization time (Fig. 4.10). $\boldsymbol{\xi}_{3836}$ and $\boldsymbol{\xi}_{3838}$ project strongly onto the same FVs, but with their roles exchanged.

Despite the qualitative similarity of the singular values and Floquet decompositions of SVs calculated in the three inner products, the temporal evolution of their spatial scales is remarkable different. The leading SVs in the SA inner product are dominated by very small structures at the initialization time, but systematically evolve toward larger scales by the optimization time (Fig. 4.11a), where scale is measured by the mean wavenumber $\overline{K}$, defined by

$$\overline{K}^2 = \frac{\int |\nabla\psi_1|^2 + |\nabla\psi_2|^2 \; d\boldsymbol{x}}{\int \psi_1^2 + \psi_2^2 \, d\boldsymbol{x}}. \tag{4.18}$$

The leading WE SVs show similar behavior, but the initial SVs are larger scale and the up-scale evolution is significantly weaker (Fig. 4.11c, see also figs. 4.5 & 4.14). The PV SVs, by contrast, are nearly channel scale (the largest possible wave has $\overline{K} = \pi$) at both the initialization and optimization times and evolve toward slightly smaller scales (Fig. 4.11e). In all three cases, the most rapidly decaying SVs show evolution in the opposite sense as the leading SVs (Fig. 4.11b, d & f, see also

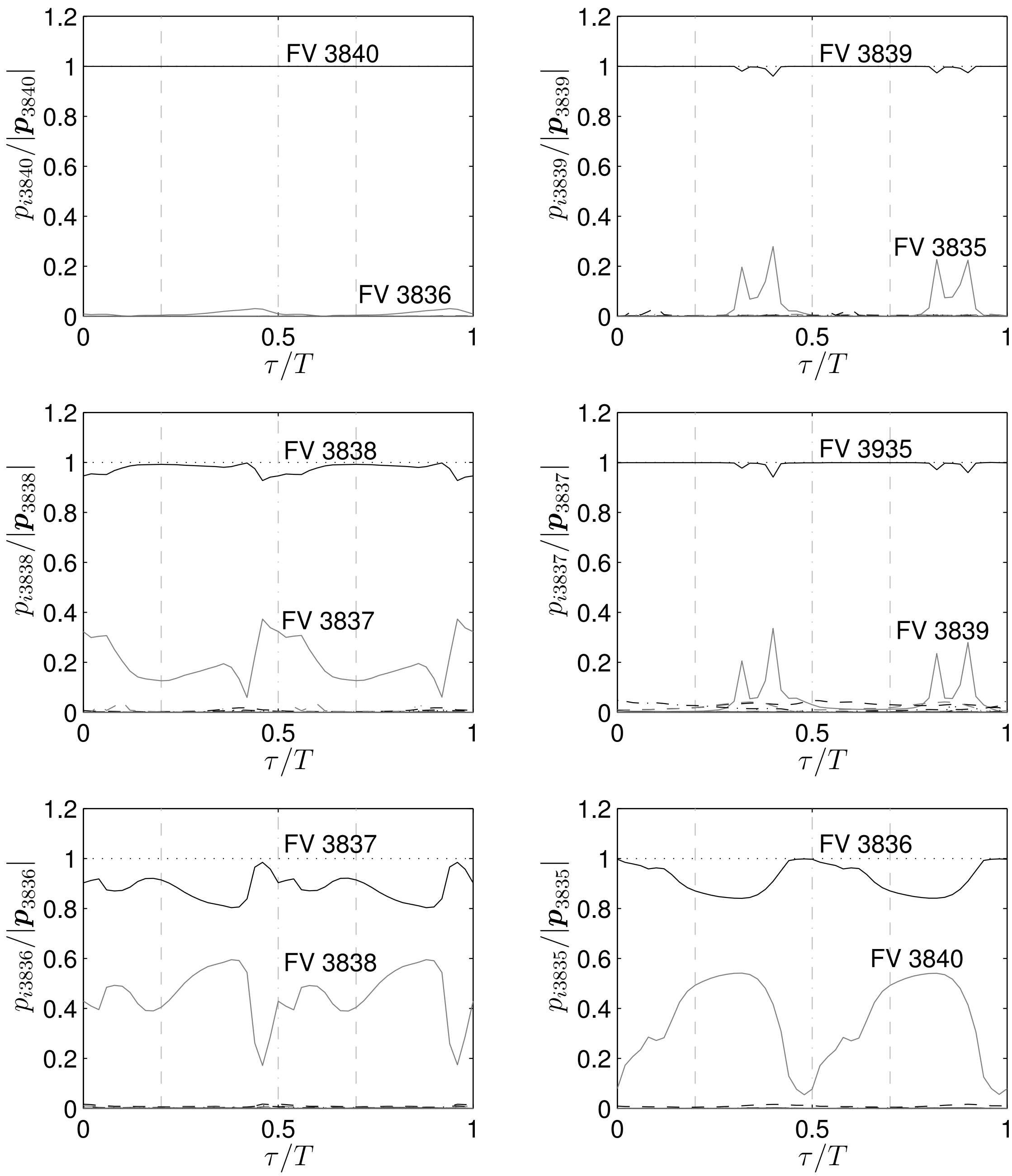

FIGURE 4.10: As with figure 4.9, but for the most rapidly decaying SVs.

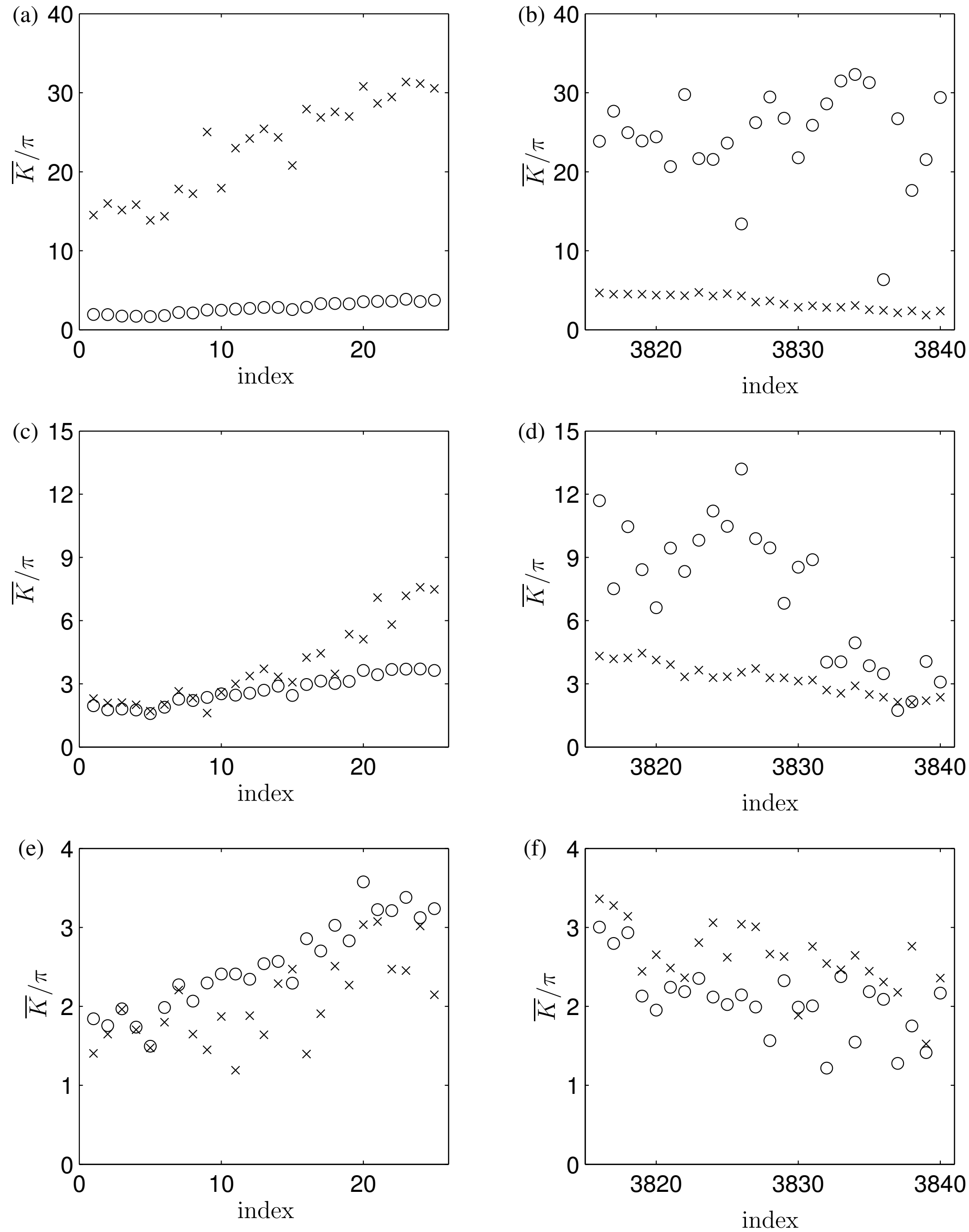

FIGURE 4.11: Scales, as measured by mean wavenumber $\overline{K}$, of the leading and trailing SVs at the initialization (crosses) and optimization (circles) times for SVs calculated using the SA (a,b), WE (c,d), and PV (e,f) inner products. The optimization interval $\tau = T$ and the results are averaged over all possible initialization times.

fig. 4.7).

4.4.2.3 Fixed optimization interval $\tau = T_w$

As mentioned in the previous section, $\tau = T$ is a relatively long lead time for operational forecasts and realistic forecast errors are unlikely to evolve linearly over this time interval. However, error growth is expected to remain linear over the 'short-range' forecasting time scale, encompasing approximately one baroclinic growth time scale T_w. The impact of varying initialization time is thus examined for the case of the optimization interval fixed at $\tau = T_w$.

Remarkably, the SVs with $\tau = T_w$ do not have significantly lower growth factors than those with $\tau = T$ (Fig. 4.12). This is consistent with the observation that most of the super-Lyapunov growth in the singular values occurs for $\tau \leq T_w$, after which the growth rate of the singular values closely matches that of the FVs (Fig. 4.1). As with the case $\tau = T$, the WD singular values oscillate on the time scale of the basic cycle growth and decay phases, but in the present case the oscillations lead the basic cycle by approximately 90°. Thus, disturbances made at the beginning of the basic cycle growth phase have the greatest capacity for growth over the interval $\tau = T_w$ because they evolve *with* the growth of the basic cycle. Conversely, disturbances made at the beginning of the basic cycle decay phase have a poor capacity for growth because they evolve *against* the decay of the basic cycle. An alternative viewpoint is that small changes to the background flow made at the beginning of the basic cycle growth (resp. decay) phase evolve into small changes *relative to the background flow* by the basic cycle maximum (resp. minimum), but since the amplitude of the basic cycle has significantly increased (resp. decreased) the small changes correspond to disturbances of increased (resp. decreased) amplitude.

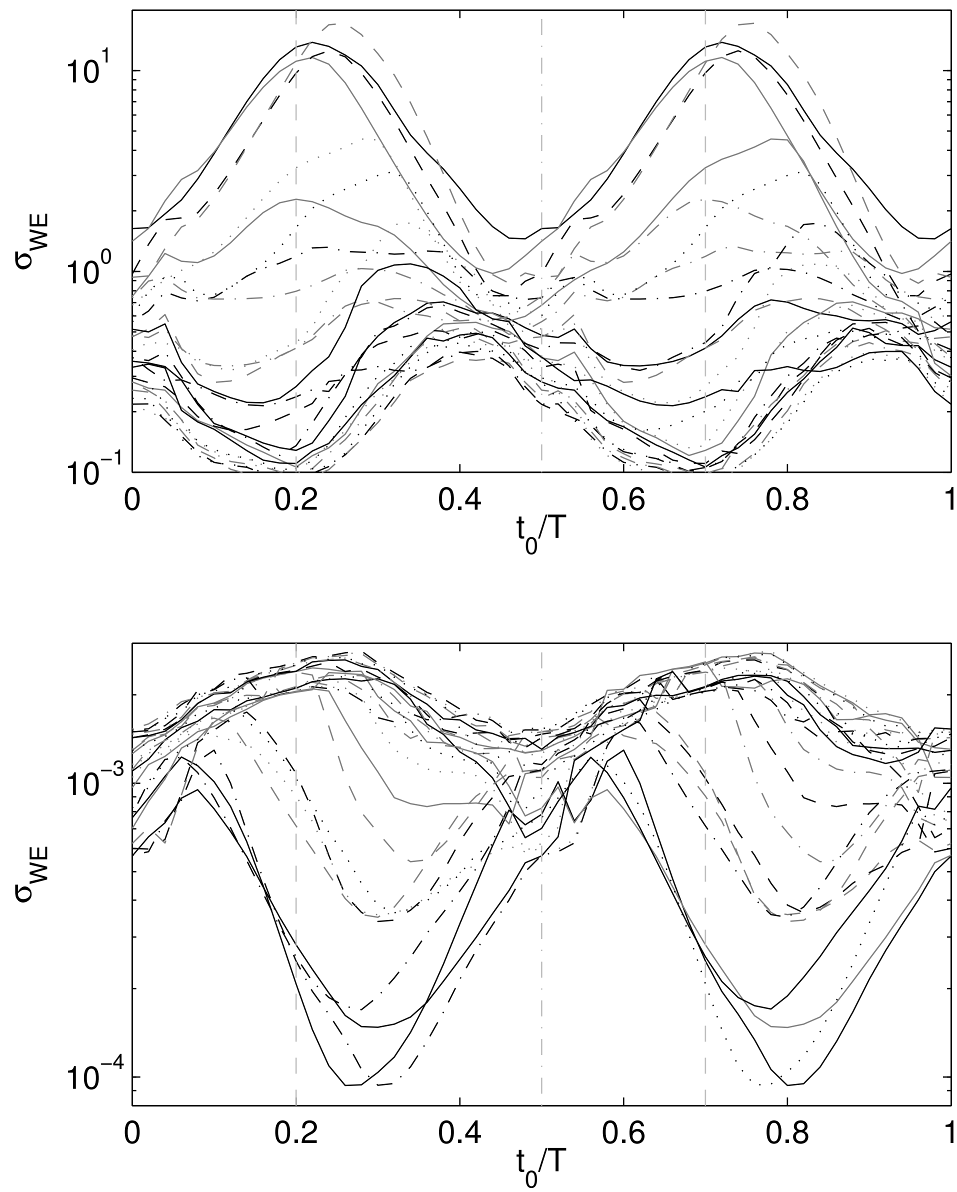

FIGURE 4.12: Leading (upper panel) and last (lower panel) 25 singular values in the WE inner product vs initialization time t_0/T for fixed optimization time $\tau = T_w$. $t_0/T = 0$ corresponds to a cycle maximum. The vertical lines are as in figure 4.2.

The less dominant singular values exhibit progressively smaller oscillations and decreased lead times compared to the leading singular values, most likely due the increased contribution of decaying FVs to the corresponding SVs. These SVs thus have less time in which to grow with the basic cycle before the asymptotic decay of the FVs begins to dominate. (This also occurs for $\tau = T$, but the effect is too small to be seen in figure 4.8.)

The modal structure of the SVs with $\tau = T_w$ is not as clear as those at longer optimization intervals. The Floquet decompositions of both the leading and rapidly damped SVs have a large number of components of roughly equal magnitude which are complicated functions of initialization time. However, the leading SVs are still relatively simple functions of a few adjoint FVs (Fig. 4.13), although a larger number of adjoint FVs have significant magnitude than at $\tau = T$. The simplicity of the adjoint representation is reflected in the physical structures of the SVs as well, which resemble the leading FVs at the optimization time t_1 (Fig. 4.14). Note that figure 4.14 shows $\boldsymbol{\xi}_4$ which, due to differences in ranking, is the same as $\boldsymbol{\xi}_1$ shown in figure 4.5c & d for $t_0 = 0$.

The chevron-shaped structures (see Fig. 4.5) are present in the initial SVs when the basic flow is predominately zonal. As the basic cycle evolves the flow becomes increasingly non-zonal and the chevron structures become difficult to discern, completely disappearing for initialization times $0.2T \leq t_0 \leq 0.3T$. Further, at these times the scale of the basic flow nearly matches the scale of the singular vectors. The chevron shapes are predicted from a WKBJ analysis which requires the flow to vary slowly on the scale of the disturbances (Zeng, 1983; Buizza and Palmer, 1995), so it is not surprising that they should disappear precisely when the basic flow violates the WKBJ assumptions. During these times, the initial SV disturbances are

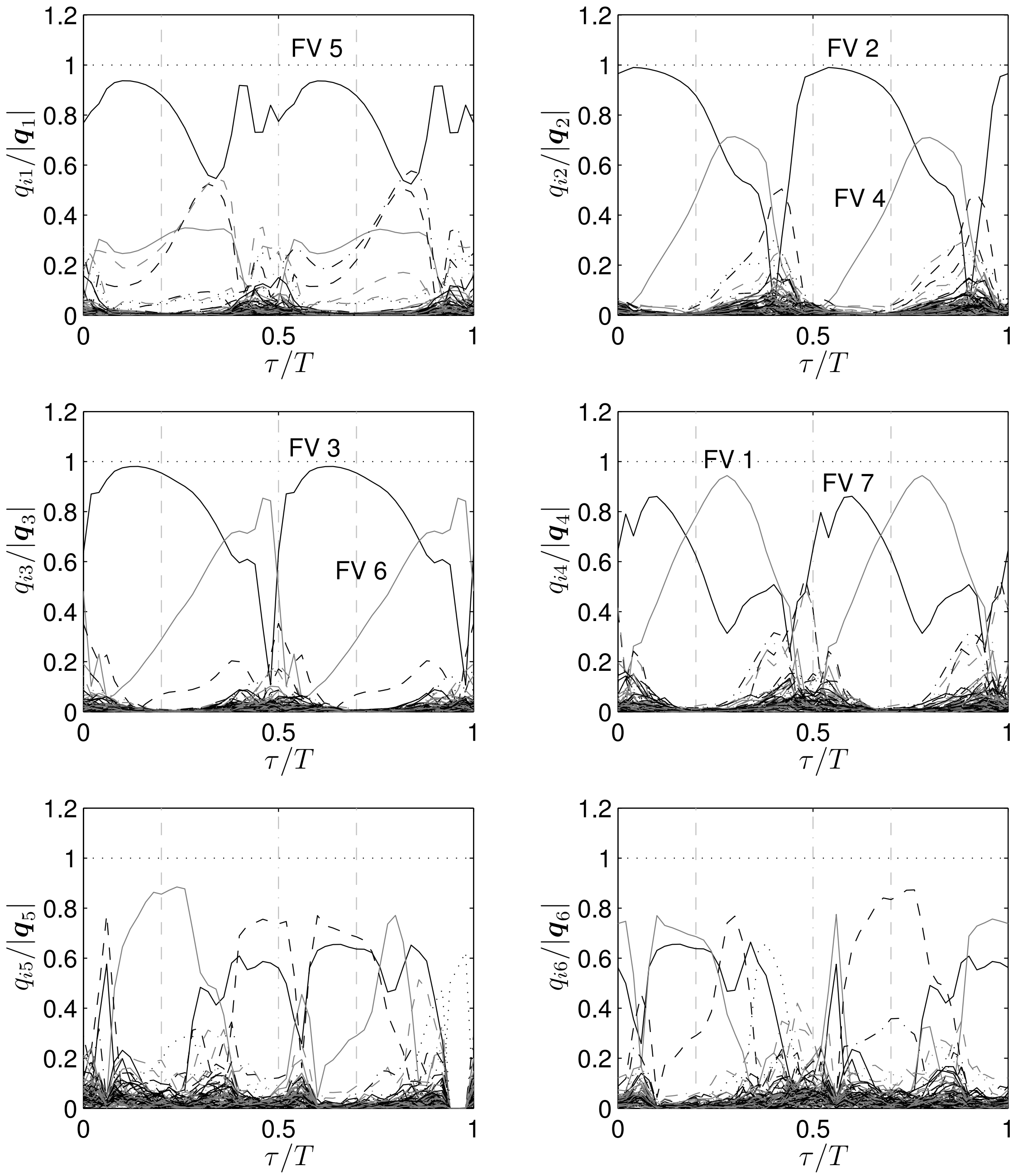

FIGURE 4.13: Magnitude of the largest 100 adjoint FV components $\boldsymbol{q}_j$ of the leading SVs in the WE inner product vs initialization time t_0/T for fixed optimization interval $\tau = T_w$. The vertical lines are as in figure 4.2.

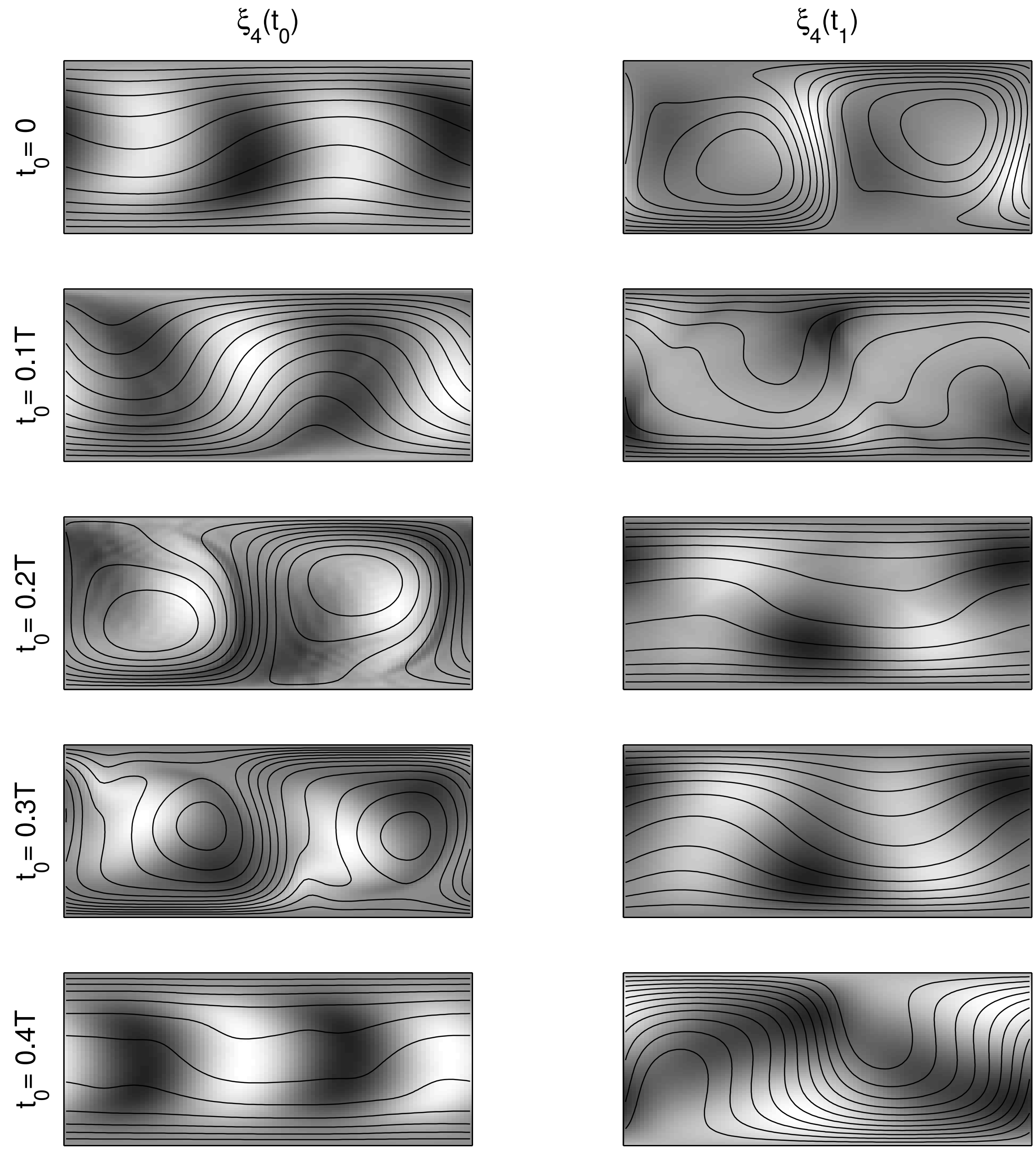

FIGURE 4.14: The initial $\boldsymbol{\xi}_4(t_0)$ (left panels) and final $\boldsymbol{\xi}_4(t_1)$ (right panels) upper layer streamfunction of the fourth WE SV (colors) with $\tau = T_w$ at five initialization times t_0. Also shown is the upper level streamfunction of the basic cycle (contours). Since the SVs are linear disturbances, the color scale is arbitrary.

located near where the basic flow undergoes rapid changes in direction. These areas are regions of high strain which are conducive to rapid disturbance growth through barotropic processes (Moore and Mariano, 1999). This growth mechanism is sufficiently effective that the leading SVs obtain their largest growth during these times (Fig. 4.12).

Despite the complexity of their Floquet decomposition, the initial conditions of the most rapidly decaying SVs (not shown) maintain a strong visual resemblance to the most rapidly decaying FVs. The final conditions of these SVs, on the other hand, are dominated by filamented and patchy structures similar to those seen in figure 4.7.

4.5 Relationship to the local attractor structure

If model used for ensemble forecasting is a faithful representation of the true dynamics of the atmosphere, the attractor of the model should resemble the attractor of the atmosphere. In that case, errors in the forecast should primarily be errors of placement within the attractor. For lead times sufficiently short that disturbance dynamics are linear (2–3 days in the atmosphere), the initialization error should then lie in the unstable tangent linear space of the attractor. Thus, a common argument against using SVs in ensemble forecasting schemes is that the SV initial conditions point off (i.e., they are not geometrically tangent to) the attractor and that much of their growth is due to rapid rotation of the disturbances back onto the attractor (e.g., Kalnay, 2003, §6.3). The growing Lyapunov vectors (the aperiodic analog of FVs), on the other hand, determine local unstable tangent linear space which, since attractors are unions of unstable manifolds, determines the geometric

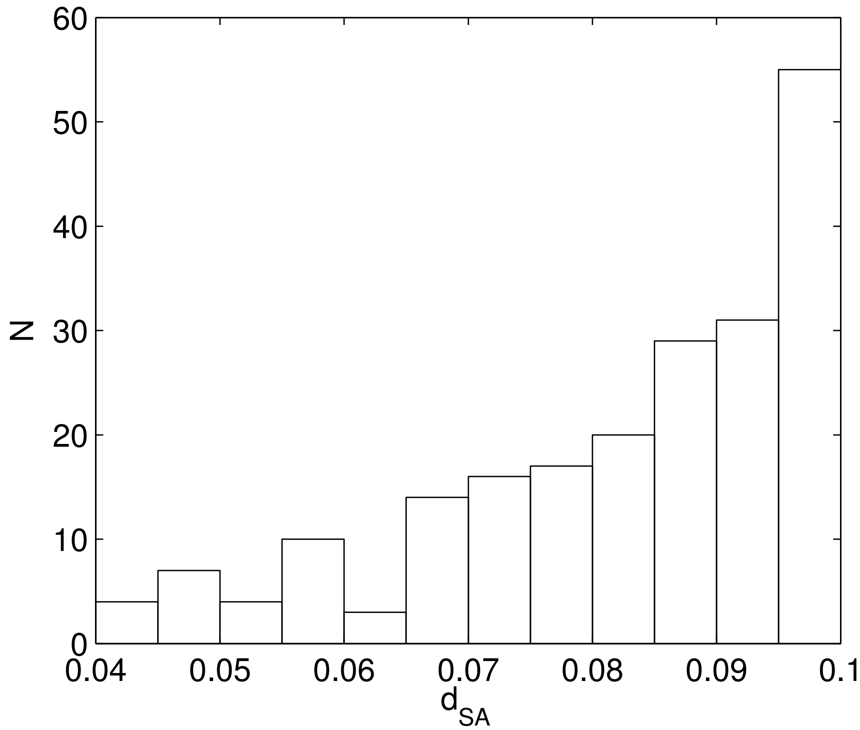

FIGURE 4.15: Histograms of the relative distance in the SA norm d_{SA} from the basic cycle $\mathbf{P}_b$ to the Poincaré intersections $\mathbf{P}_n$ based on 120 000 Poincaré intersections. The total number of intersections with $d_{\mathrm{SA}} \leq 0.1$ is 210. There were no intersections with $d_{\mathrm{SA}} < 0.04$.

tangent of the local attractor.

These statements can be examined in a quantitative manner in the present context, both with regard to the unstable cycle and to the more complex chaotic attractor itself. The leading FVs define the local unstable tangent space to the basic cycle and it is clear from results of section 4.4 that the leading SVs do not project strongly into the subspace of the leading FVs, but instead have strong projections onto the *adjoint* FVs. Thus, the leading SVs point 'off' the basic cycle and much of their initial growth comes from rapid rotation into the unstable subspace defined by the leading FVs.

It is of interest to determine if these results generalize to the attractor at large. We focus on trajectories within the attractor which are near the basic cycle in following sense: Let the state vector formed by the basic cycle at the first cycle maximum be denoted by $\mathbf{P}_b$ and define a Poincaré section by the hyperplane passing through $\mathbf{P}_b$ with normal equal to the tangent to the basic cycle $\partial_t \mathbf{P}_b$. Define $\Delta\mathbf{P}_j \equiv \mathbf{P}_j - \mathbf{P}_b$ as the difference between the Poincaré intersections and the basic cycle. The Poincaré intersections $\mathbf{P}_j$ with relative distance to $\mathbf{P}_b$

$$d_{\mathrm{SA}} \equiv \frac{\|\Delta\mathbf{P}_j\|_{\mathrm{SA}}}{\|\mathbf{P}_b\|_{\mathrm{SA}}} \leq 0.1, \tag{4.19}$$

where $\|\cdot\|_{\mathrm{SA}}$ is the norm induced by the SA inner product, are considered to be 'near' the basic cycle. Out of 120 000 Poincaré intersections, generated from a long integration on the attractor, 210 near approaches to the basic cycle satisfying (4.19) were found (Fig. 4.15). Since the attractor of the present system is a fairly high dimensional object (Kaplan-Yorke dimension ≈ 7), any low period orbit represents only a part of the attractor, and this small number of returns is not a surprise. The 210 returns are sufficient to furnish a useful description of the local structure of the attractor. Note that these and the following calculations were performed using a reduced resolution of 24×22 for computational expediency.

The extent to which the leading FVs describe the variability of nearby trajectories can be quantified by attempting to expand $\Delta\mathbf{P}_j$ in an orthonormalization of the leading n FVs $\hat{\boldsymbol{\phi}}$:

$$\Delta\mathbf{P}_j = \sum_{i=1}^{n} \langle \hat{\boldsymbol{\phi}}_i, \Delta\mathbf{P}_j \rangle_{\mathrm{SA}} \hat{\boldsymbol{\phi}}_i + \boldsymbol{\rho}_j^{(n)}, \tag{4.20}$$

where $\boldsymbol{\rho}_j^{(n)}$ is the residual after expanding $\Delta\mathbf{P}_j$ in the first n FVs. The relative

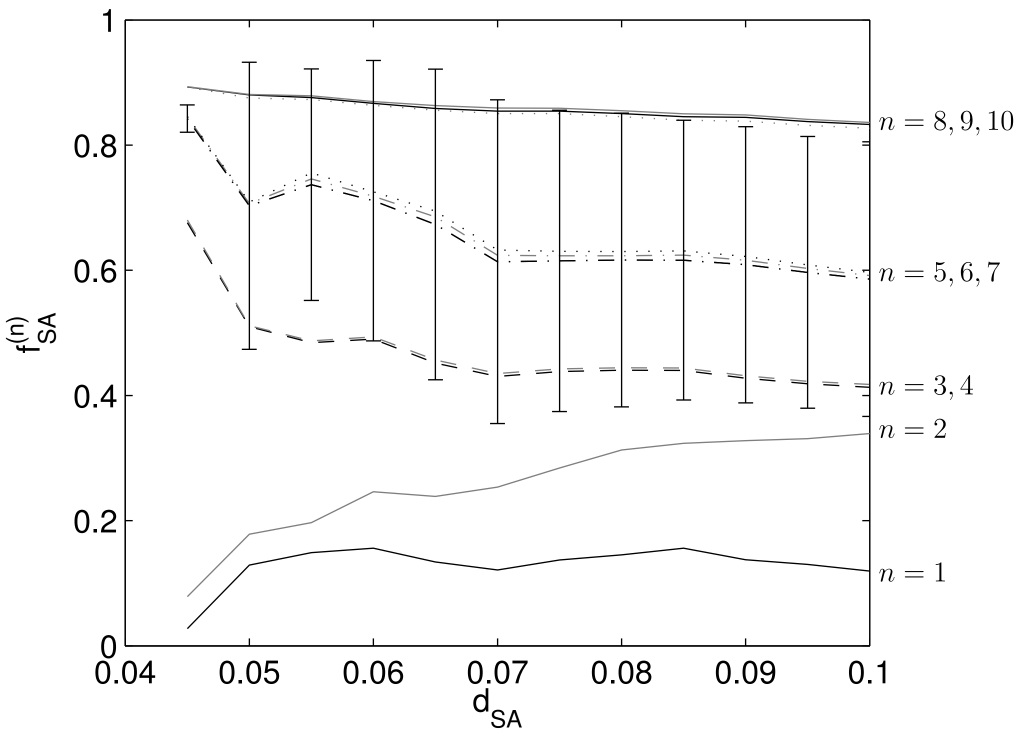

FIGURE 4.16: Fraction of the local variance of $\mathbf{P}_n$ explained by the leading FVs in the SA norm $f_{\mathrm{SA}}^{(n)}$ ordered by the relative distance to the basic cycle d_{SA}. Lines give bin averages of f_{SA} and errorbars (plotted on the $n = 5$ line) give bin standard deviations. The bin size is 0.005. The number of FVs n used to construct the leading subspace increases vertically, starting with $n = 1$ and ending with $n = 10$.

magnitude of the $\boldsymbol{\rho}_j^{(n)}$,

$$f_{\mathrm{SA},j}^{(n)} = \frac{\|\boldsymbol{\rho}_j^{(n)}\|_{\mathrm{SA}}}{\|\Delta\mathbf{P}_j\|_{\mathrm{SA}}}, \tag{4.21}$$

gives the fraction of the variance of nearby Poincaré intersections explained by the leading n FVs. It is found that the leading 10 FVs explain approximately 90% of the local variance of $\Delta\mathbf{P}_j$, although there is significant point-to-point variability (Fig. 4.16). The leading FVs thus point 'onto' the local attractor. Note that very little improvement results from adding the fourth FV $\boldsymbol{\phi}_4$. This FV is the neutral mode proportional to $\partial_t\mathbf{P}_b$, which defines the normal to the Poincaré section. The $\Delta\mathbf{P}_j$ are thus orthogonal to $\boldsymbol{\phi}_4$ by construction.

The fraction of the local variability on the Poincaré section explained by the leading SVs may be similarly assessed by expanding $\Delta\mathbf{P}_j$ in terms of the leading SVs. The details of the calculation are unchanged, except that the inner product use to calculate the SVs was also used to calculate the inner product in (4.20) and to assess the magnitude of the residual. The initial conditions of the leading SVs do a poor job of describing the local variation on the Poincaré section, with little more than 10% of the variance captured by the WE and PV SVs and only about 2% captured by the SA SVs (Fig 4.17, left panels). The SV final conditions, on the other hand, capture as much of the variance as the FVs (Fig 4.17, right panels). The leading SV initial conditions thus point 'off' the local attractor, but rotate into the attractor by the optimization time.

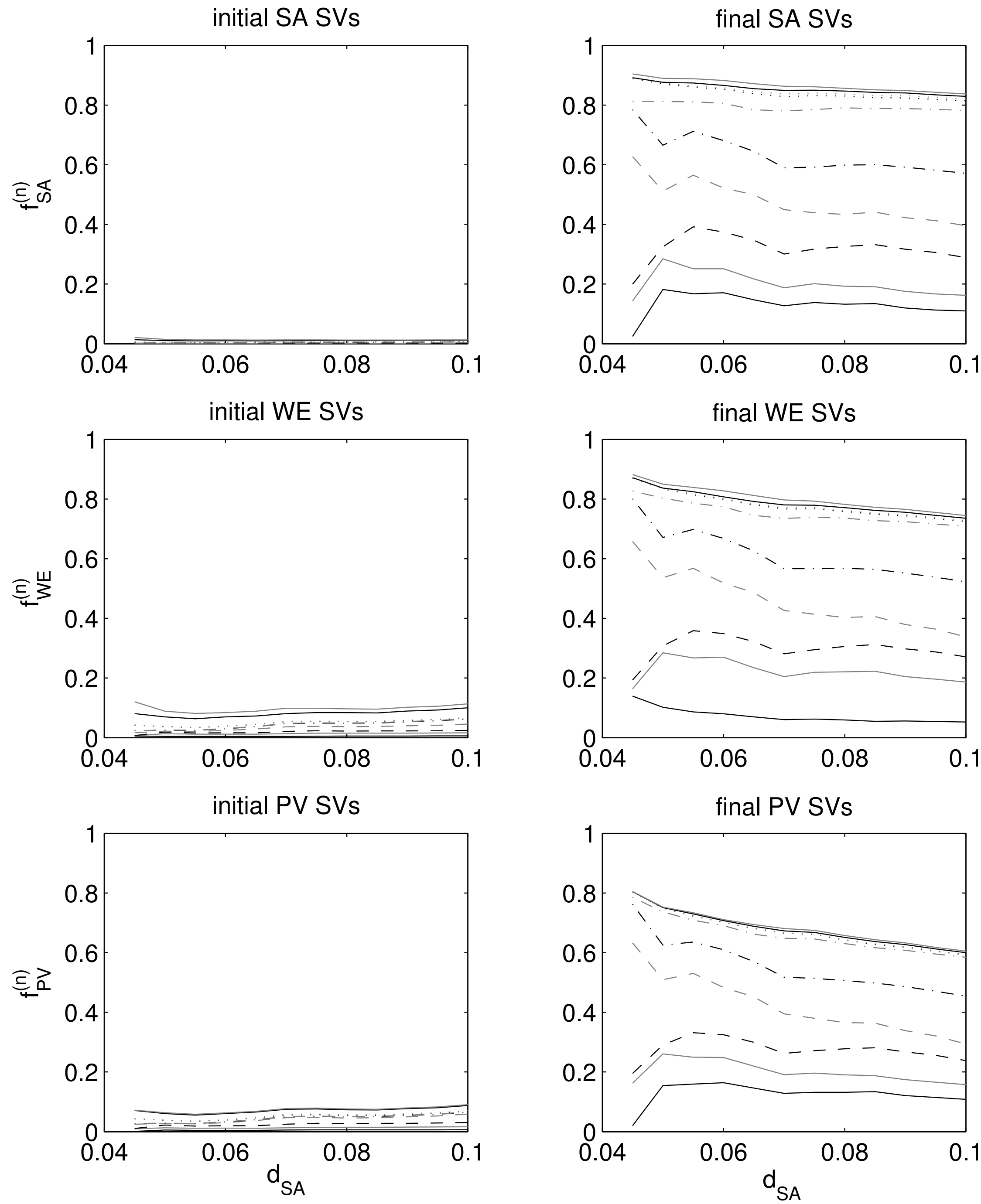

FIGURE 4.17: Fraction of the local variance of $\mathbf{P}_n$ explained by the leading SVs in the SA, WE and PV norms f_{SA}, f_{WE}, and f_{PV}, respectively, ordered by the relative distance to the basic cycle d_{SA}. Lines give averages of f over bins of size 0.005. The number of SVs n used to construct the leading subspace increases vertically, starting with $n = 1$ and ending with $n = 10$.

4.6 Recovering Floquet vectors from singular vectors

4.6.1 Formulation

The case under present consideration is unusual in studies of linear disturbance growth, since the norm-independent quantities characterizing asymptotic disturbance growth (i.e., Floquet/Lyapunov vectors) are known a priori and are used to calculate the SVs. In most situations, a subset of the SVs are calculated directly while the Lyapunov vectors may be difficult to obtain. Wolfe and Samelson (2006b) have presented an efficient method for constructing the extremal n Lyapunov vectors using just $2n$ SVs and demonstrated the effectiveness of this method using two low-dimensional numerical examples. It is of interest to determine whether the method remains effective when applied to a more complex model with thousands or millions of variables. The present model, with 3840 variables, provides an ideal system with which to begin answering this question. Furthermore, since the Floquet vectors are already known, they may used to check the calculations. For a detailed discussion and justification of the method for recovering Floquet vectors from SVs, see Wolfe and Samelson (2006b). A brief recapitulation is given here for completeness.

Fix a time t. Under fairly general conditions, SVs converge exponentially as $\tau \to \infty$ to constant linear combinations of the Lyapunov (here, Floquet) vectors such that

$$\mathbf{F}(t) = \mathbf{A}\mathbf{X}, \tag{4.22}$$

$$\mathbf{F}(t) = \mathbf{B}\mathbf{Y}, \tag{4.23}$$

where $\mathbf{X}$ is a matrix whose columns are the initial conditions $\hat{\boldsymbol{\xi}}$ of SVs initialized at time t, $\mathbf{Y}$ is a matrix whose columns are the final conditions $\hat{\boldsymbol{\eta}}$ of SVs optimized at time t, $\mathbf{F}$ is as in sections 4.3 & 4.4, and $\mathbf{A}$ and $\mathbf{B}$ are upper and lower triangular, respectively. The time dependence of $\mathbf{X}$, $\mathbf{Y}$, $\mathbf{A}$, and $\mathbf{B}$ has been suppressed for clarity. The convergence rate of the n^{th} SV is given by the difference between the real parts of the n^{th} Floquet exponent and the nearest Floquet exponent associated with a non-orthogonal FV. If the Floquet spectrum is degenerate, the SVs associated with the multiple Floquet exponents will not exhibit exponential convergence to constant vectors and may not converge at all. Note that complex conjugate Floquet exponents are considered degenerate according to this definition.

The representations (4.22) & (4.23) and the method of Wolfe and Samelson (2006b) allow the first n FVs to be recovered from $2n$ asymptotic SVs by finding the non-trivial solution to

$$\mathbf{D}^{(n)}\boldsymbol{y}^{(n)} = 0, \tag{4.24}$$

where

$$y_k^{(n)} = \langle \hat{\boldsymbol{\eta}}_k, \boldsymbol{\phi}_n \rangle \qquad k = 1, 2, \ldots, n, \tag{4.25}$$

$$D_{kj}^{(n)} = \sum_{i=1}^{n-1} \langle \hat{\boldsymbol{\eta}}_k, \hat{\boldsymbol{\xi}}_i \rangle \langle \hat{\boldsymbol{\xi}}_i, \hat{\boldsymbol{\eta}}_j \rangle \qquad k, j \leq n. \tag{4.26}$$

The last n FVs may be obtained in a similar manner by finding the non-trivial solution to

$$\mathbf{C}^{(n)}\boldsymbol{x}^{(n)} = 0, \tag{4.27}$$

where

$$x_k^{(n)} = \langle \hat{\boldsymbol{\xi}}_{k+n-1}, \boldsymbol{\phi}_n \rangle \qquad k = 1, 2, \ldots, N-n+1, \tag{4.28}$$

$$C_{ki}^{(n)} = \sum_{j=n+1}^{N} \langle \hat{\boldsymbol{\xi}}_{k+n-1}, \hat{\boldsymbol{\eta}}_j \rangle \langle \hat{\boldsymbol{\eta}}_j, \hat{\boldsymbol{\xi}}_{i+n-1} \rangle \qquad k, i \leq N-n+1, \tag{4.29}$$

4.6.2 Results

The Floquet spectrum shows that a large number (~ 3000) exponents cluster near the dissipation rate (WS), and, thus, the associated SVs are expected converge very slowly to their asymptotic forms. Further, unlike the examples in Wolfe and Samelson (2006b), the Floquet spectrum contains a large number of exponents which form complex conjugate pairs, so that the associate Lyapunov spectrum is, in fact, degenerate. There is no formal reason to expect that the SVs associated with degenerate Lyapunov exponents will assume an asymptotic form for any finite optimization interval. Fortunately, the Floquet exponents on the extreme upper and lower ends of the spectrum are distinct and well separated, with the exception of the two neutral modes for which $\lambda_4 = \lambda_5 = 0$. The two neutral modes are, however, orthogonal in the inner products used here, so the degeneracy of the Floquet exponents does not effect the convergence of the associated SVs.

The first and last ten SVs were calculated in the PV inner product for a fixed set of optimization intervals, with the longest interval $\tau = 3T$. The order of magnitude of the convergence times is correct (Fig. 4.18), but they do not agree with the expected convergence time to the same degree as with the low-order examples of Wolfe and Samelson (2006b). Some of the discrepancy may be due to the fact that—in contrast with the previous study—the present model is sufficiently computationally burdensome that the optimization interval was not systematically increased until convergence within a specified tolerance was observed. Thus, for some of the SVs, there may not be sufficient data to accurately estimate the observed convergence rate.

The FVs $\hat{\boldsymbol{\phi}}$ recovered from the asymptotic SVs compare well with the FVs calculated directly from the one-period propagator $\boldsymbol{\phi}$ (Fig. 4.19). This agreement

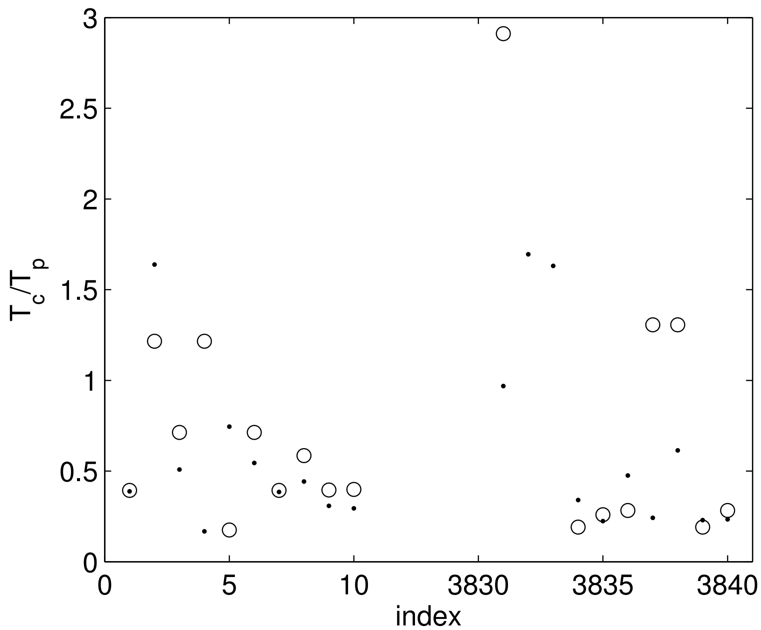

FIGURE 4.18: SV convergence e-folding time T_c relative to the period of the baroclinic wave-mean oscillation T. Circles give the expected convergence time based on the Floquet exponents, dots give the average convergence time (based on an exponential fit). The asymptotic forms were only calculated for the first and last ten SVs. For SVs 3832 & 3833, T_c is infinite.

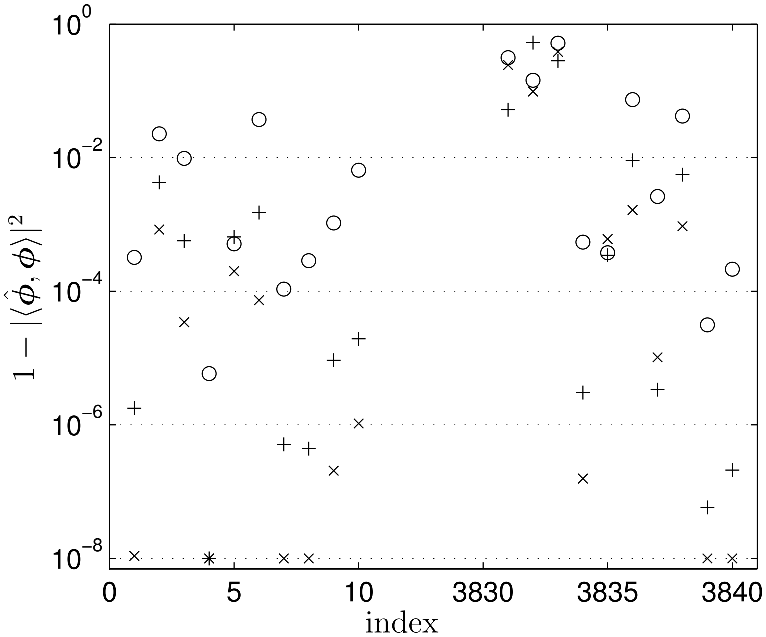

FIGURE 4.19: One minus the pattern correlation between the recovered FVs $\hat{\boldsymbol{\phi}}$ and the true FVs $\boldsymbol{\phi}$ for optimization intervals of T (crosses), $2T$ (pluses), and $3T$ (circles), where T is the period of the basic wave-mean oscillation. A value of unity indicates orthogonality while a value of zero indicates collinearity. Pattern correlations for which $1 - |\langle \hat{\boldsymbol{\phi}}, \boldsymbol{\phi} \rangle|^2 < 10^{-8}$ are plotted at 10^{-8} to show the upper values more clearly.

demonstrates that the efficient method of Wolfe and Samelson (2006b) can be used successfully to computer Lyapunov vectors from SVs in a model with several thousand degrees of freedom and multiple unstable modes. Curiously, while the leading ten recovered FVs show a systematic improvement in accuracy as the optimization interval is increased, a number of the trailing FVs do not. This may be due to the fact the trailing FVs decay so rapidly (by more than 10^{-37} after three periods) that the numerical stability of the tangent linear integration and eigenvalue calculation are compromised for long optimization intervals.

4.7 Discussion

A significant advantage of the present calculations is that they allow the connection between normal mode disturbances (Floquet vectors) and optimal disturbances (singular vectors) to be explicitly displayed. The leading singular vectors are non-modal disturbances: they have significant contributions from a large number of damped FVs (Fig. 4.3) and owe a significant portion of their initial growth to the rapid decay of the damped FVs. Further, as shown in section 4.5, the initial leading SVs point 'off' the local attractor. It appears (Figs. 4.6 & 4.10) that the most rapidly damped SVs are modal, or nearly so, but this an illusion. The largest components of the most rapidly damped SVs decay so quickly that, by the optimization time, the physical structure of these SVs will be dominated by less rapidly decaying FVs, no matter how small their initial projection onto the SVs. This view of the most rapidly decaying SVs is consistent with the down-scale evolution of these SVs (Fig. 4.11) which is due to the domination of the large-scale, but rapidly decaying, FVs by smaller scale, less rapidly decaying, FVs as the disturbance evolves.

The non-modal character of the optimal disturbances is due entirely to the non-orthogonality of the FVs, so it is worth examining the projections of the FVs onto each other in some detail. While the leading 10 WD modes have significant projections onto the DA modes—with pattern correlations greater than 0.75 in the SA inner product at certain times—the temporal structure is interesting: The leading WD modes are nearly orthogonal to the DA modes during the basic cycle growth phase, while baroclinic dynamics are most pronounced. In contrast, large projections of the WD modes onto the DA modes occur during the basic cycle decay phase, when the dynamics are primarily viscous and advective. This behavior is more complicated than studied by Samelson (2001b) where the relative orientations of the FVs were maintained throughout the cycle and advective dynamics were never dominant, allowing the WD modes to remain nearly orthogonal to the DA modes throughout the cycle. As the number of derivatives in the inner product increases, the leading WD modes become progressively more orthogonal to the DA modes. In the WE inner product, the maximum pattern correlation is 0.33, while it is less than 0.07 in the PV norm. This explains why the transient, super-Lyapunov growth is less apparent in the PV SV spectrum than in the WE and SA SV spectra. The most rapidly damped WD modes show more complicated behavior, with some modes projecting maximally onto the DA modes during the cycle decay phase, some modes during the growth phase, and some modes during both phases. Further, the pattern correlations are larger, with maximum PCs of at least 0.92, 0.61, and 0.39 in the SA, WE, and PV inner products, respectively.

Some of the apparent simplicity of the results discussed in section 4.4 may be the result of the fact that the WD modes are nearly mutually orthogonal, in the sense that a given WD mode has large projections on only a few other WD modes. For example, the first three unstable FVs form a mutually orthogonal set in all three inner products (to within numerical accuracy), as do the three most rapidly decaying FVs. This orthogonality may be a result of the simplified geometry and the dynamical constraints imposed by quasigeostrophy. Additionally, all of the unstable modes supported by this system are of a single class (predominately baroclinic) and evolve on similar time scales, whereas operational forecast models typically support multiple competing modes of instability which may have a wide range of time scales. Calculations similar to the present using less highly constrained models are likely to produce more complicated results.

The results of the present study are broadly consistent with those of Buizza and Palmer (1995) who identify a systematic evolution of leading kinetic energy SVs to larger scales, while PV SVs are dominated at initialization and optimization time by planetary-scale disturbances. In the present study, the both the leading SA and WE SVs show an evolution toward larger scales, with the scale change more significant for the SA SVs. The PV SVs are dominated by channel-scale disturbances at both the initialization and optimization times and actually evolve toward slightly smaller scales. For the SA and WE SVs, the evolution to larger scales occurs because the small scale components project strongly onto decaying FVs. The PV SVs project primarily onto the leading and most rapidly damped FVs, which have similar scales. The evolution of rapidly decaying SVs is essentially opposite to that of the leading SVs in all three inner products: the SA and WE SVs evolve toward smaller scales by the optimization while the PV SVs are similarly dominated by channel-scale disturbances. Further, the decaying SVs show either eastward or neutral phase shifts with height, in contrast to the leading SVs, which have westward phase shifts. Reynolds and Palmer (1998) observed a very similar relationship between the leading and decaying SVs in a simplified global forecast model with 1449 degrees of freedom.

In contrast to results found by Vannitsem and Nicolis (1997) for a 3-layer quasigeostrophic model, there does not appear to be a clear demarcation between the scales of the growing SVs (indices 1–5) and the weakly decaying SVs (indices 6–25). This is perhaps a reflection of the structure of the underlying FVs, where both the growing and weakly decaying FVs belong to the WD class and have very similar scales.

Szuntogh et al. (1997) notes that the choice of the optimization interval leads to little significant change in the SVs once the optimization interval exceeds about 72 hours, or roughly one baroclinic growth time scale. This is consistent with what we observe in the present system, where the SVs become approximately independent of optimization interval once $\tau \gtrsim T_w$. As pointed out in section 4.6, the exponential convergence of SVs to an asymptotic form independent of optimization interval is a generic property of SVs, even when the underlying flow is time-dependent.

The dynamical splitting observed in the present system is not as clear as that observed by Samelson (2001a,b) in a similar study of a weakly nonlinear model of the baroclinic instability. In that system, the dynamical splitting was so pronounced that the WD SVs projected strongly onto only the WD FVs. In that case, the primary transient growth mechanism for the leading SVs was interference between the inviscidly growing (leading) and inviscidly decaying (trailing) WD modes, which lead Samelson to conjecture that inviscidly damped modes might be important for understanding the dynamics of transient error growth. In the present, less constrained system, we find that while the PV SVs have large projections onto the trailing WD FVs, the SA and WE SVs do not. This is due to the fact that PV SVs are channel-scale disturbances and thus can only project strongly onto channel-scale WD FVs. The SA and WE SVs, on the other hand, have smaller scales and can project onto the small-scale DA modes. Thus, it appears that the importance of the inviscidly damped FVs to transient disturbance growth is norm-dependent. It should be noted, however, that all of the SVs have strong projections onto FVs (either DA or WD modes) which decay at or faster than the dissipation rate, implying that the calculation of SVs from a leading subspace of normal modes is likely to produce highly sub-optimal SVs.

An essential question regarding SVs and Lyapunov (here Floquet) vectors is their relative utility in ensemble forecasting schemes. As noted in section 4.5 and by other authors (e.g., Kalnay, 2003, §6.3 and references therein), the initial SVs point 'off' the attractor and thus represent 'unlikely' perturbations provided the forecast model is a reasonably good representation of the atmosphere. This may indicate that initial SVs are not a good choice for initial perturbations of ensemble members. On the other hand, the results of the present study seem to indicate that the leading final, or 'evolved,' SVs with $\tau \gtrsim T_w$ are approximately an orthogonalization of the leading Lyapunov vectors. Thus, ensemble forecasting systems using Lyapunov vectors and evolved SVs should behave roughly equivalently, all other things begin equal. The choice between SVs and Lyapunov vectors then becomes one of computational expediency. SVs require the solution of either a large eigenvalue problem or repeated integrations of a tangent linear model (Buizza et al., 2005) and, thus, represent a significantly more expensive computation than Lyapunov vectors, which can be computed at little additional cost to the ensemble forecast (Toth and Kalnay, 1993).

It should be noted that the present system is dominated by a single instability with a single time scale T_w. In the atmosphere, multiple instabilities with multiple time scales are present and there exists some evidence (Lorenz, 1996) that the leading Lyapunov vectors will be dominated by fast-growing, low-amplitude, instabilities (e.g., convective instabilities) which do not have a large impact on the large-scale flow. The breeding method, outlined in the introduction, attempts to circumvent this problem by allowing the disturbances to reach sufficient amplitude that the fast-growing, low-amplitude, disturbances saturate. The resulting bred vectors then capture the dynamics of the slower-growing, but larger-amplitude, baroclinic disturbances (Toth and Kalnay, 1993, 1997). The conclusions on the relative merits of SVs and Lyapunov vectors apply to bred vectors to the extent that bred vectors are 'proper' nonlinear generalizations of Lyapunov vectors. That is, to the extent that they capture the same patterns of variability that the leading Lyapunov vectors would capture if the fast-growing, low-amplitude, disturbances were not present in the system.

4.8 Summary

The singular vectors obtained in the present study characterize the transient growth of disturbances to a nonlinear wave-mean oscillation of a 2-layer quasi-geostrophic model. The model is simple enough to admit complete numerical solution in terms of time-dependent normal modes, but, with several thousand degrees of freedom, complex enough to allow connections to be made to realistic operational forecast models. Much like the Floquet vectors of the same system (WS), the singular vectors divide into two dynamical classes. Singular vectors in the wave-dynamical (WD) class grow or decay at rates significantly different from the dissipation rate and exhibit large oscillations on the time scale of the baroclinic wave mean oscillation. The singular vector spectrum is completed by a large number of damped-advective modes which decay at rates near the dissipation rate.

For optimization times greater than the baroclinic wave growth time scale, the WD singular vectors asymptotically approach constant linear combinations of Floquet vectors. The most rapidly decaying singular vectors project strongly onto the most rapidly decaying Floquet vectors. In contrast, the leading singular vectors project strongly onto the leading adjoint Floquet vectors. The leading singular vectors are thus optimal excitations of the leading Floquet vectors. Calculations where the initialization time was allowed to vary while the optimization interval was fixed to $\tau = T$ show that, while changes in the initialization time have a large impact on the singular values, they cause little change in the projection of the singular vectors onto the Floquet vectors. If the optimization interval is shortened to $\tau = T_w$, the decompositions of the SVs in terms of the forward SVs become complicated functions of initialization time, but the leading SVs remain relatively simple functions of the adjoint SVs.

Examination of Poincaré intersections near the basic cycle show that the leading FVs of the basic cycle point 'into' the local unstable tangent space of the attractor. The leading initial SVs, by contrast, point 'off' the attractor, but rotate into the local unstable tangent space by the optimization time. This demonstrates the value of Lyapunov vectors (here FVs) for describing the local structure of the attractor in a model of intermediate complexity, and suggests they may be useful for even more complex models.

A method for recovering the leading Floquet vectors from a relatively small number singular vectors was demonstrated using the present calculations. While this system used in the present study is significantly more complex than those considered by Wolfe and Samelson (2006b), the method was able to recover the leading Floquet vectors at a relative accuracy of 1% using singular vectors with $\tau = T$. Increasing the optimization time generally lead to significantly improved accuracy. This result suggests that the method may be robust enough for use in models with complexity comparable to operational forecast models.

4.9 Acknowledgement

The authors gratefully acknowledge the Office Naval Research, Grants N00014-98-1-0813 and N00014-06-1-0369, Code 322 OM, for support of this work. Computational resources were provided by the National Partnership for Advanced Computational Infrastructure and the San Diego Supercomputer Center.

4.10 References

Buizza, R., P. L. Houtekamer, Z. Toth, G. Pellerin, M. Wei, Y. B. Zhu, L. Galgani, A. Giorgilli, and J.-M. Strelcyn, 2005: A comparison of the ECMWF, MSC and NCEP global ensemble prediction systems. *Mon. Wea. Rev.*, **133**, 1076–1097.

Buizza, R. and T. Palmer, 1995: The singular vector structure of the atmospheric general circulation. *J. Atmos. Sci.*, **52**, 1434–1456.

Buizza, R., J. Tribbia, R. Molteni, and T. Palmer, 1993: Computation of unstable structures for a numerical weather prediction model. *Tellus*, **45A**, 388–407.

Eckmann, J.-P. and D. Ruelle, 1985: Ergodic theory of chaos and strange attractors. *Rev. Mod. Phys.*, **57**, 617–656.

Farrell, B. F., 1989: Optimal excitation of baroclinic waves. *J. Atmos. Sci.*, **46**, 1193–1206.

Kalnay, E., 2003: *Atmospheric Modeling, Data Assimilation and Predictability*. Cambridge University Press.

Klein, P. and J. Pedlosky, 1986: A numerical study of baroclinic instability at large supercriticality. *J. Atmos. Sci.*, **43**, 1243–1262.

Lorenz, E. N., 1965: A study of the predictability of a 28-variable atmospheric model. *Tellus*, **17**, 321–333.

— 1996: Predictability: a problem partly solved. *Predictability, Volume I*, European Centre for Medium-Range Weather Forecasts, 1–18.

Miller, R. N. and L. L. Ehret, 2002: Ensemble generation for models of multimodal systems. *Mon. Wea. Rev.*, **130**, 2313–2334.

Moore, A. M. and A. J. Mariano, 1999: The dynamics of error growth and predictability in a model of the Gulf Stream. Part I: singular vector analysis. *J. Phys. Oceanogr.*, **29**, 158–176.

Oseledec, V., 1968: A multiplicative ergodic theorem. Lyapunov characteristic numbers for dynamical systems. *Trans. Moscow Math. Soc.*, **19**, 179–210.

Palmer, T. N., 1996: Predictability of the atmosphere and oceans: From days to decades. *Predictability, Volume I*, European Centre for Medium-Range Weather Forecasts, 83–141.

Pedlosky, J., 1987: *Geophysical Fluid Dynamics*. Springer, second edition.

Phillips, N. A., 1954: Energy transformations and meridional circulations associated with simple baroclinic waves in a two-level, quasi-geostrophic model. *Tellus*, **6**, 273–286.

Reynolds, C. A. and T. N. Palmer, 1998: Decaying singular vectors and their impact on analysis and forecast correction. *J. Atmos. Sci.*, **55**, 3005–3023.

Samelson, R. and E. Tziperman, 2001: Instability of the chaotic ENSO: The growth-phase predictability barrier. *J. Atmos. Sci.*, **58**, 3613–3625.

Samelson, R. M., 2001a: Lyapunov, floquet, and singular vectors for baroclinic waves. *Nonlinear Processes Geophys.*, **8**, 439–448.

— 2001b: Periodic orbits and disturbance growth for baroclinic waves. *J. Atmos. Sci.*, **58**, 436–450.

Szuntogh, I., E. Kalnay, and Z. Toth, 1997: A comparison of Lyapunov and optimal vectors in a low-resolution GCM. *Tellus*, **49A**, 200–227.

Toth, Z. and E. Kalnay, 1993: Ensemble forecasting at NMC: the generation of perturbations. *Bull. Am. Met. Soc.*, **12**, 2317–2330.

— 1997: Ensemble forecasting at NCEP and the breeding method. *Mon. Wea. Rev.*, **125**, 3297–3319.

Trevisan, A. and F. Pancotti, 1998: Periodic orbits, Lyapunov vectors, and singular vectors in the Lorenz system. *J. Atmos. Sci.*, **55**, 390–398.

Vannitsem, S. and C. Nicolis, 1997: Lyapunov vectors and error growth patterns in a T21L3 quasigeostrophic model. *J. Atmos. Sci.*, **54**, 357–361.

Wei, M. and J. S. Frederiksen, 2004: Error growth and dynamical vectors during southern hemisphere blocking. *Nonlinear Processes Geophys.*, **11**, 99–118.

Wolfe, C. L. and R. M. Samelson, 2006a: Normal-mode analysis of a baroclinic wave-mean oscillation. *J. Atmos. Sci.*, in press.

— 2006b: Recovering Lyapunov vectors from singular vectors. *Tellus*, submitted.

Zeng, Q.-C., 1983: The evolution of a Rossby wave packet in a three-dimensional baroclinic atmosphere. *J. Atmos. Sci.*, **40**, 73–84.

Zhang, Z., 1988: *The Linear Study of Zonally Asymmetric Barotropic Flows*. Ph.D. thesis, University of Reading, UK.

5 SUMMARY

The study of disturbance growth is fundamental to the understanding of geophysical fluid instabilities and the forecasting of geophysical fluid flows. This dissertation presented a series of studies examining three ways of describing linear disturbances growth: normal modes, singular vectors, and Lyapunov vectors.

Chapter 2 gave a detailed discussion of the definitions of and relationships between normal modes, singular vectors, and Lyapunov vectors. It was argued that Lyapunov vectors provide a natural generalization of normal modes to aperiodic flows. Based on the results of a two-dimensional example problem, it was concluded that, under farly general conditions, singular vectors converge exponentially to constant linear combinations of Lyapunov vectors. Based on this conclusion, a direct and efficient method was developed which allows the first n Lyapunov vectors to be constructed in a norm-independent manner from the first n asymptotic forward and backward singular vectors. The method was demonstrated for two idealized geophysical examples and was shown to give correct results.

The next two chapters presented a detailed study of the normal modes (Floquet vectors) and singular vectors of a wave-mean oscillation in an intermediate complexity geophysical model.

The Floquet vectors obtained in chapter 3 characterized the asymptotic stability of the wave-mean oscillation. These Floquet vectors split into two dynamical classes which are analogous to those found by Samelson (2001b) in a weakly nonlinear model of the baroclinic instability. The wave-dynamical class was characterized by large-scale disturbances which are frequency-locked to the basic cycle and grow or decay at rates which are well separated from the dissipation rate. These modes were interpreted as a time-dependent analog of the inviscidly growing and decaying modes of the classic Phillips (1954) model. The number of wave-dynamical modes was much smaller than the total number of numerically determined Floquet vectors and these modes appeared to form a discrete set. By contrast, the damped-advective class, characterized by small-scale disturbances advected by the background flow and damped at a rate near the dissipation rate, dominated the numerical Floquet spectrum. Individual damped-advective modes did not have natural physical interpretations, but the class, taken as a whole, appeared to represents a generalized solution to the damped advection problem. In this sense, the damped-advective class resembled a numerical approximation to the continous spectrum of normal modes often seen in problems with continous horizontal or veritical shear (Case, 1960).

The singular vectors obtained in chapter 4 characterize the transient growth of disturbances to the wave-mean oscillation. The singular vectors divided into same dynamical classes as the Floquet vectors, indicating that the dynamical splitting of the normal modes was preserved in the structure of the singular vectors spectrum. Consistent with the results of chapter 2, the wave-dynamical singular vectors approached constant linear combinations of Floquet vectors for optimization times greater than the baroclinic wave growth time scale. The most rapidly decaying singular vectors projected strongly onto the most rapidly decaying Floquet vectors, while the leading singular vectors projected strongly onto the leading *adjoint* Floquet vectors. The leading singular vectors were thus optimal excitations of the leading Floquet vectors. For optimization times on the order of the period of the wave-mean oscillation, both the singular values and singular vectors were strong functions of the initialization time. However, the projections of the singular vectors onto the Floquet vectors were almost independent of initialization time, confirming that the strong connection between the normal modes and singular vectors observed in the weakly nonlinear baroclinic instability model is preserved in the present, much less constrained, model.

Examination of Poincaré intersections near the wave-mean oscillation showed that the leading Floquet vectors pointed 'into' the local unstable tangent space of the attractor. The leading initial singular vectors, by contrast, pointed 'off' the attractor, but rotated into the local unstable tangent space by the optimization time.

The method for recovering the leading Floquet vectors from a relatively small number singular vectors developed in chapter 2 was demonstrated using the Floquet and singular vectors of the wave-mean oscillation. While this system used in the present study is significantly more complex than those considered in chapter 2, the method was able to recover the leading Floquet vectors at a relative accuracy of 1% using singular vectors with optimization intervals equal to the period of the wave-mean oscillation. Increasing the optimization time generally lead to significantly improved accuracy. This result suggests that the method may be robust enough for use in models with complexity comparable to operational forecast models.

Accurate ensemble forecasting requires that the ensembles be initialized in such a way that their subsequent evolution is representative of the possible future states of the atmosphere or ocean. This initialization should also be economical, so that the broadest possible set of future states is achieved by the smallest possible ensemble. In the present case, the asymptotic stability of the basic cycle is determined by the leading wave-dynamical modes so these modes are a natural choice for the ensemble initial conditions. These modes have the advantage that they are few in number and that they are fluid instabilities which are related, in a straightforward manner, to the background flow. This implies that the modes which are most interesting from the standpoint of geophysical fluid dynamical instability theory are also natural choices for ensemble initial conditions. The results of chapters 2 & 4 indicate that, for optimization intervals greater than or equal to the baroclinic growth time scale, the leading final, or 'evolved,' singular vectors are approximately an orthogonalization of the leading wave-dynamical modes. Thus, ensemble forecasting systems using the wave-dynamical modes and evolved singular vectors should behave roughly equivalently, all other things being equal. The choice between singular vectors and the leading wave-dynamical modes then becomes one of computational expediency. Singular vectors require the solution of either a large eigenvalue problem or repeated integrations of a tangent linear model (Buizza et al., 2005) and, thus, represent a significant computation while the leading wave-dynamical modes can be computed at little additional cost to the ensemble forecast.

As noted in section 4.5 and by other authors (e.g., Kalnay, 2003, §6.3 and references therein), the initial singular vectors point 'off' the attractor and thus represent 'unlikely' perturbations provided the forecast model is a reasonably good representation of the atmosphere. This may indicate that initial singular vectors are not a good choice for initial perturbations of ensemble members.

6 REFERENCES

Bennetin, G., L. Galgani, A. Giorgilli, and J.-M. Strelcyn, 1980: Lyapunov characteristic exponents for smooth dynamical systems and for Hamiltonian systems: A method for computing all of them. *Meccanica*, **15**, 9–21.

Buizza, R., P. L. Houtekamer, Z. Toth, G. Pellerin, M. Wei, Y. B. Zhu, L. Galgani, A. Giorgilli, and J.-M. Strelcyn, 2005: A comparison of the ECMWF, MSC and NCEP global ensemble prediction systems. *Mon. Wea. Rev.*, **133**, 1076–1097.

Buizza, R. and T. Palmer, 1995: The singular vector structure of the atmospheric general circulation. *J. Atmos. Sci.*, **52**, 1434–1456.

Buizza, R., J. Tribbia, R. Molteni, and T. Palmer, 1993: Computation of unstable structures for a numerical weather prediction model. *Tellus*, **45A**, 388–407.

Case, K. M., 1960: Stability of inviscid plane Couette flow. *Phys. Fluids*, **3**, 143–148.

Charney, J. G., 1947: The dynamics of long waves in a baroclinic westerly current. *J. Meteor.*, **4**, 135–163.

Coddington, E. A. and N. Levinson, 1955: *Theory of Ordinary Differential Equations*. Krieger Publishing Company.

Cvitanović, P., R. Artuso, R. Mainieri, G. Tanner, and G. Vattay, 2005: *Chaos: Classical and Quantum*. Neils Bohr Institute, Copenhagen, ChaosBook.org.

Drazin, P. G. and W. H. Reid, 2004: *Hydrodynamical Stability*. Cambridge University Press, Cambridge, UK, second edition.

Durran, D. R., 1998: *Numerical Methods for Wave Equations in Geophysical Fluid Dynamics*. Springer-Verlag.

Eady, E. T., 1949: Long waves and cyclone waves. *Tellus*, **1**, 33–52.

Eckmann, J.-P. and D. Ruelle, 1985: Ergodic theory of chaos and strange attractors. *Rev. Mod. Phys.*, **57**, 617–656.

Ehrendorfer, M. and J. Tribbia, 1997: Optimal prediction of forecast error covariances through singular vectors. *J. Phys. Oceanogr.*, **54**, 286–313.

Farrell, B. F., 1989: Optimal excitation of baroclinic waves. *J. Atmos. Sci.*, **46**, 1193–1206.

Farrell, B. F. and P. J. Ioannou, 1996: Generalized stability theory part I: autonomous operators. *J. Atmos. Sci.*, **53**, 2025–2040.

Frederiksen, J. S., 1997: Adjoint sensitivity and finite-time normal mode disturbances during blocking. *J. Atmos. Sci.*, **54**, 1144–1165.

Goldhirsch, I., P. L. Sulem, and A. Orszag, 1987: Stability and lyapunov stability of dynamical systems: a differential approach and a numerical method. *Phyisca D*, **27**, 311–337.

Golub, G. H. and C. F. Van Loan, 1996: *Matrix Computations*. The Johns Hopkins University Press Ltd, London, 3rd edition edition.

Grassberger, P. and I. Procaccia, 1983: Measuring the strangeness of strange attractors. *Physica*, **9D**, 189–208.

Hart, J. E., 1981: Wavenumber selection in nonlinear baroclinic instability. *J. Atmos. Sci.*, **38**, 400–408.

Itoh, H. and M. Kimoto, 1996: Multiple attractors and chaotic itineracy in a quasi-geostrophic model with realistic topography: Implications for weather regimes and low-frequency variability. *J. Atmos. Sci.*, **53**, 2217–2231.

James, I. N., 1987: Suppression of baroclinic instability in horizontally sheared flows. *J. Atmos. Sci.*, **44**, 3710–3720.

Kalnay, E., 2003: *Atmospheric Modeling, Data Assimilation and Predictability*. Cambridge University Press.

Kazantsev, E., 1998: Unstable periodic orbits and attractor of the barotropic ocean model. *Nonlinear Processes Geophys.*, **5**, 193–208.

— 2001: Sensitivity of the attractor of the barotopic ocean model to external influences: approach by unstable periodic orbits. *Nonlinear Processes Geophys.*, **8**, 281–300.

Klein, P. and J. Pedlosky, 1986: A numerical study of baroclinic instability at large supercriticality. *J. Atmos. Sci.*, **43**, 1243–1262.

Kuchment, P., 1993: *Floquet Theory for Partial Differential Equations*. Birkhauser Verlag, Basel.

Legras, B. and R. Vautard, 1996: A guide to Liapunov vectors. *Predictability, Volume I*, European Centre for Medium-Range Weather Forecasts, 143–156.

Lorenz, E. N., 1963: Deterministic non-periodic flow. *J. Atmos. Sci.*, **20**, 130–141.

— 1965: A study of the predictability of a 28-variable atmospheric model. *Tellus*, **17**, 321–333.

— 1984: The local structure of a chaotic attractor in four dimensions. *Physica D*, **13**, 90–104.

— 1996: Predictability: a problem partly solved. *Predictability, Volume I*, European Centre for Medium-Range Weather Forecasts, 1–18.

Lust, K., D. Roose, A. Spence, and A. Champneys, 1998: An adaptive Newton-Picard algorithm with subspace iteration for computing periodic solutions. *SIAM J. Sci. Comp.*, **19**, 1188–1209.

Miller, R. N. and L. L. Ehret, 2002: Ensemble generation for models of multimodal systems. *Mon. Wea. Rev.*, **130**, 2313–2334.

Moore, A. M. and A. J. Mariano, 1999: The dynamics of error growth and predictability in a model of the Gulf Stream. Part I: singular vector analysis. *J. Phys. Oceanogr.*, **29**, 158–176.

Orr, W. M., 1907: The stability or instability of the steady motions of a perfect liquid and of a viscous liquid. *Proc. Roy. Irish Acad.*, **27**, 9–138.

Oseledec, V., 1968: A multiplicative ergodic theorem. Lyapunov characteristic numbers for dynamical systems. *Trans. Moscow Math. Soc.*, **19**, 179–210.

Palmer, T. N., 1996: Predictability of the atmosphere and oceans: From days to decades. *Predictability, Volume I*, European Centre for Medium-Range Weather Forecasts, 83–141.

Pedlosky, J., 1971: Finite-amplitude baroclinic waves with small dissipation. *J. Phys. Oceanogr.*, **28**, 587–597.

— 1981: The nonlinear dynamics of baroclinic wave ensembles. *J. Fluid Mech.*, **102**, 169–209.

— 1987: *Geophysical Fluid Dynamics*. Springer, second edition.

Pedlosky, J. and C. Frenzen, 1980: Chaotic and periodic behavior of finite-amplitude baroclinic waves. *J. Atmos. Sci.*, **37**, 1177–1196.

Pedlosky, J. and J. Thomson, 2003: Baroclinic instability of time-dependent currents. *J. Fluid Mech.*, **490**, 189–215.

Phillips, N. A., 1954: Energy transformations and meridional circulations associated with simple baroclinic waves in a two-level, quasi-geostrophic model. *Tellus*, **6**, 273–286.

Poulin, F. J., G. R. Flierl, and J. Pedlosky, 2003: Baroclinic instability of oscillatory shear flow. *J. Fluid Mech.*, **481**, 329–353.

Reynolds, C. A. and T. N. Palmer, 1998: Decaying singular vectors and their impact on analysis and forecast correction. *J. Atmos. Sci.*, **55**, 3005–3023.

Samelson, R. and E. Tziperman, 2001: Instability of the chaotic ENSO: The growth-phase predictability barrier. *J. Atmos. Sci.*, **58**, 3613–3625.

Samelson, R. M., 2001a: Lyapunov, floquet, and singular vectors for baroclinic waves. *Nonlinear Processes Geophys.*, **8**, 439–448.

— 2001b: Periodic orbits and disturbance growth for baroclinic waves. *J. Atmos. Sci.*, **58**, 436–450.

Samelson, R. M. and C. L. Wolfe, 2003: A nonlinear baroclinic wave-mean oscillation with multiple normal mode instabilities. *J. Atmos. Sci.*, **60**, 1186–1199.

Shimada, I. and T. Nagashima, 1979: A numerical approach to the ergodic problem of dissipative dynamical systems. *Prog. Theor. Phys.*, **61**, 1605–1616.

Sparrow, C., 1982: *The Lorenz Equations: Bifurcations, Chaos, and Strange Attractors*. Springer-Verlag.

Szuntogh, I., E. Kalnay, and Z. Toth, 1997: A comparison of Lyapunov and optimal vectors in a low-resolution GCM. *Tellus*, **49A**, 200–227.

Toth, Z. and E. Kalnay, 1993: Ensemble forecasting at NMC: the generation of perturbations. *Bull. Am. Met. Soc.*, **12**, 2317–2330.

— 1997: Ensemble forecasting at NCEP and the breeding method. *Mon. Wea. Rev.*, **125**, 3297–3319.

Trevisan, A. and R. Legnani, 1995: Transient error growth and local predictability: a study of the Lorenz system. *Tellus*, **47A**, 103–117.

Trevisan, A. and F. Pancotti, 1998: Periodic orbits, Lyapunov vectors, and singular vectors in the Lorenz system. *J. Atmos. Sci.*, **55**, 390–398.

Vannitsem, S. and C. Nicolis, 1997: Lyapunov vectors and error growth patterns in a T21L3 quasigeostrophic model. *J. Atmos. Sci.*, **54**, 357–361.

Vastano, J. A. and R. D. Moser, 1991: Short-time Lyapunov exponent analysis and the transition to chaos in Taylor-Couette flow. *J. Fluid Mech.*, **233**, 83–118.

Wei, M. and J. S. Frederiksen, 2004: Error growth and dynamical vectors during southern hemisphere blocking. *Nonlinear Processes Geophys.*, **11**, 99–118.

Wiggins, S., 2003: *Introduction to Applied Nonlinear Dynamical Systems and Chaos*. Springer, New York, second edition, 843 pp.

Wolfe, C. L. and R. M. Samelson, 2006a: Normal-mode analysis of a baroclinic wave-mean oscillation. *J. Atmos. Sci.*, in press.

— 2006b: Recovering Lyapunov vectors from singular vectors. *Tellus*, submitted.

Yoden, S. and M. Nomura, 1993: Finite time lyapunov stability analysis and its application to atmospheric predictability. *J. Atmos. Sci.*, **50**, 1531–1543.

Zeng, Q.-C., 1983: The evolution of a Rossby wave packet in a three-dimensional baroclinic atmosphere. *J. Atmos. Sci.*, **40**, 73–84.

Zhang, Z., 1988: *The Linear Study of Zonally Asymmetric Barotropic Flows*. Ph.D. thesis, University of Reading, UK.